The Thesis Committee for Michael Kazuto Chang
Certifies that this is the approved version of the following thesis:

Development of a Testing Protocol for Insulation Ignition by Wildland Fire Embers

APPROVED BY
SUPERVISING COMMITTEE:

Ofodike A. Ezekoye, Supervisor

Kevin C. Marr

Development of a Testing Protocol for Insulation Ignition by Wildland Fire Embers

by

Michael Kazuto Chang

Thesis

Presented to the Faculty of the Graduate School of

The University of Texas at Austin

in Partial Fulfillment

of the Requirements

for the Degree of

Master of Science in Engineering

The University of Texas at Austin

August 2017

Acknowledgements

I would like to thank Dr. Ezekoye, Kevin Marr, and all of my friends and family for their love, support, and guidance. Funding for this work was provided by the Department of Commerce through NIST (Grant no. 60NANB16D278) and by the Department of Interior through the Joint Fire Science Program under project JFSP 15-1-04-4.

Abstract

Development of a Testing Protocol for Insulation Ignition by Wildland Fire Embers

Michael Kazuto Chang, M.S.E

The University of Texas at Austin, 2017

Supervisor: Ofodike A. Ezekoye

Wildfire embers, also known as firebrands, are one of the dominant fire spread elements in wildfire growth. These embers are associated with the ignition of structures at the wildland-urban interface (WUI) and there is effort to understand the mechanisms by which they ignite homes. One of the vulnerable areas of homes at the WUI is the attic space.

The ignition of attic materials by embers is not a well characterized problem, and so an effort was made to better understand the parameters critical to this issue. This thesis details the assessment of the ignition processes for embers attacking attic materials. An experimental procedure was developed to create consistent embers of specific sizes with well characterized thermal properties. These embers were transferred to various fuel beds, where air flow conditions were adjusted to determine which conditions would cause the fuel bed to ignite, extinguish, or smolder. The materials tested were extruded polystyrene (XPS), expanded polystyrene (EPS), polyurethane (PUR), flame retarded/non-flame

retarded denim, and flame retarded/non-flame retarded cellulose, which are all typical insulation materials found in the attic. The differences between flame retarded and non-flame retarded materials were highlighted through these material comparisons. Two configurations of embers, a single large ember vs. an equivalent mass pile of fragmented embers, were tested. Thermocouples and IR camera recordings were used to monitor fuel bed and ember temperatures, in order to investigate the signatures of ignition

Once the critical ignition parameter space was defined, a better understanding of the material properties was required to discern what material features were responsible for the ember flammability observations. In order to accomplish this, simple methodologies for measuring thermal conductivity, specific heat, and density were created. The oxygen consumption (cone) calorimeter was used to determine flammability characteristics of the materials, such as heat release rates and ignition times, while thermogravimetric analysis was used to define the material degradation behavior. Finally, X-ray diffraction was explored in order to find the presence of flame retardants in the various materials.

Table of Contents

List of Tables

List of Figures

Chapter 1: Introduction

1.1 Wildland Urban Interface Introduction

The frequency and severity of wildland fires have increased in recent years. These fires burn vast regions of grass and forest land area, destroy wildlife, and affect the built environment when they extend to the wildland urban interface. Assessing how a particular wildfire will impact the built environment has proven to be extraordinarily difficult.

Wildfire spread rates are dependent on a complex coupling between meteorological factors, topography, and fuel density. Further, predicting if and how a fire will penetrate particular types of structures and ignite material within the structure is equally complex. A range of potential failure pathways exist in current structures, such as unprotected gutters containing dried organic material, flammable roofing materials, vents that can allow ember transport into attic spaces, attic insulation that can ignite if embers breech the vents, window sills, re-entrant corners built with flammable materials, etc [1,2]. Assessment of wildfire impact on structures relies on development of a framework to analyze building vulnerabilities to wildfire threat.

In general, very little work has been done on assessing how transported embers from a wildfire affect building materials and configurations. There is widespread agreement that vents represent a significant path for wildland fires to ignite homes [1]. Fire ignition can take place through vents either by ember transport into the vents or direct flame impingement on the vents. Despite this awareness, there is still little understanding of the mechanisms associated with ember penetration and ignition in attic spaces.

1.2 Particle Ignition Introduction

Given the recent interest in green and sustainable construction, various types of attic insulation are also now available for use in attic and void spaces. With increased frequency of wildfires and increased variability in the types of insulating materials being used in attic spaces, it is critical that careful study is conducted to understand what insulation properties make an attic space more vulnerable to wildfire threats, as well as what mass flux of embers presents critical issues.

Manzello et al. [2] used a firebrand generator to test the ignition of paper beds through various vent mesh sizes. The mass flux of firebrands, however, was not characterized, and the critical ember mass flux for ignition was not well understood. Manzello has also investigated the effects of firebrands deposited on naturally occurring fuel beds as well as firebrands deposited on wooden boards and roof shingles [3-5]. In those studies, the effects of single and multiple ember deposition and varying fuel bed moisture content, vegetation type, and air flow were experimentally measured to better understand what factors influence ignition. Firebrands were produced by heating wooden cylinders with either a 5 mm or 10 mm diameter, and either a 51 mm or 76 mm length, respectively, using a butane burner, while being held by a linear actuator. Both glowing and flaming ember attacks were released by the actuator onto pine needle beds, shredded paper beds and hardwood mulch beds. Moisture content of the fuel bed and the amount of air flow all affected the ignition of the beds. When comparing the ignition propensity of cylindrical embers and disk-shaped embers, Manzello et al. found that the cylindrical mass that would cause ignition was only half of the mass required by the disk-shaped.

Furthermore, they found that the contact surface area between the cylindrical ember and the fuel bed that was necessary for ignition was only 80% of that required by the disk-shaped contact surface area. This shows that the contact surface area is more likely important to ignition than mass, and that the firebrand shape is also an important driver.

Other researchers have looked to characterize the ignition problem using hot metal spheres. Urban et al. [6] heated metal spheres that were held in a ceramic spoon in a furnace at various temperatures, which were then dropped onto a powdered cellulose fuel bed. The response of the fuel bed was categorized by either no ignition, smoldering ignition, or flaming ignition, while the diameter, the type of metal, and the temperature of the spheres were altered. Wang et al.[7], Hadden et al. [8], and Zak [9] also characterized ignition propensity of EPS foam, alpha cellulose, and cellulose respectively, based on the temperatures of hot steel spheres of varying sizes. They all found that the temperatures and size of the particles were key drivers behind the ignition process.

Ignition research on insulative building materials, up until now, has either used non-characteristic firebrand materials, such as metals, to test ignition behavior or a single characteristic (surface) temperature measurement to describe the firebrand. Additionally, burners have often been used to ignite firebrand materials. While burners can readily cause flaming ignition of the embers, it is harder to control the overall time-temperature evolution of the ember with burners. Further, most firebrands are not flaming when they are deposited onto substrate materials.

In order to better understand the key parameters to ignition, an experimental procedure was created to replicate the conditions involved with the transport of an ember

through an attic vent and onto various types of insulation. Embers were created in a furnace, and were then either dropped or placed using tweezers onto various types of insulation typically found in attic spaces, such as rigid polyurethane foam (PUR), expandable polystyrene (EPS), extruded polystyrene (XPS), denim insulation, and loose-fill cellulose, all of which had flame retardants in them. The behavior of the ember and fuel bed is observed using thermocouples, an IR camera, and a DSLR camera to better understand the process after the ember touches the fuel bed. During a wildfire event, it can be conjectured that a high flux of embers can penetrate the attic, forming piles of embers in the attic space. The effects of having a pile of smaller embers vs. a larger ember with the same equivalent mass was explored, as well as the effects of air flow conditions of 0 m/s, 2.4 m/s, and 4.8 m/s introduced over the fuel beds.

After performing these ignition experiments, a better understanding of the ignition characteristics of the various materials was needed. Analysis of the material characteristics were performed, that spanned finding basic thermal properties, such as thermal conductivity, specific heat, and density, to identifying various compounds such as flame retardants using X-ray diffraction. Furthermore, the flammability characteristics were investigated using cone calorimetry, while the material degradation behavior was found using thermogravimetric analysis (TGA).

Chapter 2 Ember Ignition: Experimental Determination of Insulation Ignition Parameters

For any material, the path to ignition depends on many factors, but in the simplest sense, ignition is driven by the ability of the material to generate a credible amount of pyrolyzate such that this pyrolyzate can support a flame of sufficient heat release rate that can maintain the rate of pyrolyzate production. There is a heat flux requirement from the deposited embers that must support the production of pyrolysis gases. There is a global energy balance consideration that must be met that states that the total amount of thermal energy above the ambient temperature field must be equal to the amount of energy required for the production of a unit of pyrolyzate gas. There is an awareness that the total amount of available energy will also be lost through parasitic processes (i.e., heat loss to the ambient). Over the burning time of the ember, there is conversion of chemical energy to thermal energy. The net available thermal energy supports the production of the pyrolysis gases and also must be of sufficient thermal potential to ignite the pyrolyzate.

2.1 Thermal Model

The physics involved in the coupled ember and fuel bed system are shown in Figure 2.1. Once the hot ember comes into contact with the fuel bed, the solid fuel bed begins to volatilize/pyrolyze. The flow over the fuel bed contributes to the oxidation of the ember, increasing its surface temperature, and thus increasing the rate at which the ember can volatilize the fuel bed. In the case of an ignition event, the fuel bed will continue to pyrolyze until the air/fuel mixture is able to be piloted by the ember. In the case of an extinction

event, the convection from the air flow and the radiative heat losses will be greater than the heat generated through oxidation of the ember. The equations below show this process, where m_E is the mass of the ember, c_E is the specific heat of the ember, T is the temperature of the ember, $\dot{Q_{RXN}}$ is the heat generated by the exothermic reactions of the ember, $\dot{Q_{cond}}$ is the heat lost by the ember to the fuel substrate, $\dot{Q_{conv}}$ is the heat lost by the ember due to convection, $\dot{Q_{rad}}$ is the heat lost due to radiation, δ(t) is the charring pyrolysis boundary layer thickness into the fuel bed over time, ρ_c is the density of the substrate after it has been charred, A is the area of the substrate, ρ_o is the density of the virgin material, ω_0" is the mass loss rate per area, and ω''' is the volumetric mass loss rate.

$$m_E c_E \frac{dT}{dt} = \dot{Q}_{RXN} - \dot{Q}_{cond} - \dot{Q}_{conv} - \dot{Q}_{rad} \tag{2.1}$$

The charring substrate solid mass equation can be written as:

$$\frac{d}{dt}\int_0^{\delta(t)} \rho_c A dx = \rho_0 A \frac{d\delta}{dt} - \int_0^{\delta(t)} w''' A dx \tag{2.2}$$

We can assume that the reaction processes are thin and occur at the interface:

$$w''' = w_0'' \delta(x - \delta(t)) \tag{2.3}$$

$$\frac{d}{dt}\int_0^{\delta(t)} \rho_c dx = \rho_0 \frac{d\delta}{dt} - \omega_0" \tag{2.4}$$

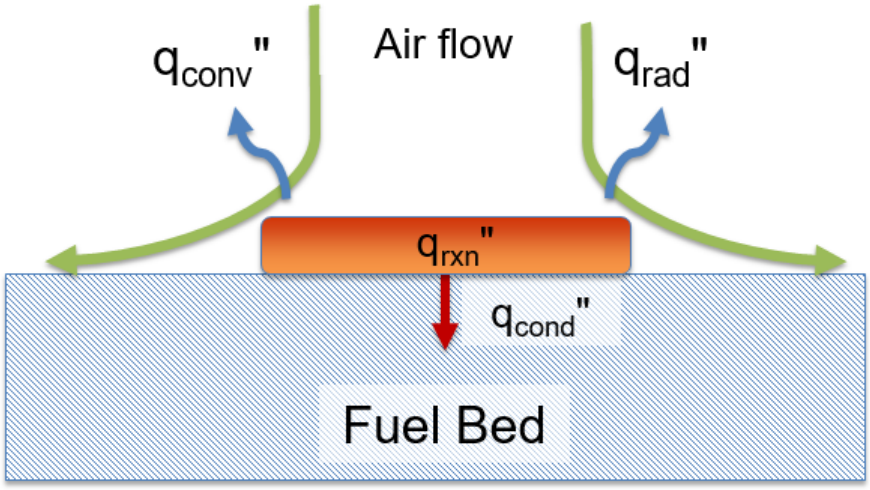

Figure 2.1: Heat and mass transfer process around an ember deposited onto a fuel bed

2.2 Experimental System

In order to simulate embers falling onto fuel beds, a two-step experimental procedure has been developed. The embers were prepared using machined pine dowels with a 10 mm (0.39”) diameter that were purchased commercially. During the first step of processing, one of two sizes of the pine dowels, with a length of either 50 mm (1.97”) or a length of 10 mm (0.39”), Figure 2.2, was placed inside of a Thermolyne Model F21115 tube-furnace in order to create glowing embers. The tube inside of the furnace had a 38 mm (1.5”) inner diameter.

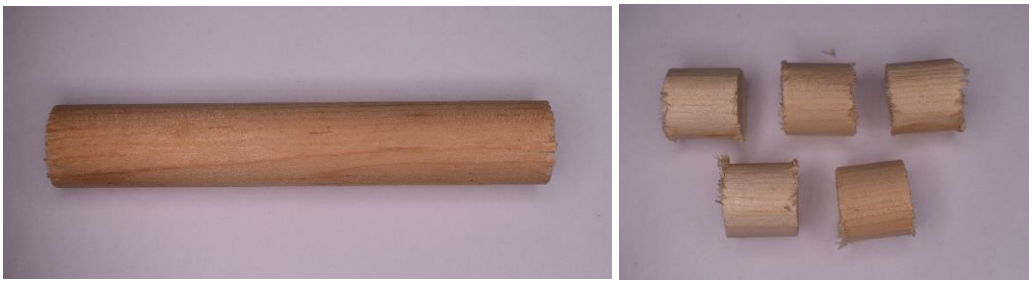

Figure 2.2: a) Large ember of 10 mm diameter and 50 mm length b) Fragmented dowel of 10 mm diameter and 10 mm length

The large 50 mm (1.97”) embers were transported inside of the furnace using one of two methods. The first method involved placing the ember inside of a metal-mesh basket and then feeding the basket through the bottom of the furnace, until the center of the ember aligned with the center of the furnace, as seen in Figure 2.3a. The second method involved drilling a hole in the radial center of the dowel, until the hole reached the vertical center of the dowel. The hole was then filled with Elmer’s Carpenter’s Stainable Interior/Exterior Wood Filler, while a k-type, 24-gauge, high temperature glass thermocouple was then fit inside of the hole and was used to monitor the centerline temperature of the ember. To further ensure the thermocouple stayed within the hole, a layer of Elmer’s Carpenter’s Wood Glue was placed on the top of the dowel to keep the thermocouple attached to the ember. The ember attached to the thermocouple was then fed from the bottom of the furnace until the center of the ember aligned with the vertical center of the furnace, as seen in Figure 2.3b. The procedure for the smaller fragmented embers will be discussed later.

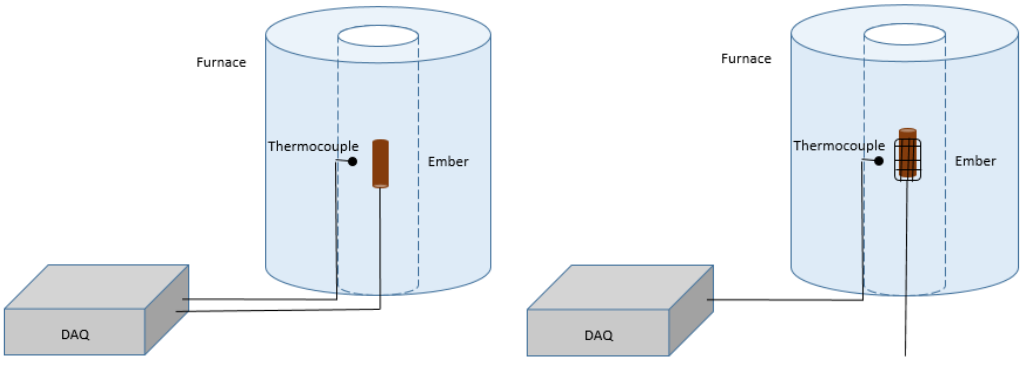

Figure 2.3: a) Furnace setup with thermocouple inserted ember b) Furnace setup with ember in mesh basket

The furnace was instrumented with a k-type, 24-gauge, high temperature glass thermocouple in the center of both the vertical and radial axis of the furnace. These dowels were then placed inside of the furnace at a constant temperature for a set amount of time, so that the embers could reach the desired criteria. An ideal ember was one that was symmetrical, had no fractures or cracks, and had an exit diameter of approximately 6.35 mm (0.25”). This size was chosen since this is a common mesh size that is used to obstruct attic vents. Furthermore, the choice of 10 mm (0.4”) diameter dowels was to create embers of approximately this size as well.

2.2.1 Initial Furnace Issues

Due to the diameter of the furnace tube, 38 mm (1.5”), and the effects of natural convection, a temperature gradient naturally occurred in both the radial and axial direction of the furnace. Initially, the production of embers was very inconsistent, where only one out of every ten embers would meet the desired criterion. In order to explore this issue, three k-type, 24-gauge, high temperature glass thermocouples were attached to a wire mesh that was cut into a circle with the same diameter as the furnace, Figure 2.4, which were then placed inside of the furnace. The thermocouples were attached to the wire mesh in order to keep all of the thermocouples at the same height inside of the furnace.

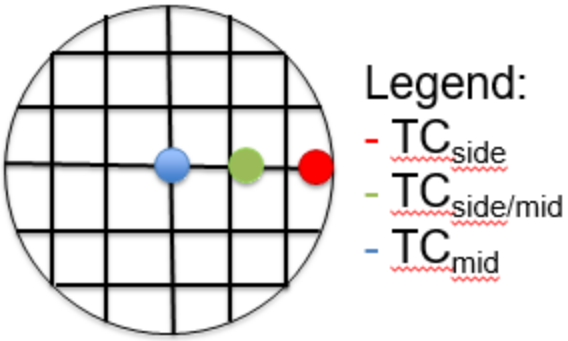

Figure 2.4: Thermocouple arrangement on wire mesh

The temperature gradient between the three thermocouples was monitored by the wire mesh roughly one inch below the vertical center of the furnace at a steady furnace temperature of 410 °C, seen in Figure 2.5. A temperature gradient of about 80 °C occurred between the side and middle thermocouples, and during other tests, temperature gradients of 100 °C occurred as well. Furthermore, the temperature measured by the centerline furnace thermocouple is higher than the temperature measured by the middle thermocouple on the wire mesh which was one inch below, demonstrating the presence of the vertical thermal gradient. The temperature measured by the centerline furnace thermocouple was still lower than the side temperature, demonstrating the larger radial thermal gradient compared to the vertical thermal gradient.

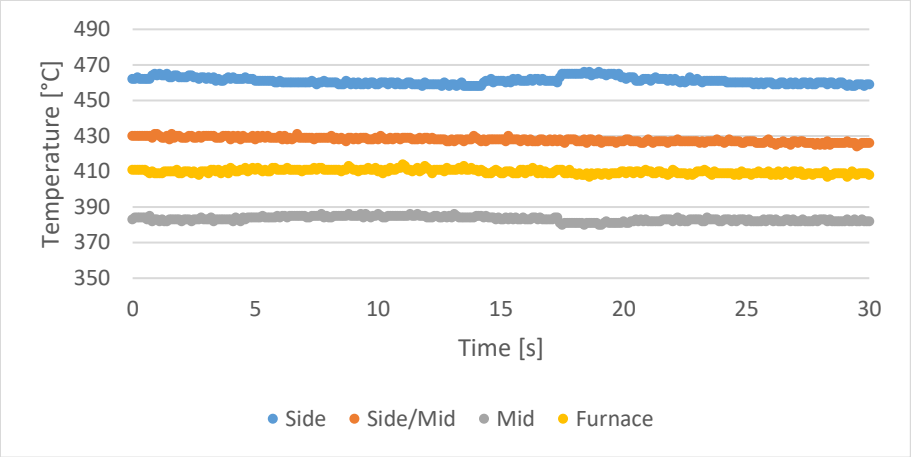

Figure 2.5: Thermal gradient at a furnace temperature of 410 °C

It was known that mixing the air inside of the furnace would help reduce the thermal gradient, and so an addition to the furnace system was added, as seen in Figure 2.6, that helped encourage mixing through the use of air flow. A series of three copper tubes with a 9.5 mm (3/8”) diameter were fitted to a plate with a 19 mm (3/4”) hole and three 9.5 mm holes (3/8”) drilled radially symmetrical. This plate was then placed over the top of the furnace pipe, where the copper tubes would distribute air through the top opening of the furnace. In-house air was split up roughly equally between the three tubes, and was monitored using a Dwyer RMC 102-SSV air flow meter. A second plate with a 19 mm (3/4”) hole was also placed at the bottom exit of the tube furnace in order to restrict air flow into the furnace. The air flow through the bottom of the furnace was the source of the convective cooling inside of the furnace, and so minimizing this effect was desirable. From previous testing, it was shown that a pipe with this diameter was able to produce embers inside of the furnace.

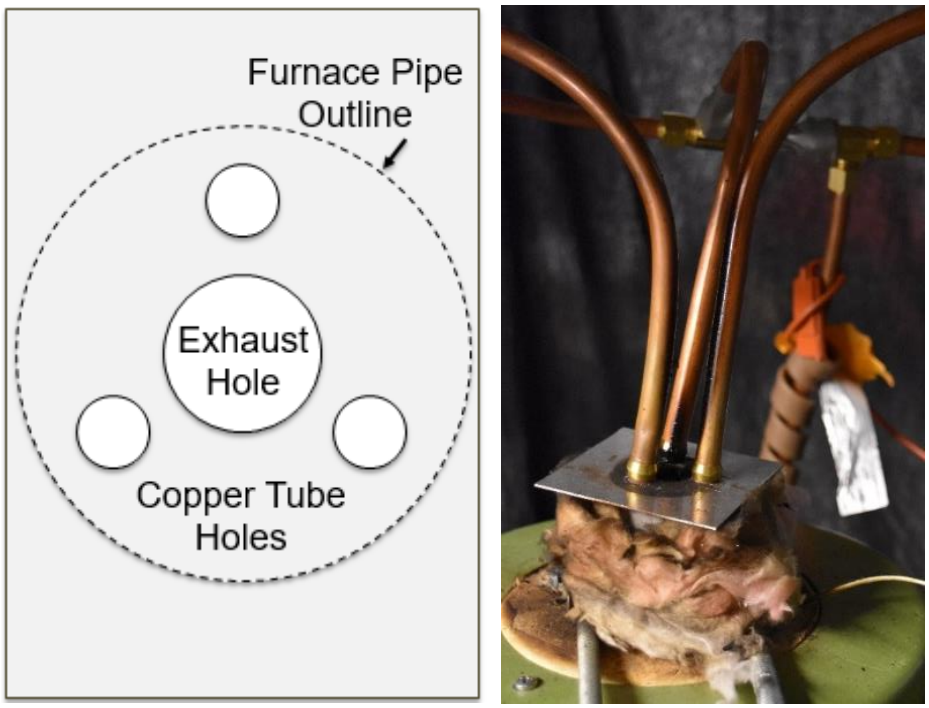

Figure 2.6: a) Schematic of top plate on furnace pipe b) Image of copper tubes feeding into furnace through top plate

It was found that an air flow between 7.1 l/min – 14.2 l/min (15 SCFH – 30 SCFH) dropped the temperature gradient down to about 10 °C – 15 °C. Figure 2.7a shows the thermal gradient to be about 10 °C between the three thermocouples when the air is turned on at a furnace temperature of 450 °C. Figure 2.7b starts with the air flow turned on until around 40 seconds when the air flow is turned off, and eventually a thermal gradient of about 100 °C develops between the thermocouples, showing the effect that the air flow has on minimizing the thermal gradient.

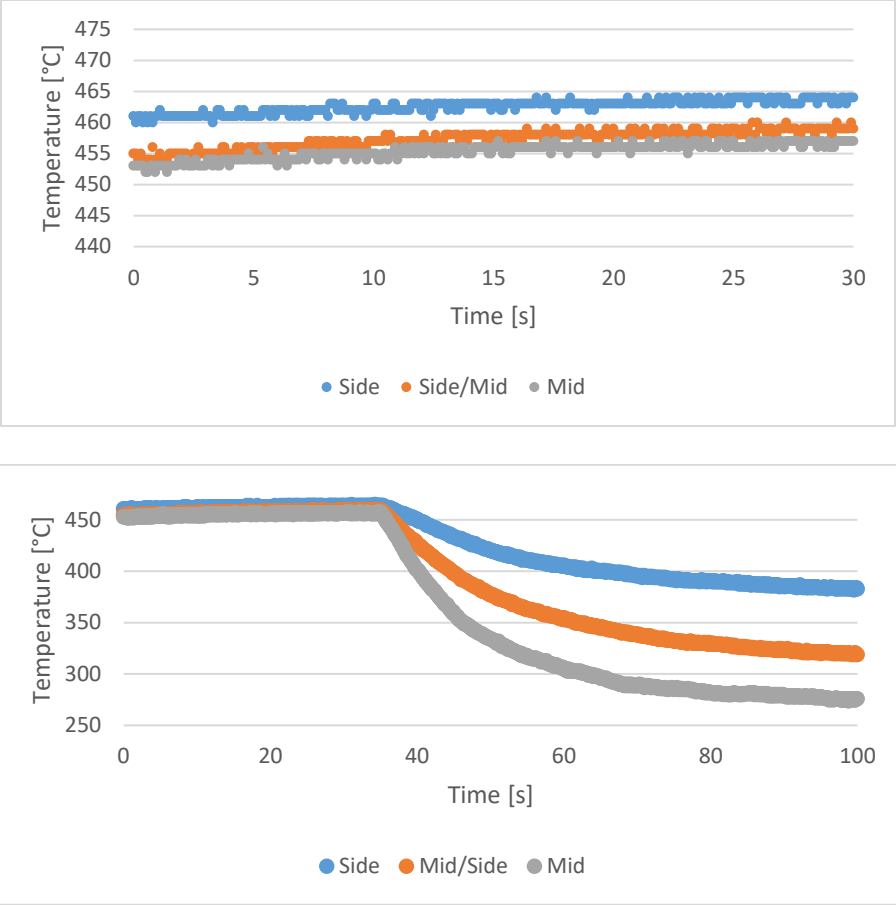

Figure 2.7: a) Furnace thermal gradient with 10.4 l/min of air (top) b) Furnace thermal gradient with no air (bottom)

Embers were then placed inside of the furnace using this range of air flows, while also changing the furnace temperature between 400 °C – 500 °C. An air flow of 10.4 l/min (22 SCFH) with a furnace temperature of 420 °C was shown to be the optimal combination of conditions, producing a small temperature gradient of 10 °C, while also promoting quality ember production. This improved the repeatability of the ember production, resulting in a one in three chance of obtaining a quality ember. Lower air flows would produce larger temperature gradients, and would thus result in less repeatability. Higher air flows would convectively cool the embers to an extent where they would not be able to reach the temperature where they could oxidize. Thus, the resulting embers would be non-

glowing and exit at a much lower temperature. To minimize the cooling effect, the copper tubes were repositioned so that a 30.5 cm (12”) segment was directly above the furnace, allowing the hot exhaust air to help pre-heat the copper tubes, and thus pre-heat the air inside of the tubes. A 52 W Omegalux medium temperature heating tape was wrapped around the copper tube section before the exhaust heated section to also help pre-heat the air in the copper tubes. However, it was found that the cooling effect of the air on the ember was still too large. Even if the air blowing over the ember was at the furnace temperature of 420 °C, the temperature difference between the air and the typical centerline temperature we observed the ember to oxidize at, 700 °C – 800 °C, would still be large. Thus, the only way to lower this effect was to reduce the air flow to the 22 SCFH air flow condition that was used.

An effort was also made to characterize the vertical thermal gradient of the furnace within the area 5.1 cm (2”) above and below the vertical center of the furnace. The wire mesh/thermocouple system was moved after measuring a steady-state temperature at each height, and the measurements were compared. However, one major issue that occurred was the tripping of the breaker during tests. Because the wire mesh, the thermocouple wires, and the large internal pipe inside of the furnace were made out of metal, and the DAQ and furnace were both running electricity through the thermocouple wires and furnace pipe, respectively, the breaker would trip if either of these objects came into contact, as a safety measure. Initially, insulation was wrapped around the periphery of the wire mesh in order to mitigate this contact. However, the insulation impeded the flow of the rising hot air, and artificially reduced the thermal gradient between the thermocouple locations on the wire mesh. Wrapping the thermocouple wires individually had a similar effect. Another solution was that the mesh could be rotated between height changes such that the mesh would not touch the pipe wall, and therefore the furnace could be heated back up to the same

temperature at this time of no-contact. Due to limits in the experimenter's dexterity, this proved to be too difficult to accomplish.

The eventual solution simply involved leaving the furnace off, so that the DAQ was able to record data without worries of losing power if the breaker was tripped. Figure 2.8 shows the temperature difference between the furnace and the three thermocouples, where the mesh was moved down one inch at the time indicated by each red dotted line. The cooling of the furnace, and therefore, the thermocouples is evident when the furnace was turned off.

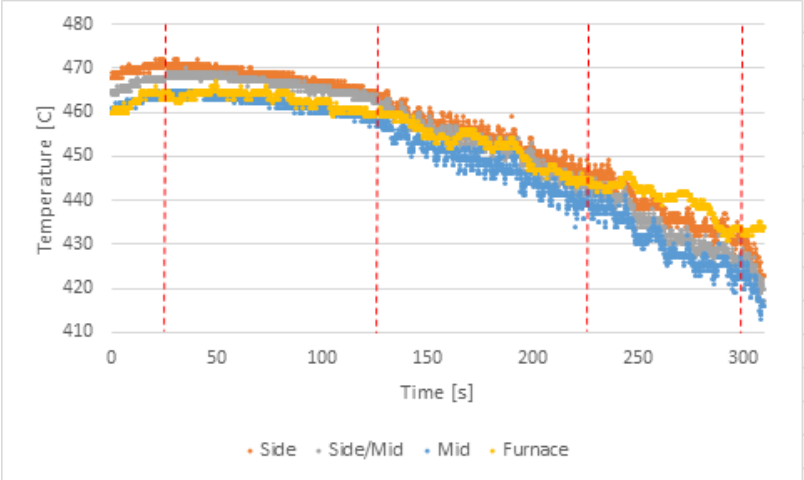

Figure 2.8: Temporal gradient in furnace at various heights

The average of the three thermocouples during each height interval is plotted in Figure 2.9. Because the furnace was cooling while measurements were made, it is difficult to separate the effect from the furnace cooling and the effect from the vertical axis temperature gradient.

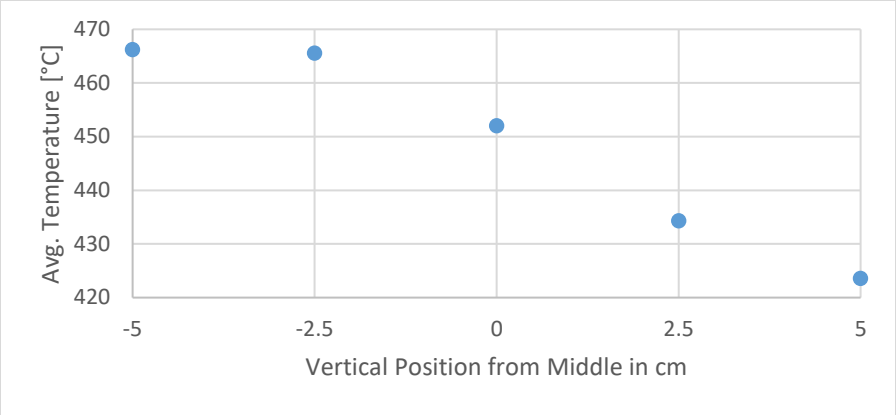

Figure 2.9: Average temperature at various heights in furnace

In order to make a more comparable result, the difference between the average furnace temperature and the average thermocouple temperatures were also plotted in Figure 2.10. This is not ideal, but it can at least give some insight into the magnitudes of the different temperatures at each height. The length of the initial dowel was five centimeters (1.97”), and therefore, the difference between the top and bottom of the dowel may only be about 9 degrees, if Figure 2.10 is referenced using the difference between the temperatures at 2.5 cm above and below the furnace middle. As a high estimate, the temperature difference between the top and bottom portion of the dowel could be 30 degrees if Figure 2.9 is referenced, though this is probably higher than what would be expected due to the effects of the cooling furnace in this experiment. In hindsight, it would have been easier to use a single stiff thermocouple, such as one that was sheathed, to measure the center temperature at each height, since an idea of the horizontal temperature gradient was already known.

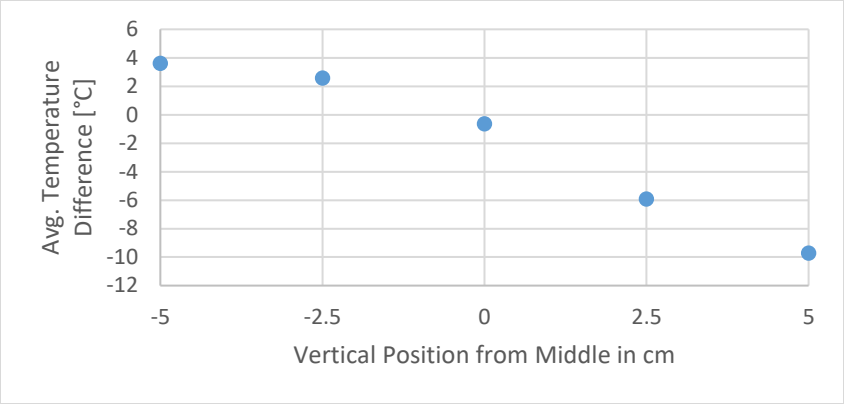

Figure 2.10: Average temperature difference between furnace and thermocouples at various heights in furnace

Leaving the ember inside of the furnace for a longer period of time did not affect the overall shape or quality, but merely affected the exit size. Once the ember reached the desired exit diameter of 6.4 mm, the ember was removed from the furnace, and placed onto the fuel bed inside of the air flow chamber below, Figure 2.11. The air flow chamber was constructed from a Plexiglas box with a hole machined on the bottom which was attached to a Shop Vacuum Corporation Wet/Dry Model 500A, 1.25 HP shop vacuum. Additionally, an aluminum lid with a centered hole was used to cover the box, allowing air to flow through the top of the box over the fuel bed, and into the vacuum. By controlling the vacuum's voltage with a variac, that was monitored using a multimeter, a range of air flow conditions could be achieved. Additionally, a layer of beads was used as a flow conditioner, improving the uniformity of the air flow.

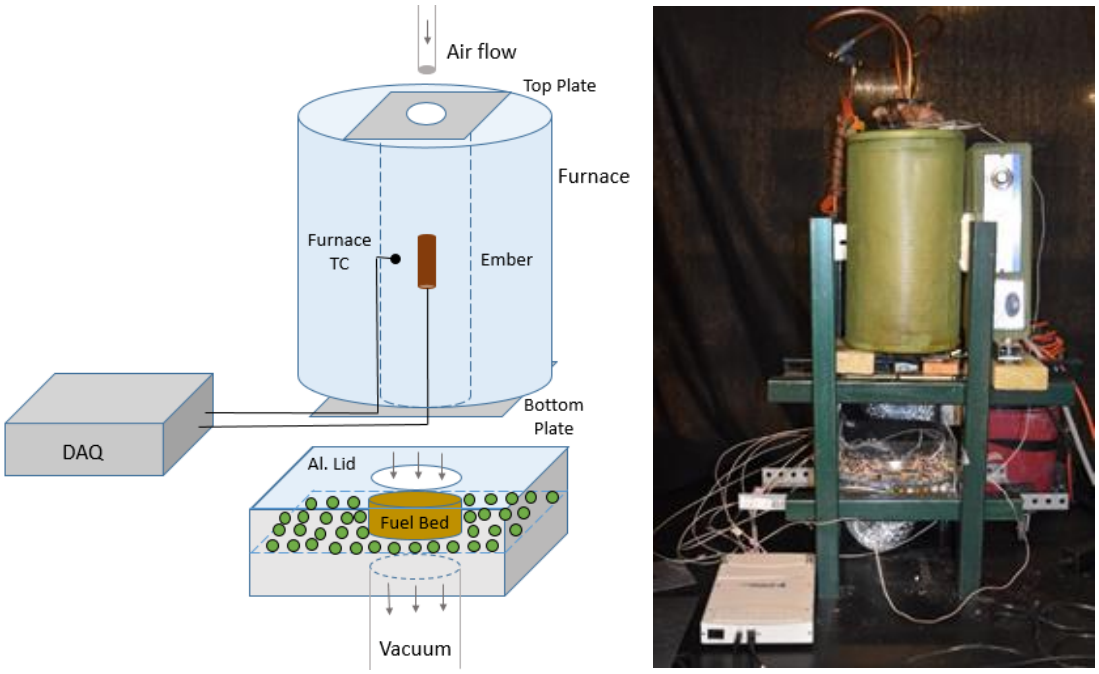

Figure 2.11: Furnace experimental schematic and photograph

During the larger ember tests, the ember was laid horizontally on the fuel bed during tests. In the case of the metal-mesh basket, the large ember was maneuvered from the basket, through the vacuum chamber's orifice, and onto the fuel bed using tweezers, seen in Figure 2.12a. In the case of the thermocouple attached ember, the thermocouple wire was bent backwards, as in Figure 2.12b, allowing for an easier placement through the vacuum chamber orifice and onto the fuel bed. The full procedure can be found in Appendix A. The procedure for the fragmented ember process will be discussed later.

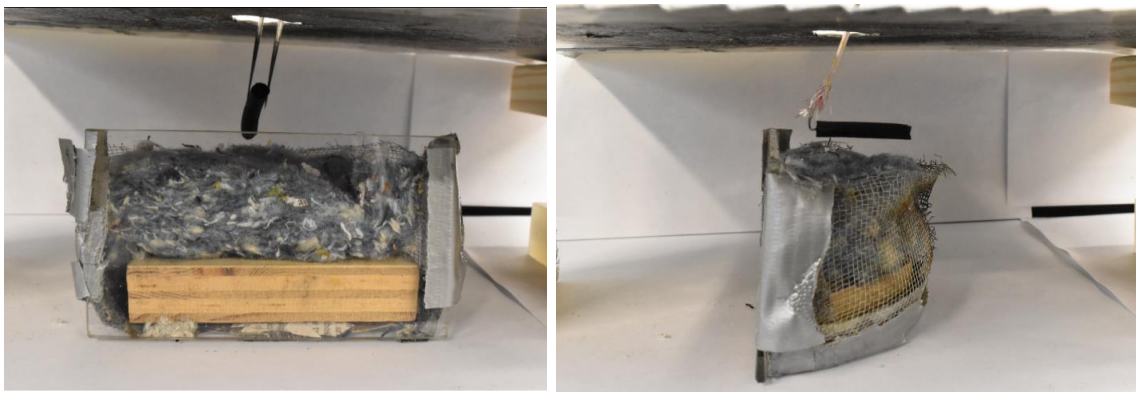

Figure 2.12: a) Picture of Maneuvering ember from basket to Fuel Bed b) Picture of Bent thermocouple

Flow was characterized using two differential pressure transducer probes, with one leg measuring ambient pressure and the other measuring pressure through a hole in the side of the chamber. The velocity of the air was calculated using Eq. 2.5 by treating the system as an orifice plate system, where V_1 is the velocity of the air inside the air flow chamber, C_d is the discharge coefficient, P_2 is the pressure inside of the air flow chamber, P_1 is the ambient pressure, ρ_{air} is the density of the air, and β is the ratio between the diameters of the orifice plate and the "pipe". C_d was set to be 0.6 based on the Reynold's number, and a negligible β.

$$V_1 = C_d \sqrt{\frac{2*(P_2-P_1)}{\rho_{air}(1-\beta^4)}} \tag{2.5}$$

A second Plexiglas box was also designed with an IR transmissive window to allow for IR imaging, and the fuel bed was embedded with three thermocouples, as seen in Figure 2.13. The fuel bed was cut to be a 10.2 cm (4") diameter half circle with a thickness of 2.5

cm (1”). Two thermocouples were located one cm (0.4”) from the top, where one was located one cm (0.4”) to the left of the ember, and the other was located two cm (0.8”) to the left of the ember. A third thermocouple was also placed one cm (0.4”) from the bottom of the fuel bed, one centimeter (0.4”) away from the center as well. The thermocouples were placed off-center of the ember, as the thermocouples would obstruct the degradation path of the ember if placed in its way. The fuel beds were then placed on top of a similarly shaped piece of wood to match the boundaries found in an attic, and were constrained by a mesh during tests. Finally, the fuel beds were sectioned off using a piece of glass. In this manner, a cross-sectional view of the insulation could be seen as they underwent the various ignition events, allowing for a better understanding of these processes, as seen in the front view in Figure 2.13.

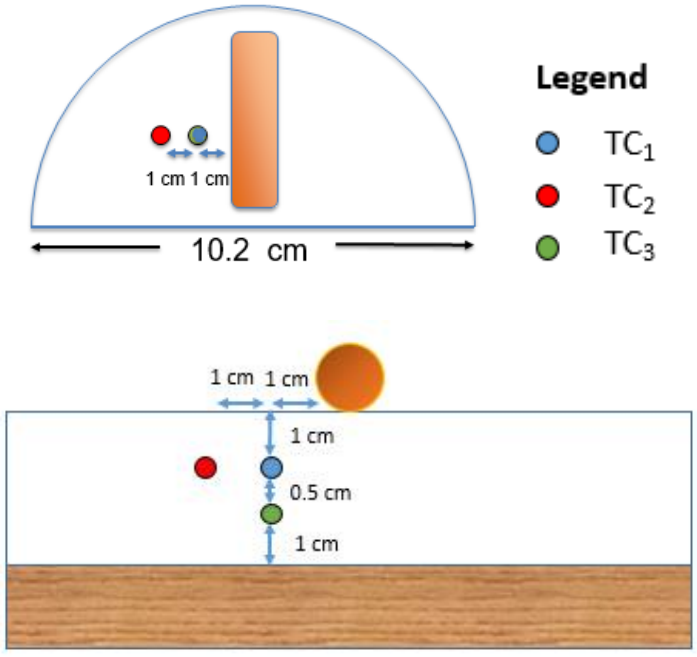

Figure 2.13: Top view (top) and front view (bottom) of thermocouple placement in fuel bed in relation to ember placement

The five main types of insulation tested were Ultratouch denim insulation, Greenfiber loose-fill cellulose, Dow Great Stuff Big Gap Filler Polyurethane spray foam (PUR), Owens Corning FOAMULAR 250 extruded polystyrene (XPS), and Cellofoam Poly Panel expanded polystyrene (EPS), all of which had flame retardants in them and were available commercially. The methodology for making the PUR can be found in Appendix B. Non-flame retarded (NFR) denim, obtained from Airgas, and non-flame retarded (NFR) cellulose, in the form of shredded newspaper, were also tested due to an interest in the behavior of their flame retardant counterparts. It can be noted that these insulations can be further categorized into two separate classes. The cellulosic class of insulation consists of denim and cellulose, while the polymeric class of insulation consists of PUR, EPS, and XPS. Ignition cases were tested at three different air flow speeds, 0 m/s, 2.4 m/s, and 4.8 m/s, and were tested three times each for repeatability. The set of experiments was tested for both the large ember and the fragmented ember cases, where the total mass of the dropped fragmented embers was equal to the mass of a single large ember.

2.2.2: Measurement Calibration

The range of temperatures that the ember underwent was approximately 700 °K – 800 °K. Typically, if one is looking at small ranges of temperatures behind an infrared transmissive window, a constant transmission correction can be applied with a proper calibration. However, because the range of temperatures was large and the IR transmissive window did not have a constant transmission curve across the wavelengths of interest, a calibration process was used to correct for the temperatures observed by the IR camera.

The calibration was performed by first attaching a thermocouple to a piece of oxidized steel. The emissivity of the steel was measured to be 0.88 by adjusting the emissivity setting on the IR camera until the observed temperature matched the thermocouple temperature. The steel was then heated up in an oven at different temperatures, taken out and placed behind the IR transmissive window, and the corresponding IR camera temperatures and thermocouple temperatures were recorded, as seen in Figure 2.14. This correction was then applied to the IR temperature readings during testing.

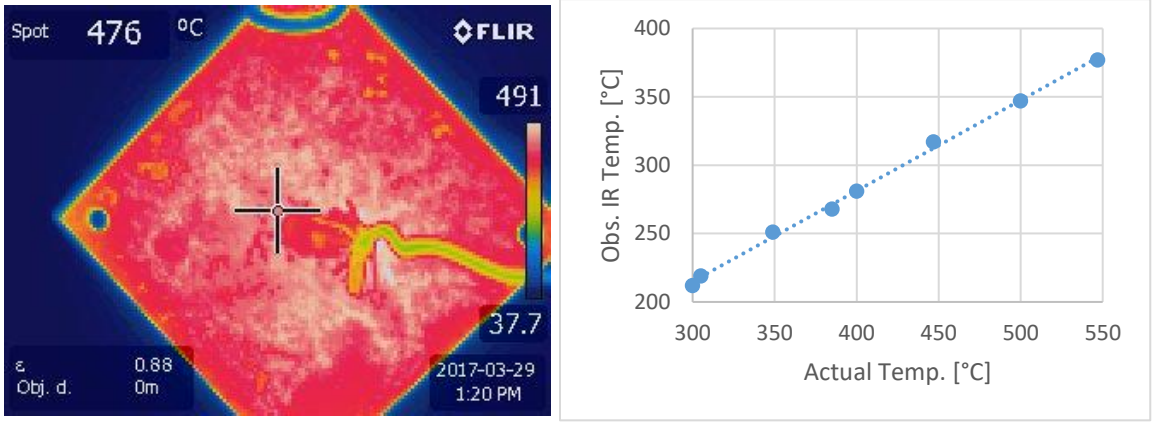

Figure 2.14: a) IR image of steel plate b) Calibration curve of IR camera temperature vs. thermocouple temperature

The emissivity of the ember was measured by covering part of a cooled ember with black tape with a known emissivity of 0.95. The ember was then heated up on a hot plate, and the temperatures were monitored using the IR camera. Once the ember temperature had reached steady state, the emissivity setting in the IR camera was changed until the temperature of the non-taped portion of the ember matched the known temperature from the taped portion. The emissivity of the ember was measured to be 0.8, which matches the range of values, 0.68-0.85 obtained by Suuberg et al. [10] for charring materials. There was

not enough time to create another calibration curve with an emissivity closer to the ember's emissivity, but this should be done in the future.

2.2.3: Sample Conditioning

In order to keep tests consistent, the embers were conditioned in a humidity chamber, seen in Figure 2.15. The humidity chamber was constructed from a 45-quart Styrofoam cooler and an Air Innovations Cool Mist Personal Humidifer Mh-103 connected to an IMAGE Digital Air Humidity Controller Sensor WH8040. It was found that the humidity could be kept to ±2% relative humidity over a tested range of 60%-80%. The chamber was lined with aluminum foil to minimize permeation of water through the walls and the lid was also sealed with vacuum grease. In order to achieve humidities lower than the ambient room relative humidity, pans of desiccant were placed inside of the chamber.

Figure 2.15: a) Humidity chamber exterior b) Humidity chamber interior

The dowels used in our experiments were first conditioned at two relative humidities, 70% and 80%, at a temperature of 22 °C. The dowels were conditioned in the chamber for three days, as this resulted in a moisture content change less than 0.5%

between daily measurements. The time to condition samples could be made more exact if the moisture content was checked more frequently. Using an oven heating moisture content test, it was found that these relative humidities resulted in an average moisture content of 10.89% and 14.11%, respectively. The standard deviations of the moisture contents were 0.36% for the 70% relative humidity and 0.9% for the 80% relative humidity, where both cases tested ten samples each. The larger standard deviation of the 80% moisture content test, compared to the 70% moisture content test, can be explained by Figure 2.16, where moisture content is more sensitive at higher relative humidities [11]. The moisture content of our samples do not match those found in Figure 2.16, but this could be due to the differences in wood used because the type of wood was not mentioned. It was concluded that the dowel conditioning would be done at 70% relative humidity. In Manzello's experiments, the embers had a moisture content of 18% [3].

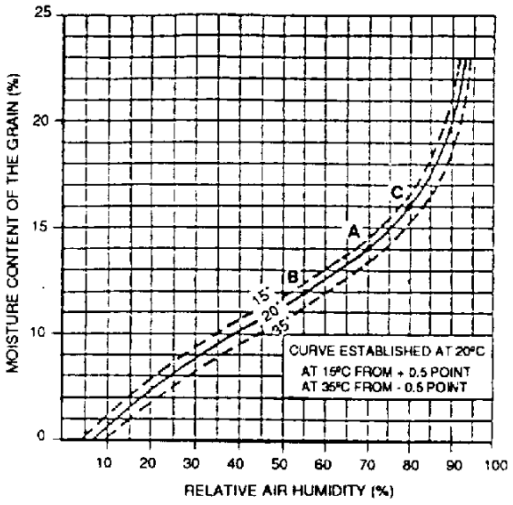

Figure 2.16: Moisture content vs. relative air humidity for wood [11]

The ideal generated ember was one that was symmetrical, had all surfaces glowing red, and without cracks. Initially, many weeks were spent trying to create this ideal ember. Temperatures within the furnace were continually monitored, and the effects of air flow were observed. However, the success rate of achieving an ideal ember fluctuated between 1 out of every 4-8 tests at the time, where samples would often leave the furnace looking like Figure 2.17. This did not include the challenge of properly transitioning the ember to the fuel bed.

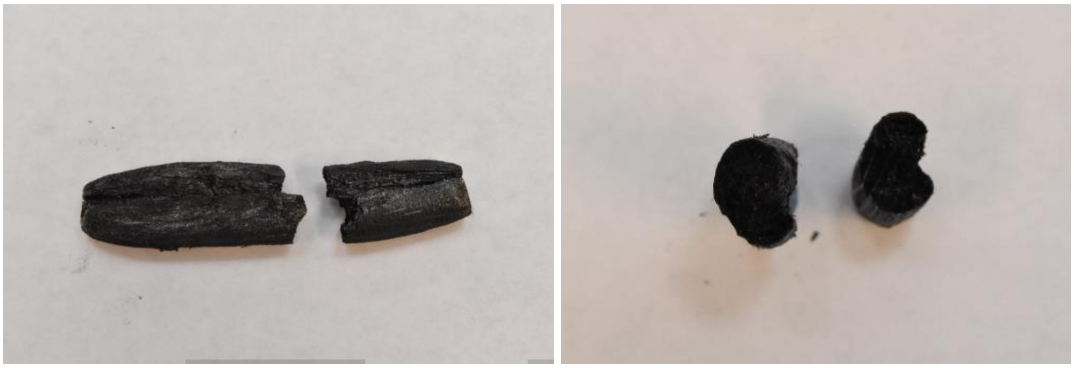

Figure 2.17: Stress induced crack from drying

The Food and Agriculture Organization of the United Nations noted that rapid drying can create internal tensions, which inevitably lead to ruptures and asymmetry in the grain. Therefore, rather than conditioning the large embers in the humidity chamber, they were dried in an oven at 105 °C for at least one hour leading to the embers seen in Figure 2.18, which are more symmetrical and exhibit little stress induced cracking.

Figure 2.18: Quenched ember samples (a) large ember samples and (b) fragmented ember samples

There was an initial consideration in the size of dowels to use, and at that point, tests were conducted on 5 mm (0.2”) and 10 mm (0.4”) samples. Later, only 10 mm diameter dowels were used for ignition testing. Three dowel samples, one 5 mm (0.2”) diameter and two 10 mm (0.4”) diameter, were dried in the oven until the mass remained unchanged by 0.5%. The moisture content was calculated where W_{wet} is the weight of the wet dowel and W_{dry} is the oven dried weight.

$$MC = \frac{W_{wet} - W_{dry}}{W_{dry}} * 100\% \tag{2.6}$$

Figure 2.19 shows the moisture content of the three dowels over a period of six hours. The dowels seem to follow similarly shaped drying curves. It should be noted that the 5 mm (0.2”) diameter dowel should have dried faster than the larger dowels though, since the diameter was smaller, and thus the water transport distance was smaller; however, none of the dowels tested were conditioned in the humidity chamber, and thus the 5 mm (0.2”) dowel’s initial moisture content was 5% higher than the 10 mm (0.4”) dowel’s

moisture content. It can be seen that after four hours in the oven, the moisture contents of the dowels were unchanging. The four hour mark was thus set as a standard for how long the dowels should be left in the oven before testing.

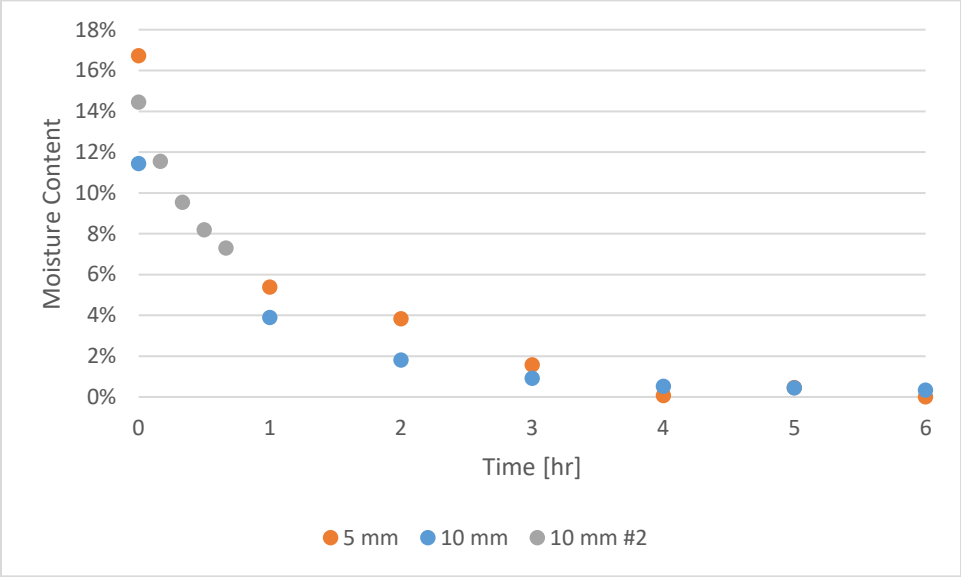

Figure 2.19: Drying progression of three dowels (two of 10 mm diameter and one of 5 mm diameter)

2.2.4: Fragmented Ember Generation

An alteration to the baseline apparatus was made to allow for the production of smaller embers that more closely mimicked those that would be seen to penetrate an attic vent mesh. The equivalent mass of fragmented dowels prior to heating, were to be used in place of the larger dowel, which in our case took five fragmented embers. Two approaches were attempted. The first approach involved positioning a 6.4 mm (¼”) mesh on the inside of the furnace at the vertical center of the furnace and dropping fragmented dowels onto this mesh from the open top of the furnace, as seen in Figure 2.20a. The dowels would then

go through the heating, pyrolysis, and oxidation process until they were small enough to fall through the 6.4 mm (¼") mesh. A mesh chute was used to further guide these embers onto the fuel beds located within the air flow chamber, as seen in Figure 2.20b.

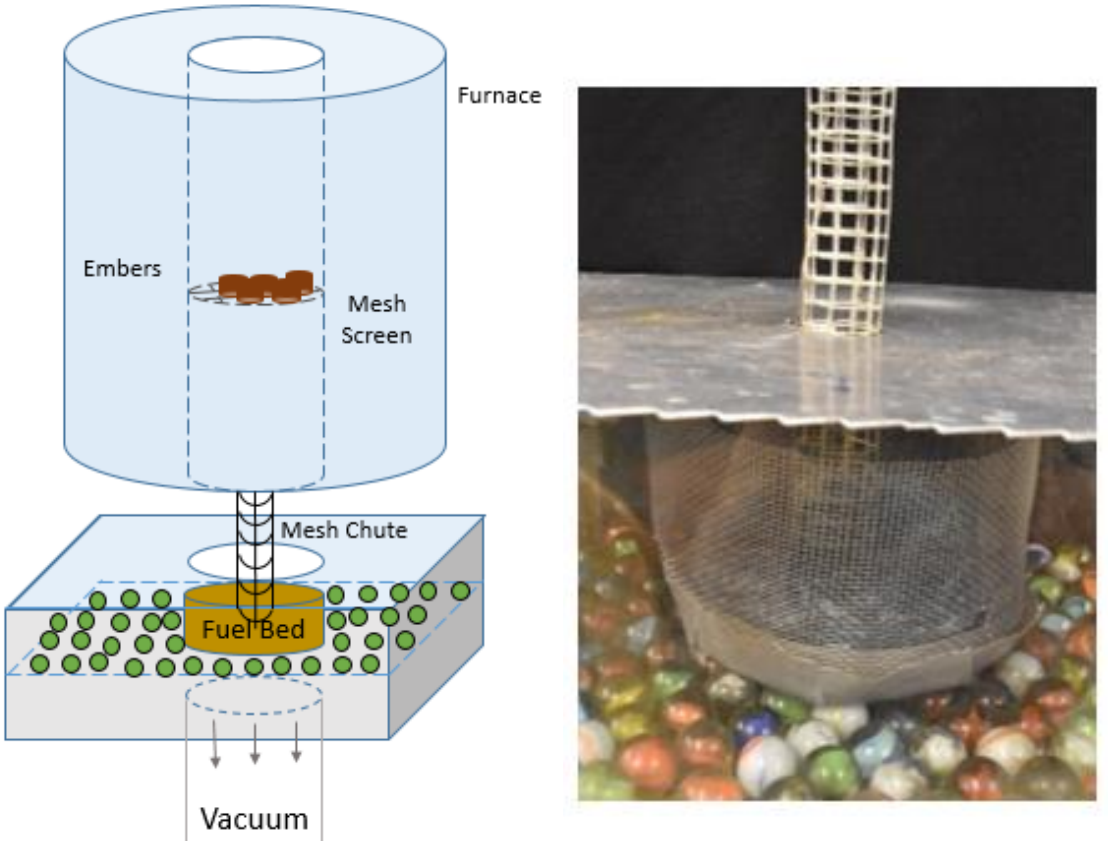

Figure 2.20: a) Schematic of inner mesh screen setup b) Image of mesh chute for embers

One issue with this approach was that the embers would oxidize too quickly and would simply burn up, leaving no mass of ember to fall through the mesh, and onto the fuel bed. Therefore, the air flow was switched with a nitrogen flow in order to slow the oxidation process. The nitrogen, however, prevented any oxidation from occurring and did not allow any of the embers to burn through the mesh. It was later found that reverting back to air, but at a higher air flow, 100 SCFH – 400 SCFH (47.2 l/min – 188.8 l/min), was able

to achieve a higher ember yield. The air flow essentially pushed the embers onto the mesh, until they were small enough to fit through the mesh and fall onto the fuel bed, so there were no issues with the embers becoming burnt up or quenched.

The inner mesh of the furnace was removed, and the ember temperature was measured for the varying furnace air flows and was plotted in Figure 2.21. A large ember was used in this case, as they were easier to instrument with a thermocouple, compared to the fragmented embers. The peak ember temperature increased with increasing air flows, although increasing the air flow from 300 CFH to 400 CFH actually decreased the peak temperature, most likely due to the increased convective cooling. The duration that the ember could keep its elevated temperature decreased with increasing air flow. Oxidation caused both of these effects, as an increased air flow increased the rate of oxidation as well as caused the ember to degrade at a faster rate.

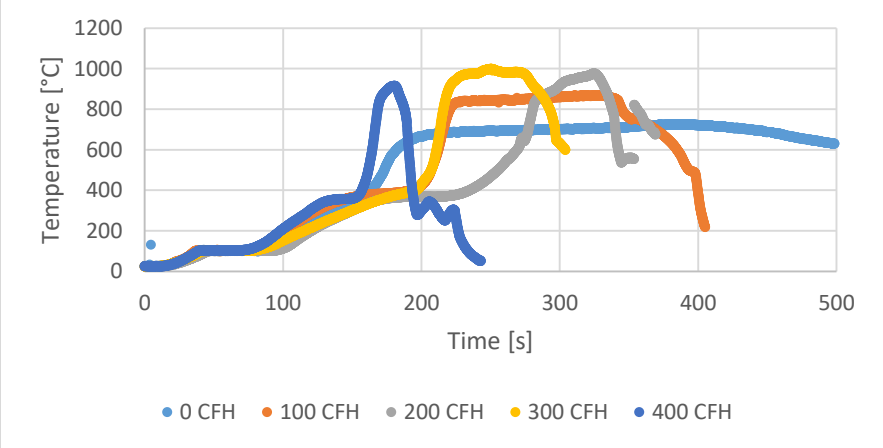

Figure 2.21: Ember temperature with varying furnace wind speeds with furnace temperature of 450 °C

The inner mesh was placed back into the furnace and the effects of air flows on the percentage of embers that fell through the mesh, as well as the total ember exit mass was

measured. These results can be seen in Figure 2.22 where the percentage of embers that had exited, out of five embers, at certain furnace wind speeds are plotted. Figure 2.23 shows the total mass of all of the embers that had exited, after being quenched in a nitrogen-filled beaker. The wind speeds were measured using an anemometer, as the air flow meter had not been installed yet.

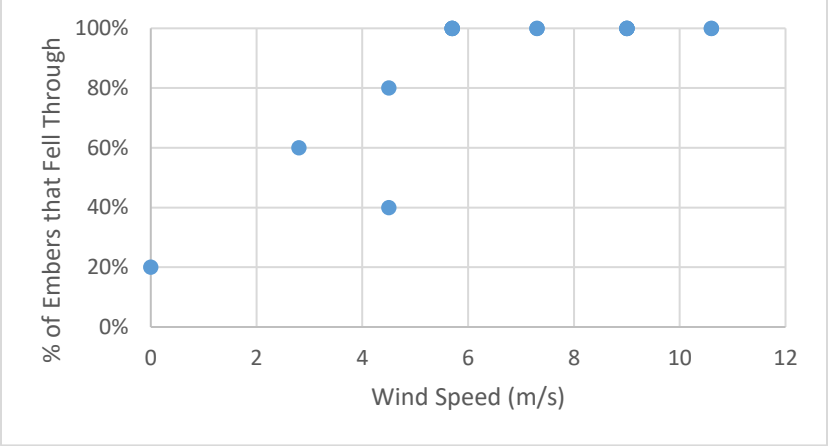

Figure 2.22: Number of embers exiting the furnace at various furnace wind speeds

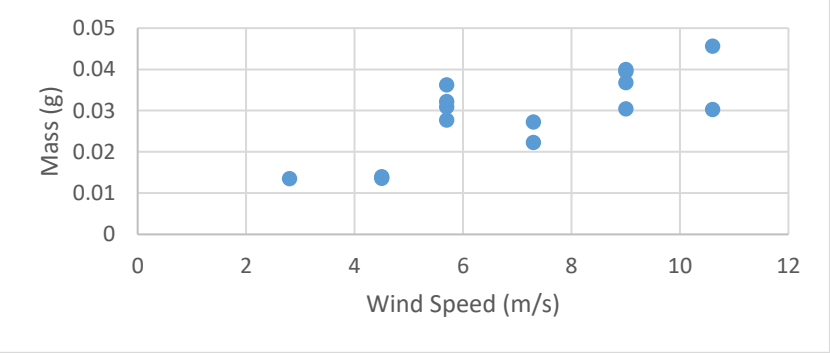

Figure 2.23: Total mass of exiting embers at various furnace wind speeds

One of the biggest issues with this approach was the lack of consistency with the time that it took for embers to fall through the mesh. During some tests, the embers would all fall through within five to ten seconds of each other. However, more often than not,

there would be thirty second intervals between the falling of subsequent embers, where the prior embers had already burnt out on the fuel beds. Therefore, there was a need for a more repeatable process.

For the second approach, a mesh bucket was used to hold the fragmented dowels within the furnace during their heating phase, seen in Figure 2.24, similar to the methodology used with the larger embers. The air flow was reverted back to the standard 22 SCFH. Once the embers reached roughly 6.4 mm after 200 seconds, the bucket was extracted from the furnace and the embers were dumped onto the fuel bed being tested within the air flow chamber. The mesh bucket with embers were left in the furnace for different lengths of time to find the length of time that produced embers closest to this size. This approach helped to improve the repeatability of the previous tests.

Figure 2.24: Mesh bucket used to transport fragmented embers into and out of the furnace

The viewing perspectives of the various recordings made during testing can be seen in Figure 2.25. The viewing perspective used for all of the shredded paper and mulch tests used perspective A, while all of the insulation tests used perspective B.

Figure 2.25: Perspective A for shredded paper and mulch tests (left) and Perspective B for all other insulation tests

There were no ignition events observed when the embers were dropped onto the fuel bed in a random orientation. The embers did not appear to have the energy or mass necessary to cause an ignition by themselves. Figure 2.26 shows two different tests, one monitored using an IR camera and the other monitored using a DSLR camera, where the five fragmented embers simply glowed, but did not cause ignition on the FR-denim.

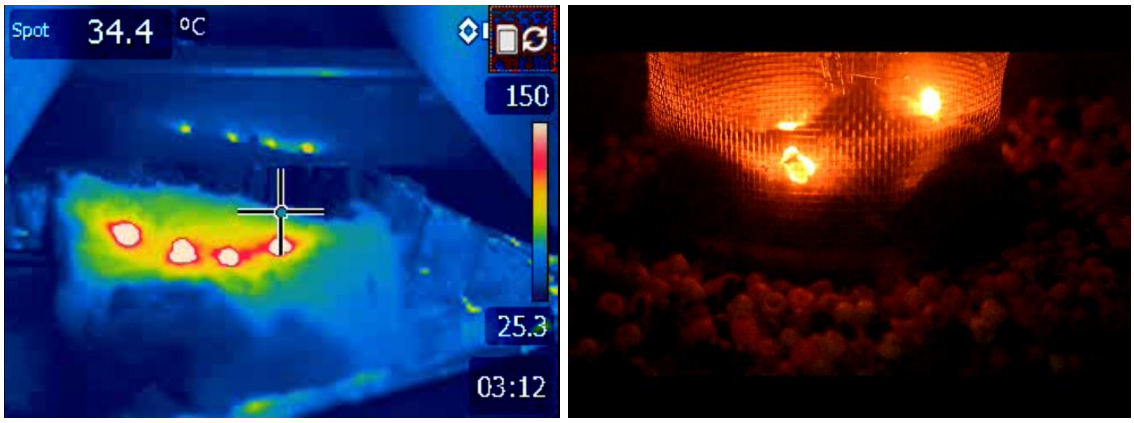

Figure 2.26: a) IR image of randomly dropped embers onto FR-denim fuel bed b) Visible image of randomly dropped embers onto FR-denim fuel bed

We hypothesize that during a wildfire event, one of the pathways to ignition could occur if a critical number of fragmented embers is able to penetrate the attic and form an ember pile in the attic space. The ember pile is more likely to maintain its temperature and have a higher likelihood of igniting materials, compared to a random scattering of embers. In order to replicate this, a cylindrical mesh was placed on top of the fuel bed, which was used to keep the embers in a pile as they fell, and the viewing perspective can be seen in Figure 2.27.

Figure 2.27: Perspective of embers constrained by mesh

The parameter space that was tested can be seen in Tables 2.1-2.3.

Table 2.1: Ember temperature testing parameter space

Ember Size	Furnace Temperature	Measurements	# of Tests Performed
Large	400 °C – 700 °C	Ember temperature	3

Table 2.2: Shredded paper and dried mulch ember ignition testing parameter space

Ember Size	Ember State	Furnace Temperature	Fuel Bed	Measurements	# of Tests Performed
Large	Glowing	420 C	Shredded Paper	IR temperature, Fuel bed temperatures	1
Large	Flaming	500 C	Shredded Paper	IR temperature, Fuel bed temperatures	1
Large	Glowing	420 C	Dried Mulch	IR temperature, Fuel bed temperatures	1
Large	Flaming	500 C	Dried Mulch	IR temperature, Fuel bed temperatures	1

Table 2.3: Insulation ember ignition test parameter space

Ember Size	Fuel Bed	Furnace Temperature	Air Flow Speed	Measurements	# of Tests Performed
Fragmented & Large	FR-Denim	420 °C	0 m/s, 2.4 m/s, & 4.8 m/s	IR temperature, Fuel bed temperature, DSLR recording	3 each
Fragmented & Large	FR-cellulose	420 °C	0 m/s, 2.4 m/s, & 4.8 m/s	IR temperature, Fuel bed temperature, DSLR recording	3 each
Fragmented & Large	XPS	420 °C	0 m/s, 2.4 m/s, & 4.8 m/s	IR temperature, Fuel bed temperature, DSLR recording	3 each
Fragmented & Large	EPS	420 °C	0 m/s, 2.4 m/s, & 4.8 m/s	IR temperature, Fuel bed temperature, DSLR recording	3 each
Fragmented & Large	PUR	420 °C	0 m/s, 2.4 m/s, & 4.8 m/s	IR temperature, Fuel bed temperature, DSLR recording	3 each
Fragmented & Large	NFR-denim	420 °C	0 m/s, 2.4 m/s, & 4.8 m/s	IR temperature, Fuel bed temperature, DSLR recording	3 each
Fragmented & Large	NFR-cellulose	420 °C	0 m/s, 2.4 m/s, & 4.8 m/s	IR temperature, Fuel bed temperature, DSLR recording	3 each

2.3 Results and Discussion

2.3.1: Ember Characterization

A sample of eight large ember diameters was measured after being left inside of the furnace for 200 seconds. Once the ember had reached the desired size, it was taken out of the furnace and placed immediately into a beaker with a flow of nitrogen directed onto the ember to quench the chemical reactions. The mean diameter of a sample of eight large embers was 5.99 mm (0.236”) with a standard deviation of 0.432 mm (0.017”). The main objective was to achieve a typical ember diameter of 6.44 mm (1/4 ") as this was the size of a typical attic mesh, and therefore this methodology was deemed acceptable.

The distributions of size and mass of a sample of 24 fragmented embers was compiled into a histogram, seen in Figure 2.28. The Freedman-Diaconis rule was used as a guideline to pick the bin width, h, and the number of bins, BN, for the histograms where n represents the number of observations, where IQR is the interquartile range, n is the number of samples, and max – min is the range of the sample values [12].

$$h = 2 * IQR * n^{-\frac{1}{3}} \tag{2.7}$$

$$BN = \frac{Max-Min}{h} \tag{2.8}$$

The final length and width of the fragmented embers were averaged for each of the embers to consolidate the dimensions, and was the main parameter describing size in the histogram. This gives a more meaningful description of the final ember size, as it shows

how large each ember was on average, as opposed to having the final lengths and widths being plotted separately. The average final dimension of the embers was 6.61 mm (0.260”) with a standard deviation of 0.41 mm (0.016”), while the average mass was 0.040 grams with a standard deviation of 0.008 grams. This falls close to the targeted 6.35 mm (0.25”) mesh size. Furthermore, the average final mass of the large ember was 0.311 grams, while the average final mass of the set of five fragmented embers was 0.200 grams. More mass was lost to volatilization for the fragmented embers, most likely due to the geometry and the higher surface area available to heating and oxidation. MATLAB’s Image Processing Toolbox was also used to find the projected area of the embers, in order to automate the process, found in Appendix C.

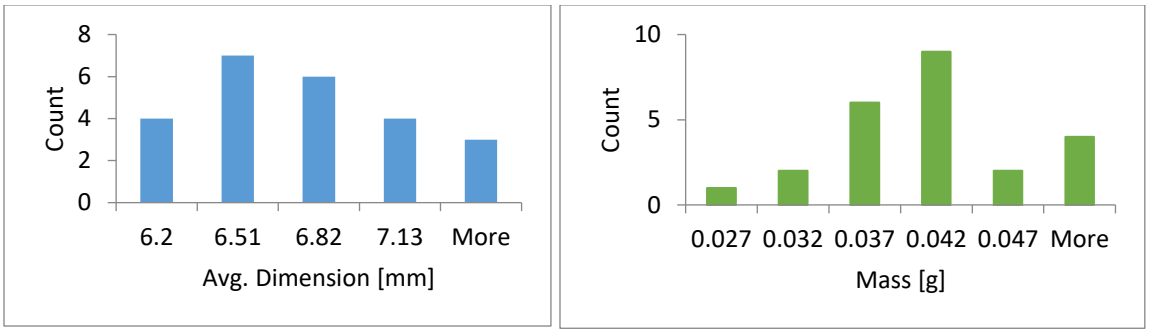

Figure 2.28: a) Distribution of the average final dimension of the fragmented embers
b) Distribution of the average final mass of the fragmented embers

2.3.1.1 Transient ember response

Creating consistent embers was important to generating reproducible and meaningful results. The centerline temperature evolution of five different large embers within a furnace at a temperature of 450 °C was monitored. The results can be seen in Figure 2.29, where the graph is started once the ember enters the furnace. One should notice

that each heating curve appears to have three stabilization points. The stability near 100 °C is due to the effects of drying, with the duration depending on the initial moisture content of the dowel. There is a sudden change in heating around 400 °C that is associated with exothermic reactions around the ember, and is often accompanied by a temporary flaming reaction. The ember's internal temperature stabilizes around 700-800 °C, due to the balancing effects of the oxidative reactions and convective & radiative cooling. At this point, the ember has transitioned to a glowing state.

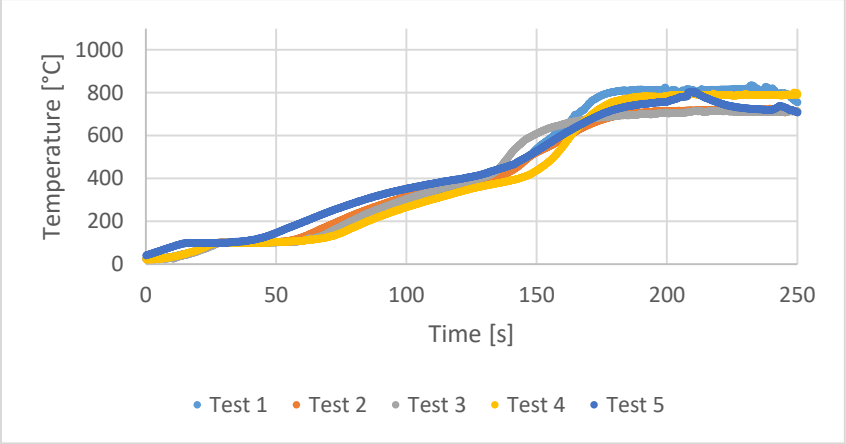

Figure 2.29: Centerline temperature of wooden elements in furnace at 450 °C

This trend looks similar to trends found by Poespowati [13], seen in Figure 2.30, after performing surface temperature measurements on wooden blocks with an external heat flux of 22 kW/m^2.

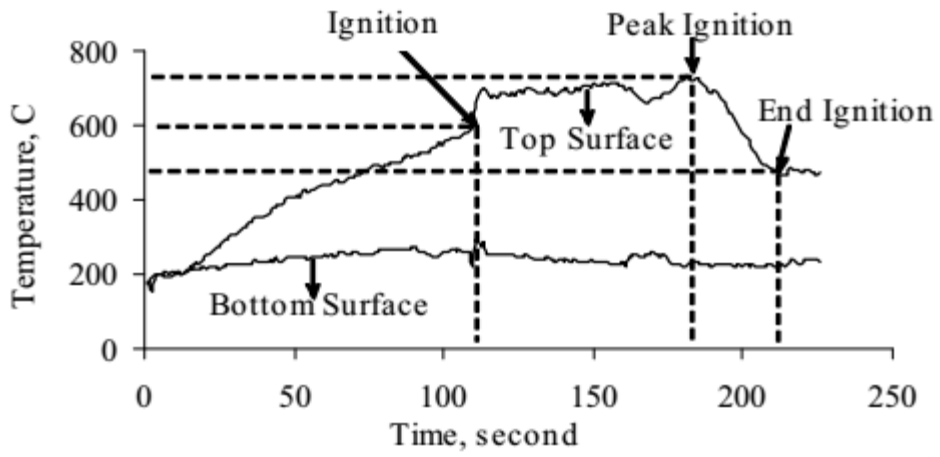

Figure 2.30: Surface temperature of wooden blocks with external heat flux of 22 kW/m^2 [13]

Furnace tests were also performed at temperatures between 400 °C and 700 °C, and can be seen in Figures 2.31-2.34. It should be noted for almost all of the temperatures, the ember goes through both the drying phase at 100 °C and the plateau region around 400 °C. The embers also reach a consistent peak temperature for each furnace condition. However, the peak temperatures increase, once the furnace temperature is increased past 600 °C. Furthermore, the ember takes longer to reach its peak temperature at lower furnace temperatures, compared to the higher furnace temperature conditions.

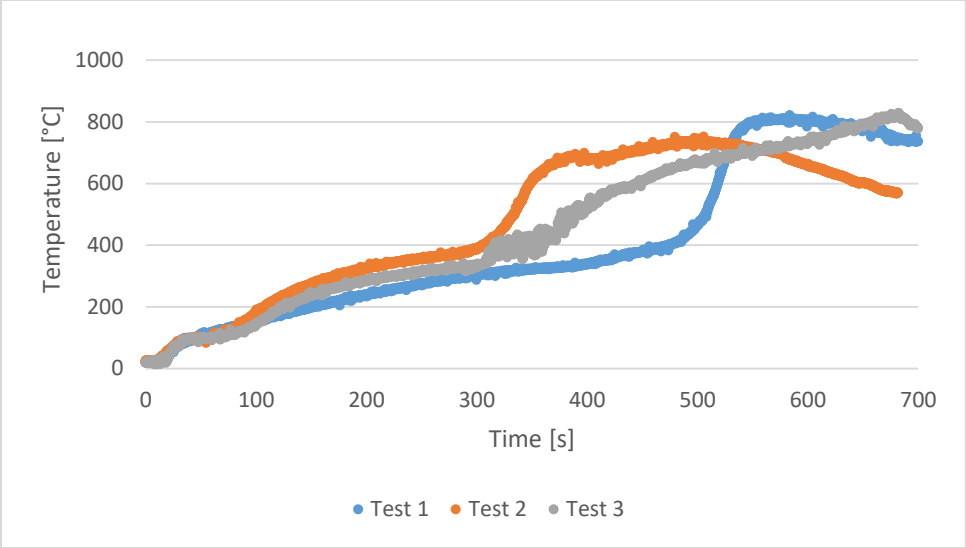

Figure 2.31: Centerline temperature of wooden elements in furnace at 400 °C

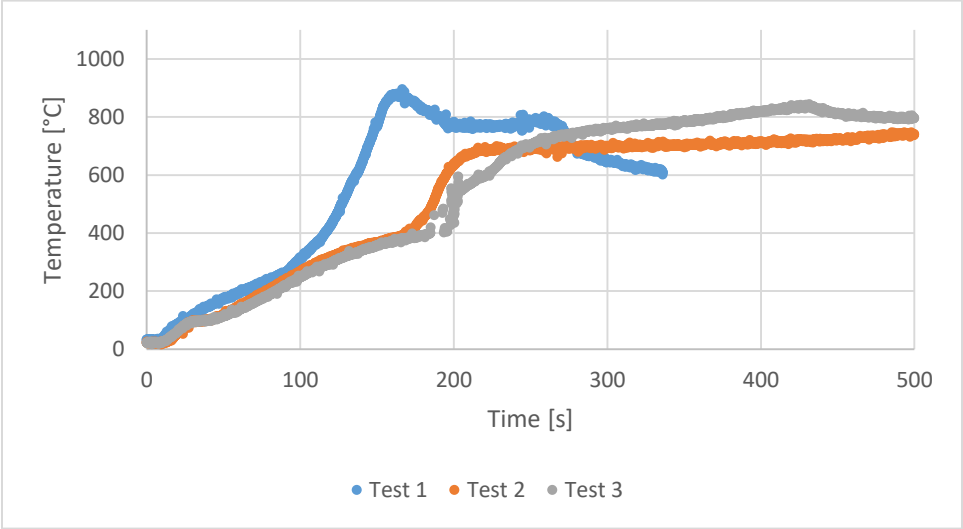

Figure 2.32: Centerline temperature of wooden elements in furnace at 500 °C

Test 1 in Figure 2.32 shows an anomalous peak around 175 seconds. The source is unknown, but it could possibly be due to a cracked ember. When the ember cracks, the thermocouple can be exposed to flames produced by the ember, thus resulting in an increase in temperature. For the cases shown in Figures 2.32-2.33, the thermocouple traces

showed intermittent noise, and therefore, the data had to be filtered using a gradient-threshold method. The maximum gradient observed in any of the normal tests was used as the gradient-threshold for the filter. Furthermore, during test three at a furnace temperature of 600 °C (Figure 2.33), the DAQ did not begin recording until after the ember had started drying, and so the test was aligned using the time at the end of the drying phase of the other tests as a reference point.

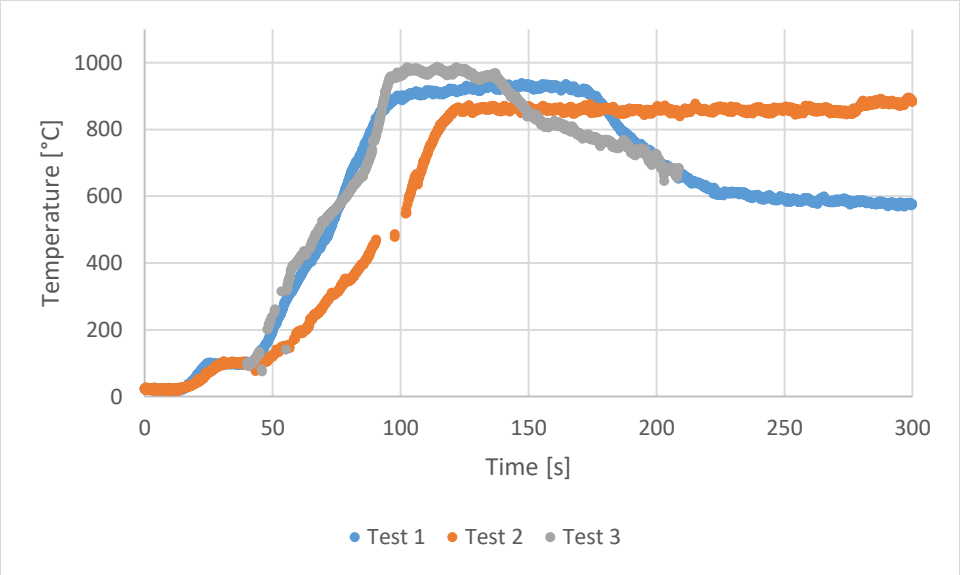

Figure 2.33: Centerline temperature of wooden elements in furnace at 600 °C

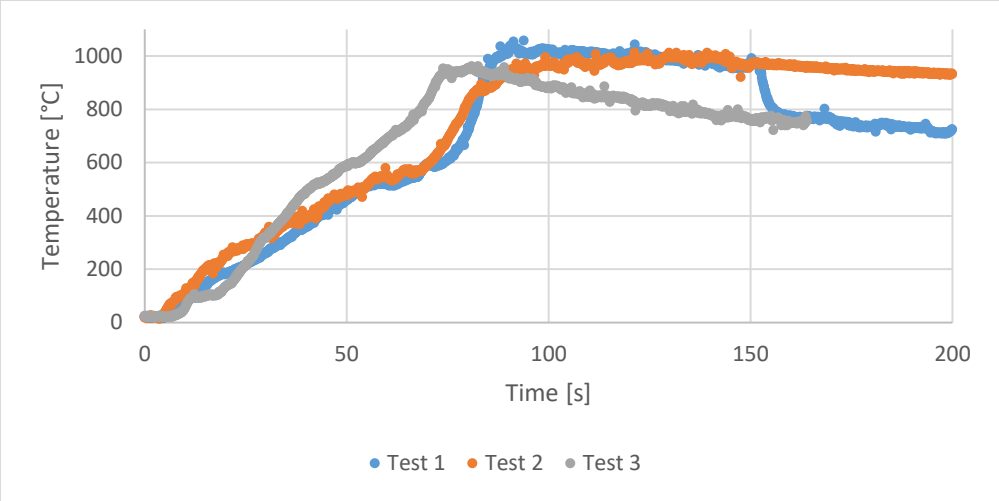

Figure 2.34: Centerline temperature of wooden elements in furnace at 700 °C

The embers tested at the 350 °C and 400 °C furnace conditions heat up slowly, and take at least five minutes before they start glowing inside of the furnace. When the temperature is raised to at least 420 °C, flaming ignition of the ember occurs inside of the furnace, which is followed by a full-bodied glow once the flames extinguish. The flames likely extinguish due to a decreased pyrolysis rate. This internal temperature of the ember when this ignition occurs is typically around 400 °C, and can be seen to align well with results from Melinek (1969) in Figure 2.35 [14]. The comparison may be reasonable since the dowels might be considered to be thermally thin and the centerline temperature is a reasonable approximation of surface temperature. The ignition temperatures observed by the researchers have a fairly large spread, which can mainly be attributed in the methodologies they used to measure ignition temperatures (e.g. pyrometer, surface-thermocouple) and also how they heated the samples (e.g. furnace vs. radiant heater).

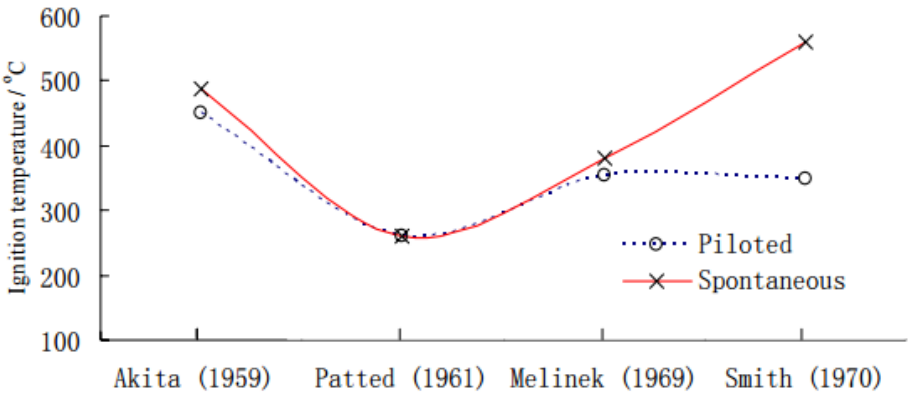

Figure 2.35: Comparison between piloted and spontaneous ignition surface temperature of samples by different investigators [14]

2.3.2 Preliminary Testing Results

Once the embers were shown to have consistent heating histories, the next step was to replicate work done by Manzello et al. [3] by placing the embers onto fuel beds under different conditions and observing whether the fuel bed ignites. The fuel beds tested were shredded paper and dried mulch placed in an aluminum foil pan. The dimensions of the fuel bed were 10 cm x 20 cm x 2.5 (3.9”x 7.9” x 1.0”) cm and six k-type, 24 gauge thermocouples were placed at a height of 1 cm (0.4”) from the bottom in the configuration seen in Figure 2.36. Infrared imaging was also used to track the resulting temperature evolutions in tandem with the thermocouple data.

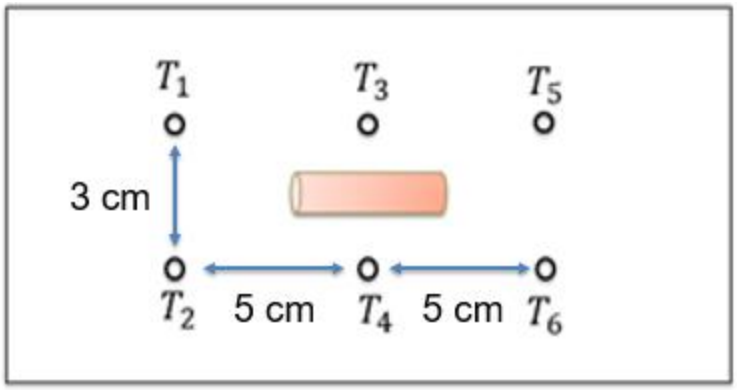

Figure 2.36: Schematic of thermocouple and ember orientation on shredded paper and dried mulch fuel bed

In order to produce an ember in a flaming state, the wooden dowel was left inside of the furnace at 500 °C and was pulled out once it was flaming. The four cases tested were a glowing ember dropped onto shredded paper or dry mulch, and a flaming ember dropped onto shredded paper or dry mulch. Recycled printer paper was processed through a shredder, while mulch made from native Texas hardwood was dried in an oven at 105 °C. The mulch was left in the oven until its weight remained unchanging by 0.5% between weighings every hour. The qualitative results can be seen to match the results produced by Manzello et al. as depicted in Figures 2.37 - 2.39 and Table 2.4, where the glowing ember caused smoldering of the paper and no ignition of the mulch, and the flaming embers caused both flaming ignitions.

Table 2.4: Comparison of ignition results with Manzello

State of Firebrand	Shredded Paper	Shredded Paper (Manzello)	Dry Mulch	Dry Mulch (Manzello)
Glowing	SI	SI	NI	NI
Flaming	FI	FI	FI	FI

NI = no ignition; SI = smoldering ignition; FI = flaming ignition

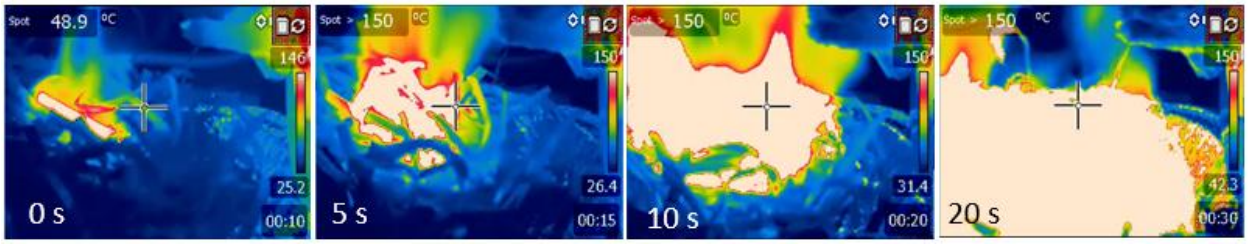

Figure 2.37: Flaming ignition on shredded paper after flaming ember dropped

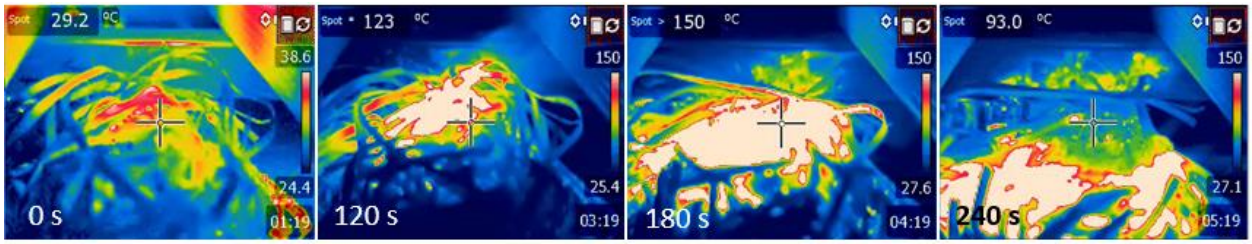

Figure 2.38: Smoldering ignition on shredded paper after glowing ember dropped

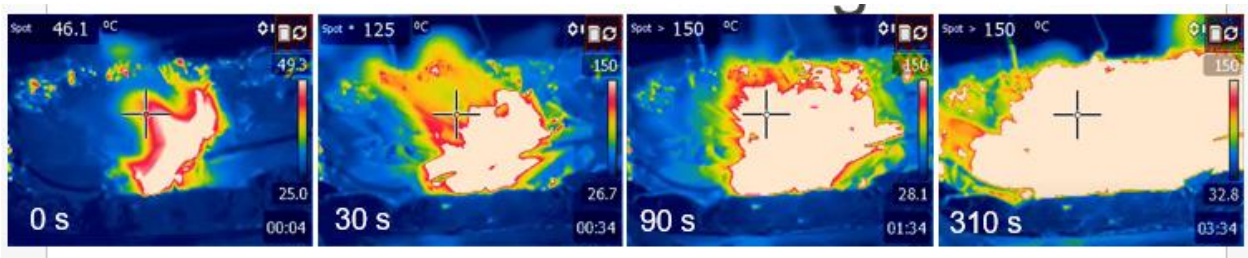

Figure 2.39: Flaming ignition on dry mulch after flaming ember dropped

The resulting fuel bed thermocouple data for flaming ignition on a shredded paper bed, as well as smoldering ignition on a shredded paper bed can be seen in Figures 2.40a

and 2.40b, respectively. The curves on the figures begin at the time when the ember is placed onto the fuel bed. The temperature profiles show that the flame spread rate is much faster and the temperatures are much hotter during flaming ignition, compared to that observed in smoldering ignition. It should be noted that thermocouples four and five malfunctioned during our tests, as they were not rated for high temperatures and had been exposed to flame previously. The data were dropped from the data set due to unrealistic measurements (e.g. a temperature range of -1000 °C to 10000 °C). The thermocouples were replaced with k-type, 24-gauge, high-temperature glass thermocouples during subsequent testing. Furthermore, the resulting fuel bed thermocouple data were compared to that obtained by Hadden et al. [8], who observed flaming ignition on α-cellulose beds after dropping a hot metal particle on it, followed by in-depth smoldering, Figure 2.41b. It was not noted when flaming ignition had stopped, nor when the in-depth smoldering began. Hadden et al's thermocouple configuration can be seen in Figure 2.41a. They also introduced house air at a velocity of 0.5 m/s. Even though the materials were similar, powdered cellulose vs. shredded cellulose, the time scale of their experiment was much longer than both our flaming ignition and smoldering ignition results. It is not known why this difference is so large.

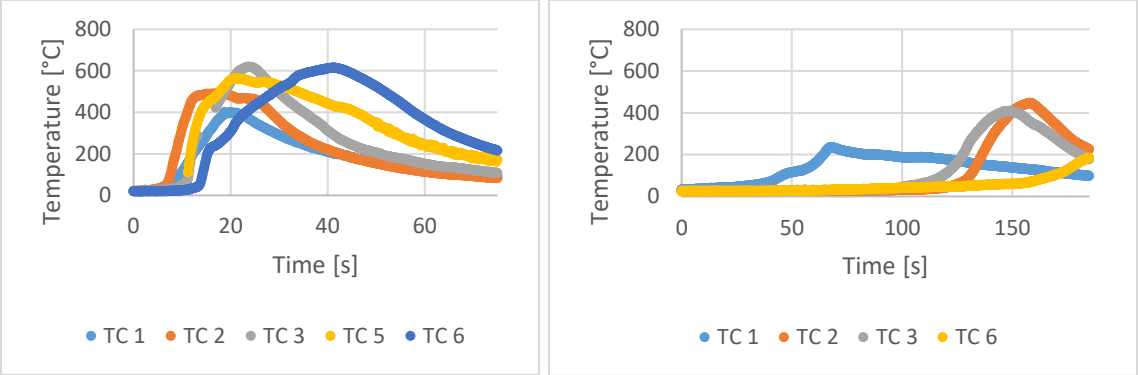

Figure 2.40: a) Temperature data from flaming ignition of the shredded paper bed
b) Temperature data from smoldering ignition of the shredded paper bed

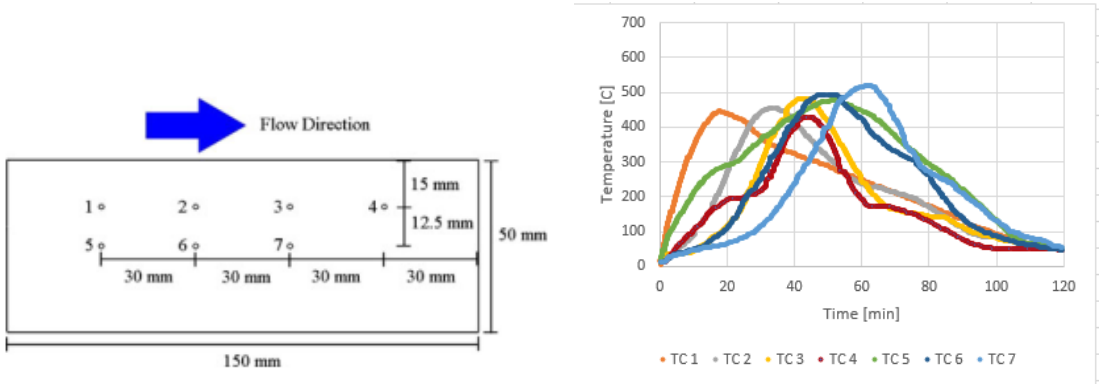

Figure 2.41: a) Thermocouple setup of Hadden et al. b) Temperature data from flaming ignition of powdered α-cellulose [8]

After these tests were performed, improvements were made to the setup to accommodate the controlled environment needed to test insulation ignition. The air flow chamber, initially a plastic container, was replaced with a Plexiglas box as detailed in section 2.2. Electrical noise was reduced by isolating electrical components using insulation, while air leakage in the air flow chamber was minimized using putty to seal any gaps. The procedure was also improved over time to obtain the following results.

2.3.3 Visual Descriptors of Ember Ignition Results

After the ember was dropped, one of four things would happen: extinction, smoldering ignition, flaming ignition, or flash flaming ignition. Due to the presence of flame retardants in the insulation, smoldering would only occur in the non-flame retarded cases. Flash flames can be characterized as wisps of fire that typically only last for a few seconds. Figure 2.42 shows an example of flash flames on PUR and XPS with a 4.8 m/s air flow condition. Because of the flame's short residence time, the fuel bed is not largely affected and is not consumed as is in the case of flaming ignition.

Figure 2.42: a) Flash flame on PUR with 4.8 m/s air flow condition by a large ember
b) Flash flame on XPS with 4.8 m/s air flow condition by fragmented embers

The polymeric insulation types showed flash flames, whereas the cellulosic insulation types were observed to have flaming ignition. An example of the progression of flash flaming can be seen with XPS at a 2.4 m/s air flow condition in Figure 2.43 by fragmented embers. After the embers came into contact with the XPS, the XPS immediately began to melt. Flash flames can be seen as the embers melt through the XPS at three seconds, and the flames continued for seven additional seconds. Once the flame

concluded, the heat radiating from the embers melted the XPS within a certain region and continued to char the wood substrate until the embers extinguished.

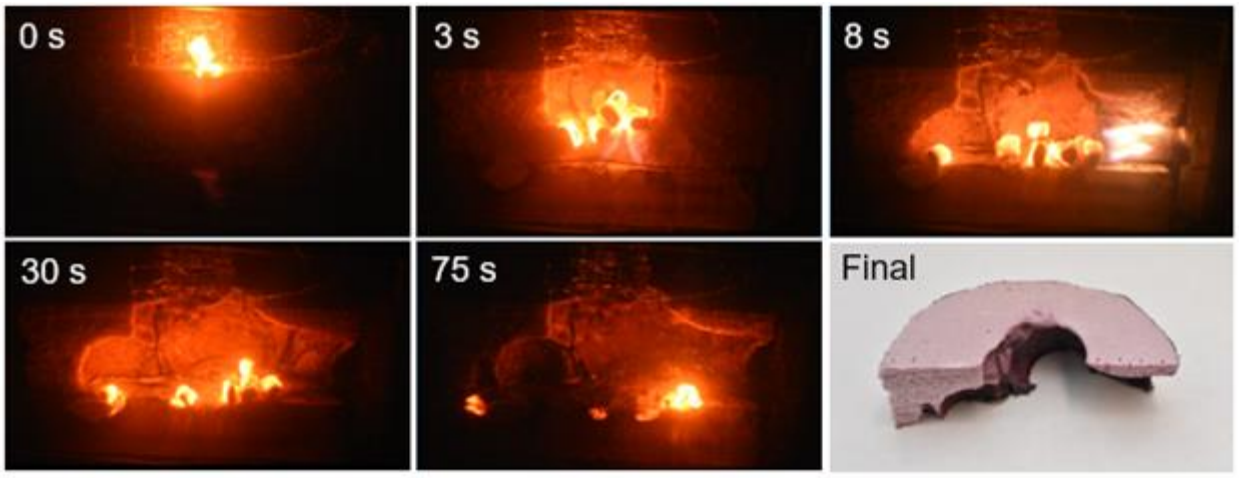

Figure 2.43: Flash flaming of XPS with 2.4 m/s air flow condition by fragmented embers

A similar trend can be seen in the case of EPS at a 4.8 m/s air flow condition by fragmented embers seen in Figure 2.44. In this case, the EPS immediately began to melt once contact was made with the embers. The EPS began to flash flame at three seconds, and endured until the embers exit out the back of the insulation at five seconds due to the air flow. This occurred due to the stagnation flow that occurs, which pushed the embers away from the stagnation point, guiding the embers out the back and sides of the insulation once the EPS has melted. The flash flame is difficult to see in the photos, but can be observed in the video due to the characteristic flickering from the flame in the background.

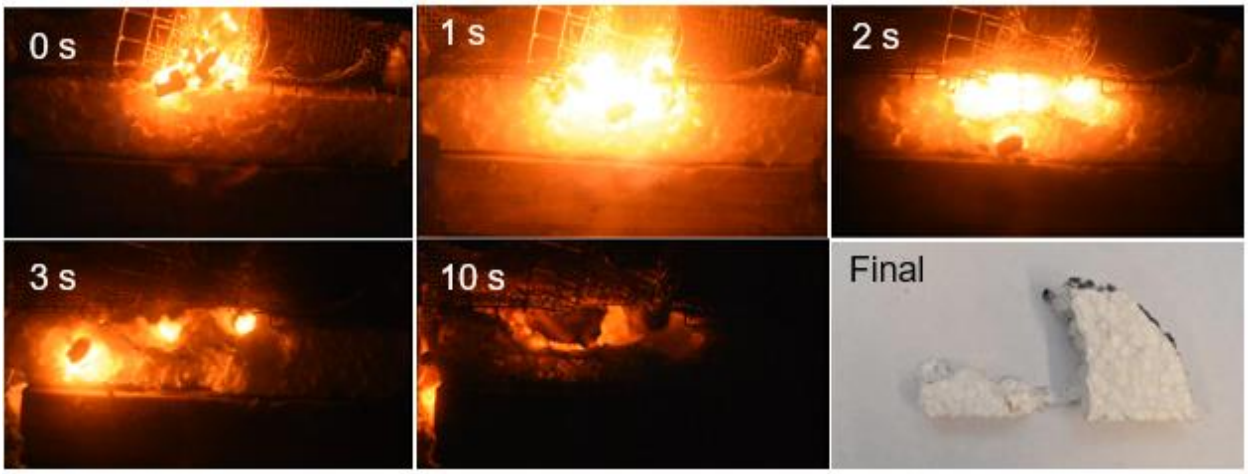

Figure 2.44: Flash flaming of EPS with 4.8 m/s air flow condition by fragmented embers

A close-up of the XPS after fragmented embers were dropped onto it at 0 m/s and 2.4 m/s can be seen in Figures 2.45 and 2.46. The resulting fuels can be seen to have an ember shaped hole in the top, and a cavern-like shape on the lower layer. For the EPS and XPS cases, the void volume created by the ember's melting of the material increased once air flow was introduced, as seen with the comparison between the two XPS cases. The increase in void volume most likely occurred due to a combination of the increased stagnation pressure that pushed the embers and an increase in ember heat generation that helped the ember melt through the fuel bed faster. The air flow would also sometimes cause the ember to spin, allowing the side of the ember in contact with the fuel bed to heat up through oxidation again before rotating and heating up the fuel bed again. A similar trend was noticed with the EPS.

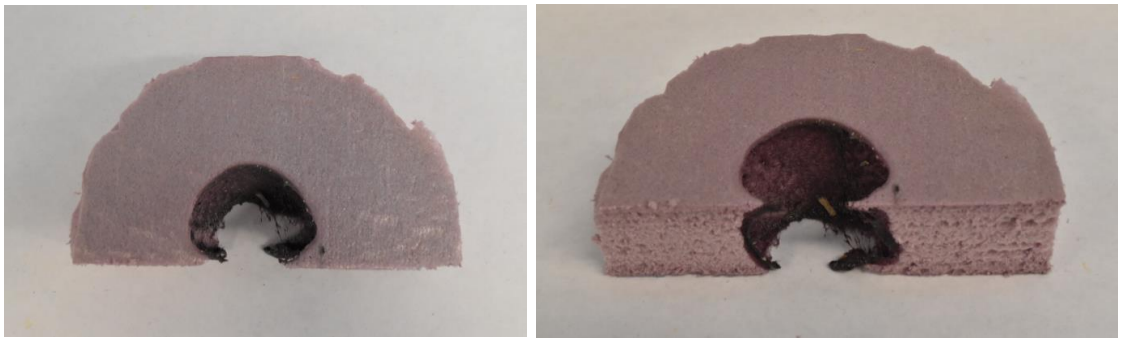

Figure 2.45: a) Top view of fragmented embers on XPS at 0 m/s air flow condition
b) Tilted view of fragmented embers on XPS at 0 m/s air flow condition

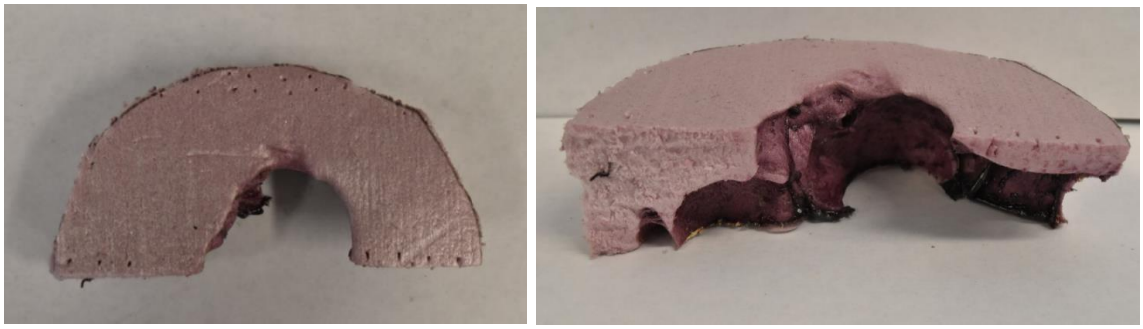

Figure 2.46: a) Top view of fragmented embers on XPS at 2.4 m/s air flow condition
b) Tilted view of fragmented embers on XPS at 2.4 m/s air flow condition

In the cases of EPS and XPS, the presence of flash flames was highly dependent on the location of the embers. If the embers were too far from the fuel, the embers could not provide enough heat to volatilize the fuel into a flammable mixture. Once the initial fuel had volatilized and the embers had burnt through to the wooden substrate, the embers were too distant to pilot an ignition as well.

Figure 2.47 shows an example of flash flames that occur on PUR at a 4.8 m/s flow condition by a large ember. The flash flames that occurred in the PUR foam at an air flow of 4.8 m/s started sixty seconds after the ember was dropped onto the fuel bed and

continued for fifteen seconds. After this time, the flame extinguished and the ember extinguished gradually as well. The flash flames occurred much faster for the EPS and XPS, compared to the PUR, due to their quicker volatilization.

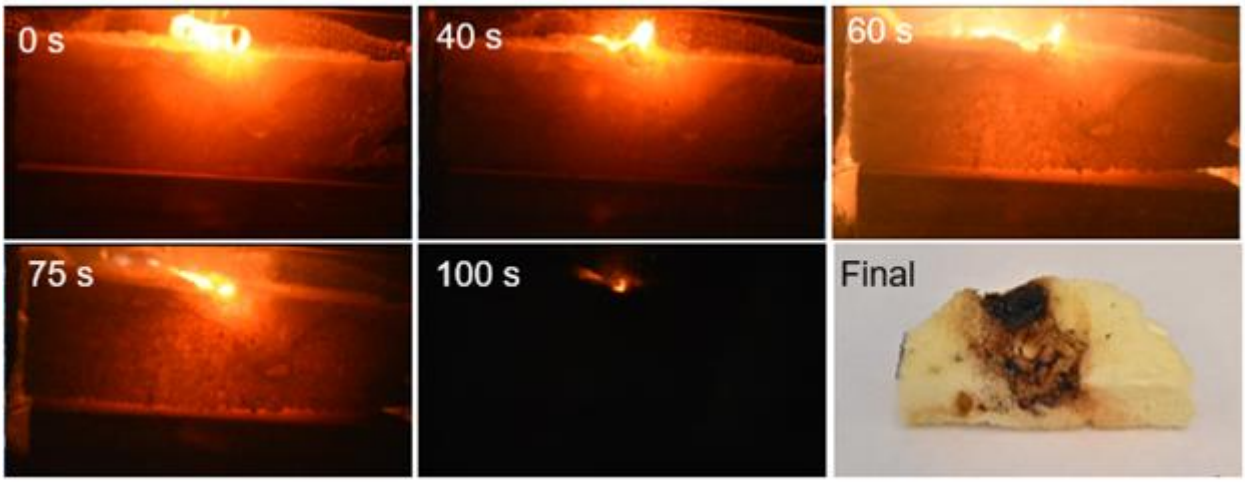

Figure 2.47: Flash flame of PUR foam with 4.8 m/s air flow condition by large ember

At low air velocities, the fuel bed absorbs the ember's energy until the ember is fully quenched. Minimal fuel degradation occurs, and thus, a combustible air/fuel mixture is not achieved. However, at higher velocities, the ember is able to oxidize at a higher rate, generating heat at a comparable rate to which it is losing heat to the fuel bed and surroundings. As the fuel bed temperature increases, the rate of pyrolysis and volatile production also continues to increase. Once the pyrolysis rate reaches the critical ignition rate, the volatile gas mixture will ignite, resulting in flaming ignition.

Figure 2.48 shows a typical case where flaming ignition of flame retardant (FR) denim at a 2.4 m/s air flow condition by fragmented embers was observed. Within the first five seconds of being dropped onto the denim, the fragmented embers began to volatilize

the fuel bed and smoke began to obscure the view. After twelve seconds, small flames began to appear which eventually enveloped the rest of the fuel bed. Prior tests involving flaming ignition of any of the fuel beds have shown that the entire fuel would be consumed. Therefore, the test was stopped prematurely in order to preserve the state of the chamber, due to possible damage due to the flames.

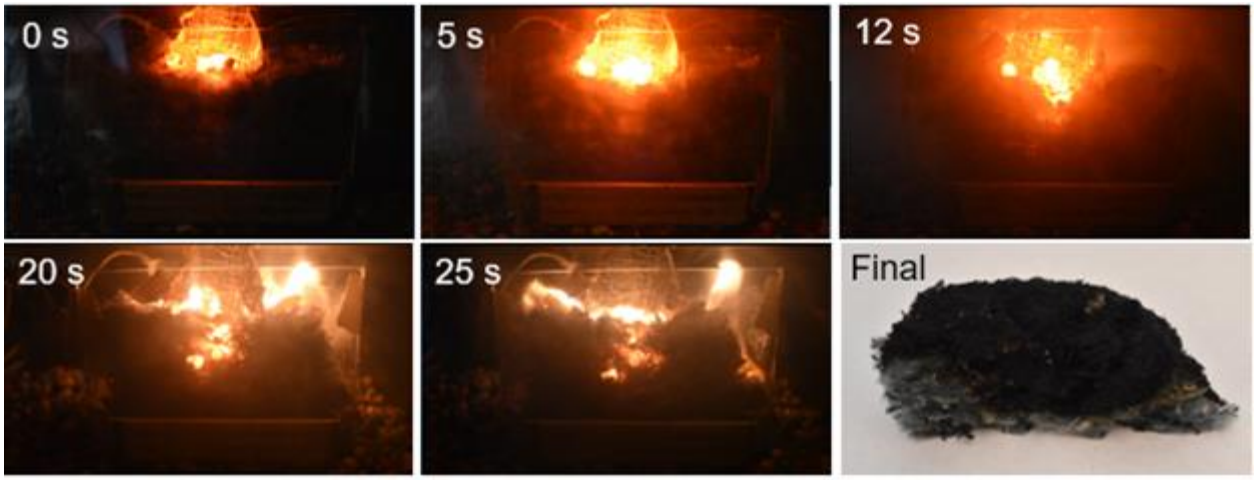

Figure 2.48: Flaming ignition of denim insulation with 2.4 m/s air flow condition by fragmented embers

Figure 2.49 shows an example of flaming ignition on FR-cellulose at a 4.8 m/s flow condition with a large ember. For this particular example, the ember began to sink into the cellulose as it degraded the initial layers of cellulose between the time of ember drop and 10 seconds. Around 13 seconds, the rate of pyrolysis increased as indicated by the increased observable smoke. Finally ignition occurred at 18 seconds, and consumed the fuel bed.

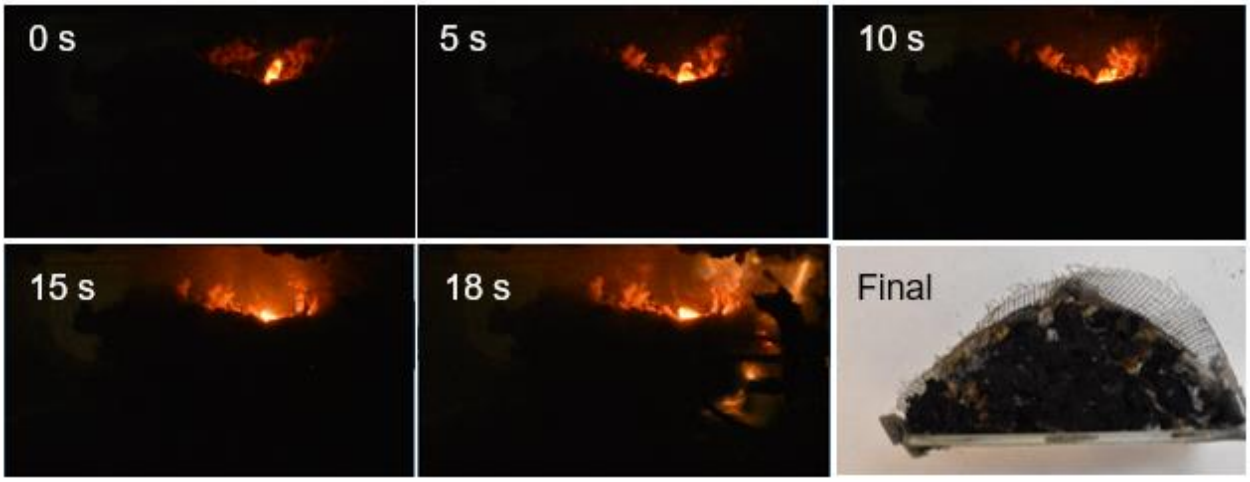

Figure 2.49: Flaming ignition of cellulose insulation with 4.8 m/s air flow condition by large ember

Table 2.5 shows the results of the ignition tests for the various flame retarded fuel bed materials at varying air flows and with the two ember geometries. Each condition was tested three times and behavior was observed to be consistent.

Table 2.5: Ignition results of various FR insulation cases

Material Type	Air Flow (m/s)	Frag. Ember Behavior	Large Ember Behavior
FR-Denim	0	NI	NI
	2.4	FI	FI
	4.8	FI	FI
FR-Cellulose	0	NI	NI
	2.4	FF	FF
	4.8	FI	FI
PUR	0	NI	NI
	2.4	NI	FF
	4.8	FF	FF
XPS	0	NI	NI
	2.4	FF	NI
	4.8	FF	FF
EPS	0	NI	NI
	2.4	FF	NI
	4.8	FF	FF

NI = no ignition; FF = flash flaming; FI = flaming ignition

The only FR-cases that resulted in flaming ignition were the FR-denim at a 2.4 m/s air flow condition, the FR-denim at a 4.8 m/s air flow condition, and the FR-cellulose at an 4.8 m/s air flow condition. Interestingly, both of the FR-cellulosic insulations ignited, while the FR-polymeric insulations merely flash flamed. Because the FR-cellulosic materials were the only samples to flame, samples of non-flame retarded (NFR) denim and non-flame retarded (NFR) cellulose were also tested at these conditions for comparison. Additional tests were performed for the cellulosic materials, so that both FR and NFR materials were tested for a total of five times. The material differences between these types of materials, as well as the differences between FR and NFR materials, would be a driving motivation to the material analysis performed later on.

The NFR-denim was initially shredded into fibers using a razor blade, as seen in Figure 2.50a. However, this did not have the same morphology as the FR-denim batting. An effort was made to turn the fibers into a more batting-like material, using two brushes, seen in Figure 2.51, to scrub the fibers until the material looked like Figure 2.50b, which resembles the FR-denim batting more closely.

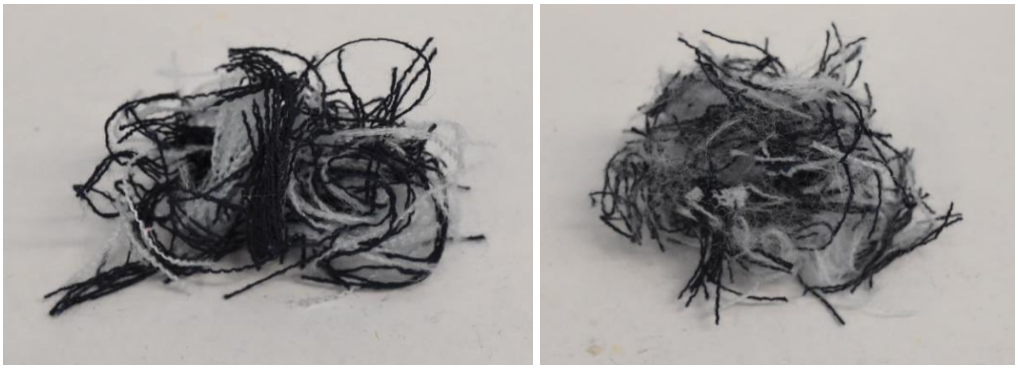

Figure 2.50: a) NFR-denim fibers before scrubbing b) NFR-denim fibers after scrubbing

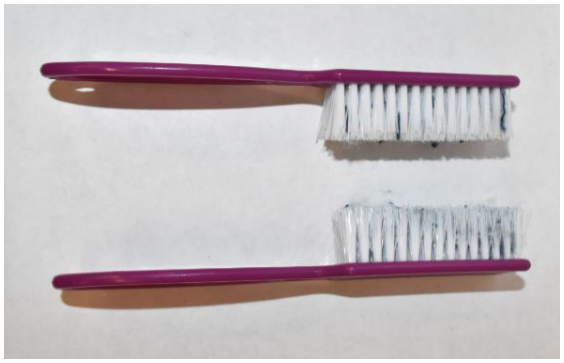

Figure 2.51: Brushes used to scrub NFR-denim fibers

Before and after comparisons of the fuel beds from fragmented embers and large embers can be seen in Figure 2.52 and 2.53, respectively. The cases of flaming ignition all look similar and typically will become fully consumed if the tests are allowed to continue.

The 0 m/s air flow conditions were not tested for the NFR-denim and NFR-cellulose as these air flow conditions did not cause flaming on their FR counterparts. More effort was placed on the higher velocity cases to better allow for comparisons between the FR and NFR insulations. The photo for the 0 m/s air flow condition for the EPS for large embers was not taken, and is therefore not available at the time.

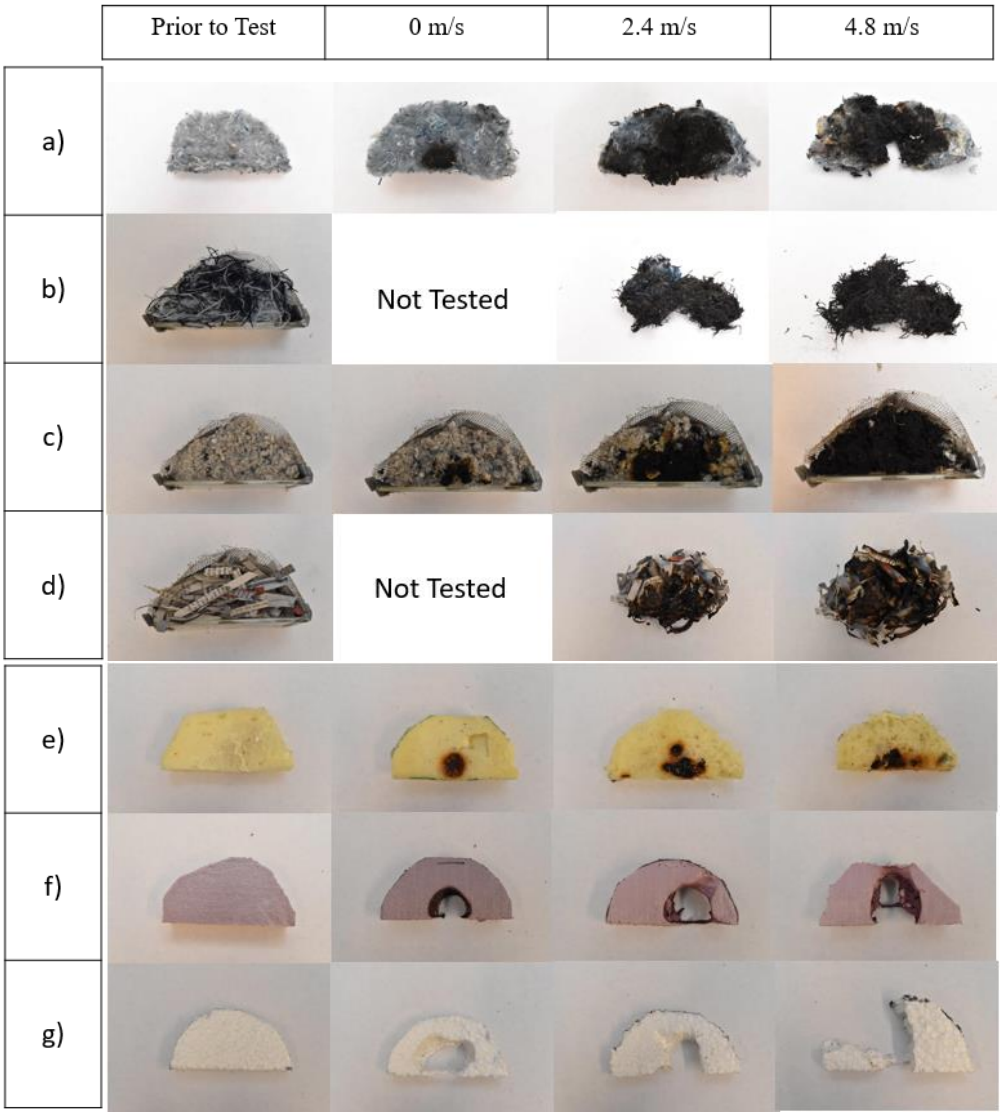

Figure 2.52: Fragmented ember tests at 0 m/s, 2.2.4 m/s and 4.4.8 m/s air flow conditions for a) FR-Denim b) NFR-Denim c) FR-Cellulose d) NFR-Cellulose e) PUR f) XPS g) EPS

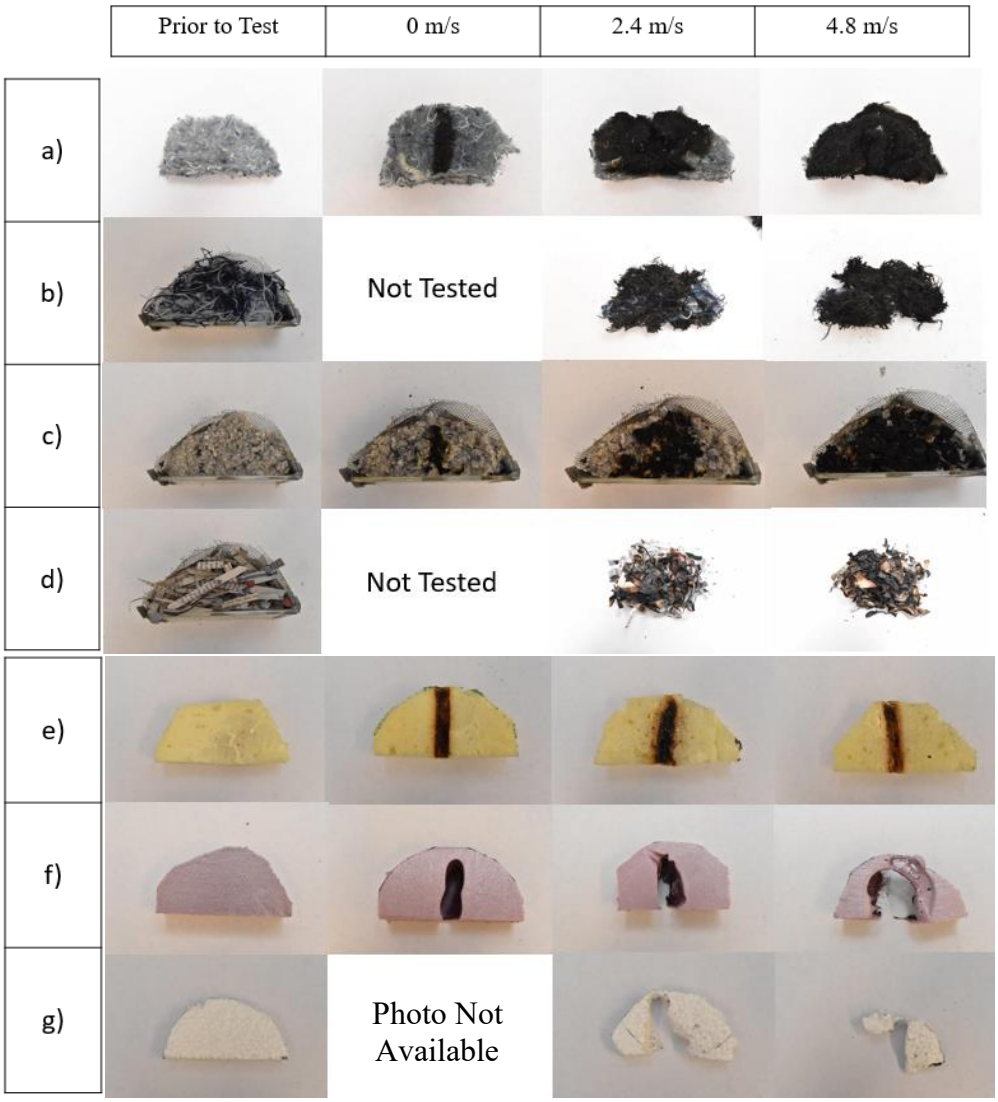

Figure 2.53: Large ember tests at 0 m/s, 2.2.4 m/s and 4.4.8 m/s air flow conditions for a) FR-Denim b) NFR-Denim c) FR-Cellulose d) NFR-Cellulose e) PUR f) XPS g) EPS

The char area is larger on the larger ember tests, while the char depth was deeper on the fragmented ember cases. This effect can be seen in Figures 2.54-2.55 for the case of PUR at a 2.4 m/s air flow condition. Furthermore, the effects of the thermal penetration, and possibly the flash flaming, can be seen in the discoloration of the PUR between the

ember drop location and the area surrounding it. The areas of discoloration show the parts of the material that had begun to pyrolyze during the experiment.

Figure 2.54: Char depth on PUR with 2.4 m/s air flow condition - a) Large ember
b) Fragmented embers

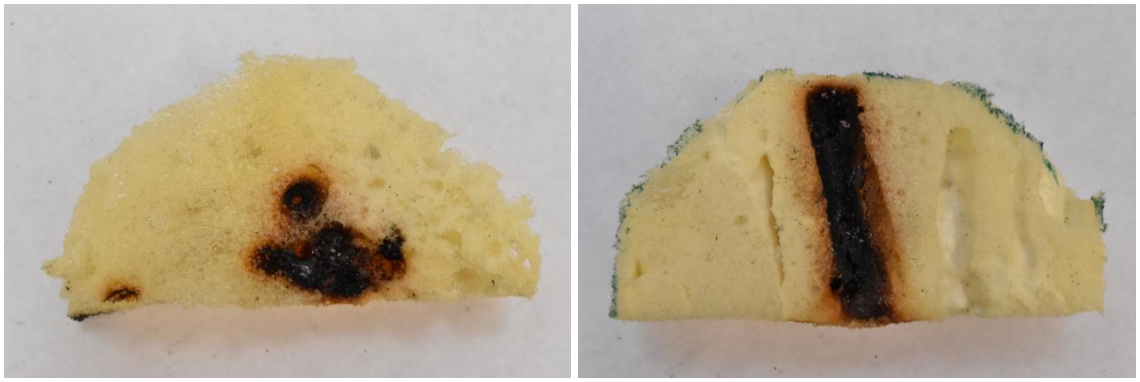

Figure 2.55: Char area on PUR with 2.4 m/s air flow condition - a) Large ember
b) Fragmented embers

A comparison of the flaming ignition times of these tests for the fragmented embers and large embers can be seen in Figure 2.56 and 2.57 and are summarized in Tables 2.6 and 2.7, respectively. Only materials at air flow conditions that caused flaming ignition were tested, which is why FR-cellulose at an air flow condition of 2.4 m/s was not included in the results. As expected, the times to ignition of the NFR samples were lower than those

of its flame retarded counterparts. Boric acid was the main flame retardant in these samples, and therefore contributed to reductions in char oxidation, as well as inhibiting ignition in the vapor phase through dilution [15]. Increasing the air flow also quickened ignition due to the higher oxidation rate of the ember, leading to higher ember temperatures, thus increasing the pyrolysis rate of the fuel beds. An increased air flow also contributes to shortening the mixing time of the volatile mixture. There may be a flow rate that has a high enough convection cooling rate that would offset the heat gained through oxidation, but that critical flow rate was not found during these tests.

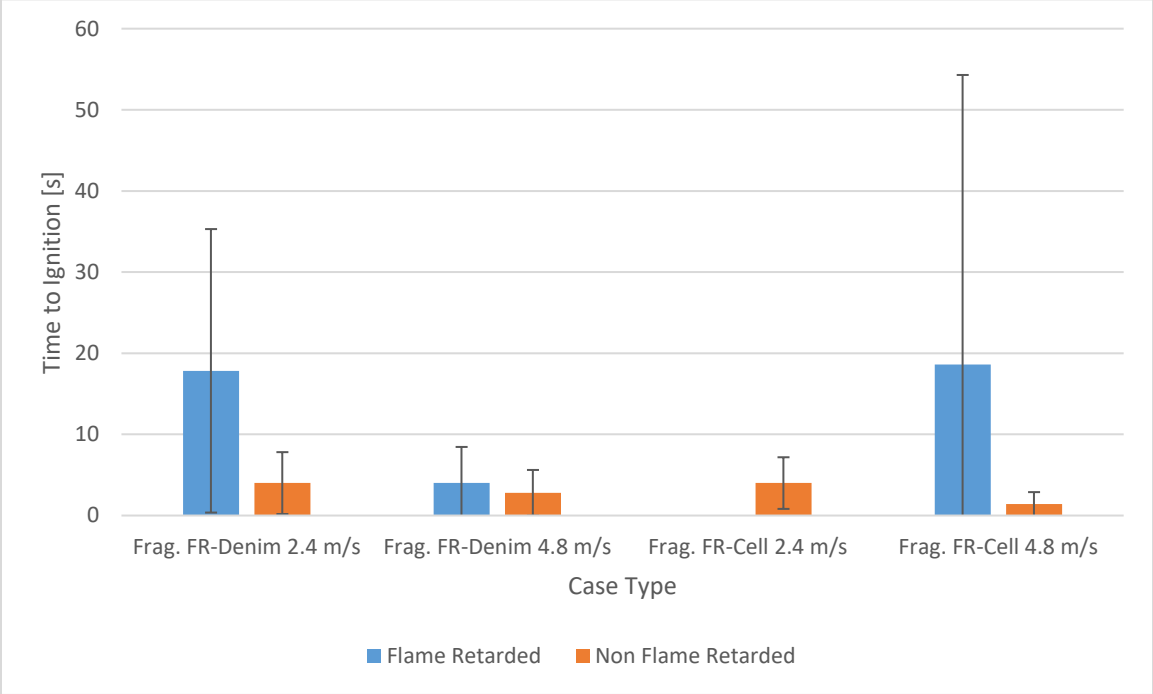

Figure 2.56: Ignition times of NFR vs. FR materials by fragmented embers

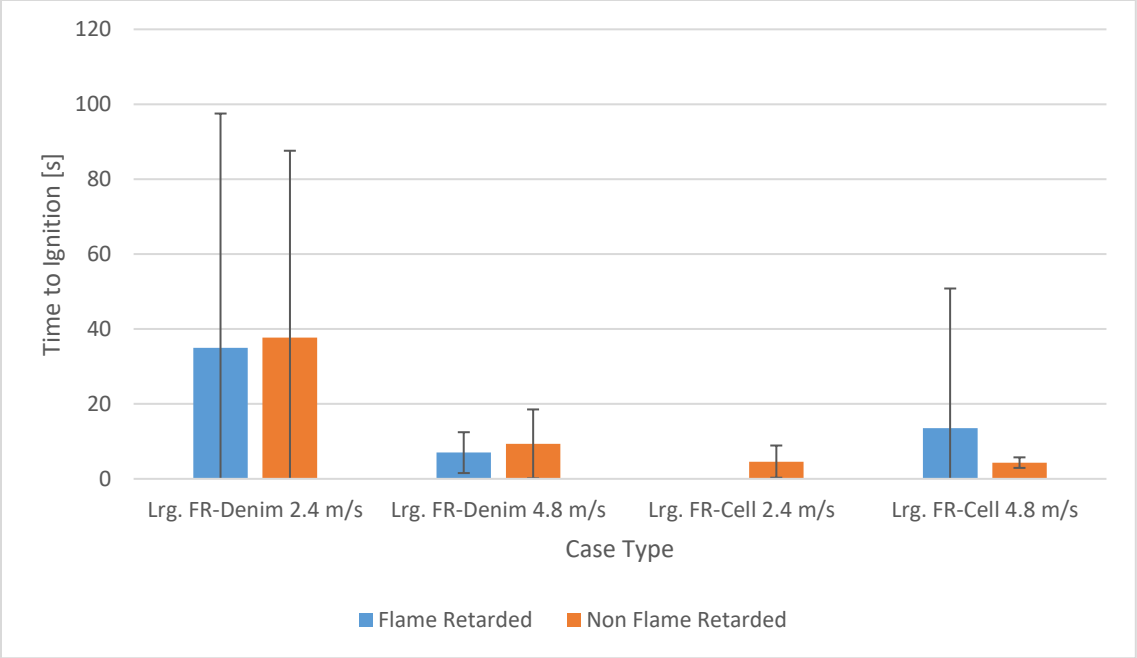

Figure 2.57: Ignition times of NFR vs. FR materials by large embers

Table 2.6: Times to Ignition (TTI) of the fragmented embers

Material	Wind Speed [m/s]	TTI #1	TTI #2	TTI #3	TTI #4	TTI #5	TTI #6 *
FR-Denim	2.4	15	21	14	12	31	14
FR-Denim	4.8	6	3	3	3	5	-
NFR-Denim	2.4	5	7	3	5	4	-
NFR-Denim	4.8	3	3	3	1	4	-
FR-Cellulose	4.8	7	11	11	41	23	-
NFR-Cellulose	2.4	3	5	4	-	-	-
NFR-Cellulose	4.8	1	2	1	2	1	-

Table 2.7: Times to Ignition (TTI) of the large embers

Material	Wind Speed [m/s]	TTI #1	TTI #2	TTI #3	TTI #4	TTI #5
FR-Denim	2.4	27	43	73	22	10
FR-Denim	4.8	10	7	5	8	5
NFR-Denim	2.4	48	20	45	4	14
NFR-Denim	4.8	8	14	6	14	5
FR-Cellulose	4.8	11	16	18	48	23
NFR-Cellulose	2.4	3	3	7	5	5
NFR-Cellulose	4.8	1	1	2	2	1

The pile of fragmented embers had quicker ignition times compared to the larger embers. Although the fragmented ember pile was measured to have about 25% less surface area in contact with the fuel substrate, it does have more surface area exposed to air due to its porosity and can thus oxidize at a faster rate. It is this effect paired with the compact geometry of the pile that allows the heat lost by the embers on the bottom to be fueled by the embers on the top, which ultimately leads to the higher fuel pyrolysis rate and the faster ignition times. The ignition effects of differently shaped embers align well with the results from Manzello et al. [3], where they had previously found that the contact surface area between the ember and the fuel bed, as well as ember shape was important to ignition. A smaller amount of fragmented ember mass would most likely ignite a fuel bed under the same conditions as a higher mass large ember. Furthermore, it can be assumed that piled fragmented embers pose a larger threat than the disk-shaped embers used by Manzello et al., since their cylindrical embers were more prone to ignite fuel beds compared to their disk-shaped embers.

The scatter represented in the data was represented by the uncertainty calculated using the Student's t-distribution for a 95% confidence interval, and can be seen by the error bars on Figure 2.56 and 2.57. It should be noted that this is not the error, but it represents the variability in the limited number of tests that were able to be performed. This scatter associated with the ignition times ranged from 2 seconds to 36 seconds for the fragmented embers and 2 seconds to 63 seconds for the large embers. Care was taken to ensure consistency of embers, air flow, and placement; however, there were sources of uncertainty in the fuel bed characteristics, such as flame retardant loading and moisture content, as well as in the placement and dropping configurations of the embers. Furthermore, we were only able to run a limited number of cases, which led to a larger variability.

It should be noted that there is a considerable amount of scatter for the large ember FR/NFR denim cases at 2.4 m/s, the large/fragmented ember cellulose case at 4.8 m/s, and the fragmented ember case for FR-denim at 2.4 m/s. The "more flammable cases", such as those with higher air flow conditions and the NFR materials, seem to show less scatter. The source of scatter needs to be further investigated, but a likely cause of the higher scatter for the aforementioned cases is that the heat flux produced by the ember is near the critical heat flux for ignition of the materials. This results in a parameter space where the time to ignition is much more sensitive to the given conditions, thus resulting in a high sensitivity to variability in the conditions. This is most likely why the scatter goes down for higher heat fluxes as well. Because the FR-cellulose requires a higher heat flux, the higher error occurs at a higher air flow compared to the FR-denim. A similar trend can be seen by Zak

[9], Figure 2.58, where the probability of ignition of a 9.5 mm (0.4”) steel sphere on alpha-cellulose, drops from 95% to 5%, simply by dropping the temperature of the sphere from 670 °C to 610 °C. The scatter associated with the FR-cellulose at 4.8 m/s may also be due to the outlier of 48 seconds, which would eventually be washed out with enough repeated testing. Ideally, a larger number of samples would have been taken in order to reduce scatter.

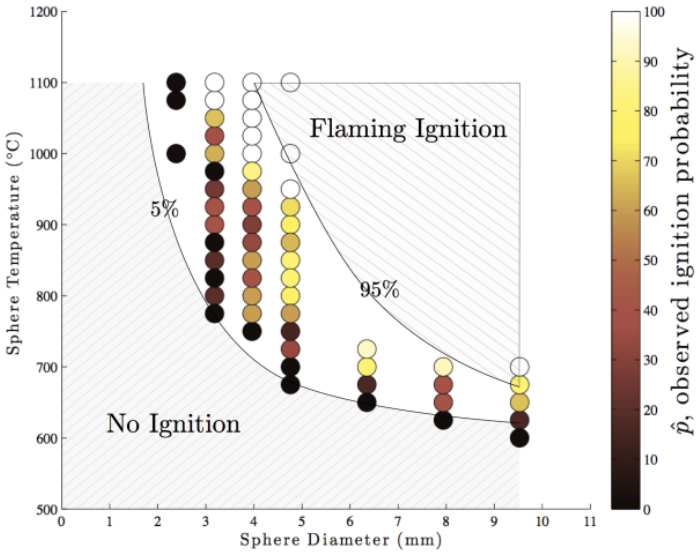

Figure 2.58: Observed ignition probability for stainless steel spheres dropped on alpha-cellulose [9]

2.3.4 Signatures of Ignition

The key signatures of ignition observed in the test cases were heavy smoke production, a sharp increase in the fuel-bed temperature, or a bright glowing ember indicating elevated temperatures. Examples of fuel-bed temperature, measured by the thermocouples, and maximum ember temperature, determined from the IR measurements, can be seen in Figures 2.59 and 2.60 for the cases of flaming ignition on NFR-denim and

FR-denim, respectively, where ignition occurs at the dashed red line. The graphs start at the time of ember drop, and end after the air flow is turned off.

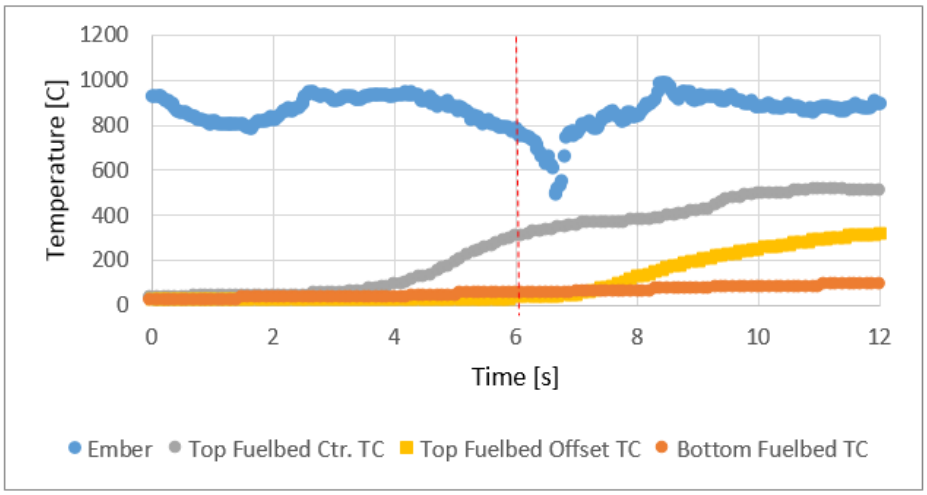

Figure 2.59: Large ember flaming ignition on NFR-Denim (4.8 m/s) at 6 seconds

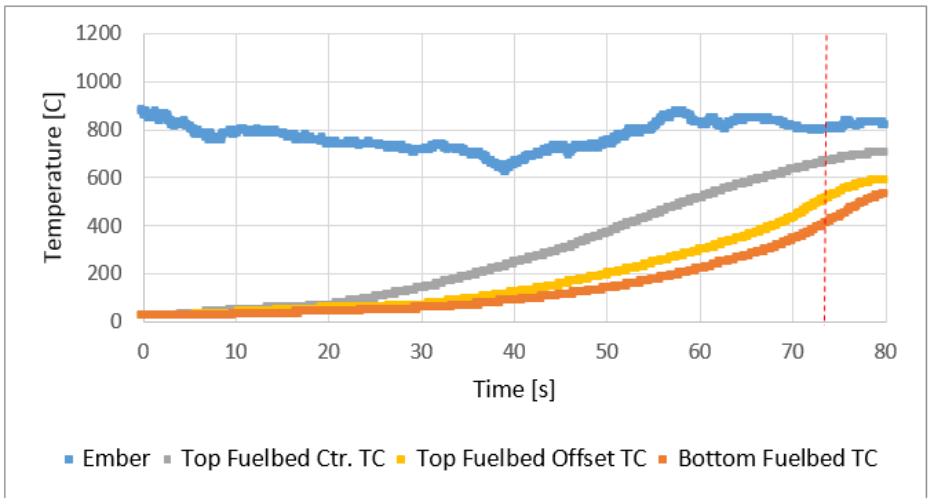

Figure 2.60: Large ember flaming ignition on FR-denim (2.4 m/s) at 5 seconds

Since the thermocouples are offset from the ember, there is a lag of a few seconds between the time of ember drop and when the thermocouples register the increase in temperature. During both ignition events observed, the center-top thermocouple

temperature, which was nearest to the ember, increases rapidly. The ember temperature shows fluctuations throughout the test because the ember was not always in clear view of the IR camera. At times, the ember would burn through the top layers of fabric and the IR camera would have a partially obstructed view. The portions that were visible to the camera weren't always in the area of focus, and thus the ember temperature would sometimes be averaged due to the pixel blur. During the tests in Figures 2.59 and 2.60, this effect is not too drastic, but one can notice the dip in Figure 2.59 around 6.5 seconds. It should also be noted that the IR temperature reported in the graph is the maximum observed temperature, and thus does not show the average temperature of the ember, nor does it tell us the temperature gradients observed throughout the ember. This maximum temperature appears to be roughly the same between the two tests on average though.

The extinguishing case of FR-denim at an air flow condition of 1 m/s can be seen in Figure 2.61. This case was a preliminary experiment, where the air flow conditions were still being investigated. The fuel bed initially heats up, but does not increase in temperature much higher than its initial temperature jump. The temperature of the fuel bed stays constant for about five additional minutes, due to the heat stored in the ember, as well as the insulating properties of the fuel bed. Once the ember is extinguished, the fuel bed follows the behavior of a convectively cooling body.

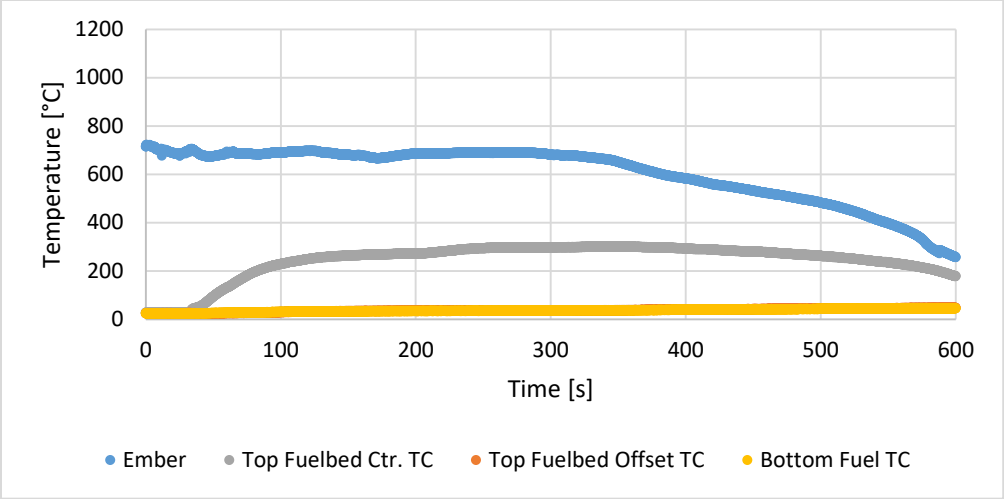

Figure 2.61: Ember extinction and fuel bed temperature response of FR-denim at 1 m/s air flow condition

The fuel beds appeared to show signs of ignition once any of the thermocouples reached a temperature of about 300 °C, where the thermocouple closest to the ember was most likely to reach this criterion first. Unfortunately, the XPS and EPS were difficult to instrument with thermocouples as the material melted quickly away from the ember, causing the thermocouples to be exposed and to no longer be measuring the material temperature. These restrictions further motivated the need to understand the thermal and flammability characteristics of our materials in a meaningful way. One additional set of tests were performed that attempted to find a relation between ignition and orientation of the fuel bed. This can be found in Appendix D.

2.4: Model of Ember in a Radiative Environment

2.4.1: Heat Flux from an Ember

The heat flux from the ember to the substrate was sought after, in order to help correlate results between the ember and the material degradation results. A first step was made to find the heat flux of the ember to the air. Although this does not represent the transient response of the ember's heat flux to the fuel bed, it can tell us the initial instantaneous heat flux once contact is made between the fuel bed and ember. This process followed the method used by Manzello et al. [4] where q''_{ember} is the heat flux of a glowing ember, h is the convective heat transfer coefficient, T_{surf} is the surface temperature of the ember, T_{amb} is the ambient temperature at 25 °C, ε is the emissivity of the ember, σ is the Stefan-Boltzmann constant, k is the thermal conductivity of the air, D is the diameter of the ember, Nu is the Nusselt number using the correlation between a cylinder with cross flow, Pr is the Prandtl number, and Re is the Reynold's number.

$$q''_{ember} = h(T_{surf} - T_{amb}) + \varepsilon\sigma({T_{surf}}^4 - {T_{amb}}^4) \tag{2.18}$$

$$h = Nu\frac{k}{D} \tag{2.19}$$

$$Nu = 0.3 + \frac{0.62Re^{\frac{1}{2}}\mathrm{Pr}^{\frac{1}{3}}}{\left[1+\left(\frac{0.4}{Pr}\right)^{\frac{2}{3}}\right]^{\frac{1}{4}}} * \left[1 + \left(\frac{Re}{282000}\right)^{\frac{5}{8}}\right]^{\frac{4}{5}} \quad \text{[4]} \tag{2.20}$$

An IR camera was used to find the surface temperature of the ember, and two different emissivities, 0.8 and 1.0, were used for the two wind speeds as seen in Figures 2.62. Figures 2.63 and 2.64 show the steady IR temperature measurement of an ember in a 2.4 m/s air flow condition and an 4.8 m/s air flow condition, respectively. Initial IR measurements were much higher than Manzello et al.'s results [4], which had average temperatures around 700 °C, so an internal thermocouple was inserted into the ember. From these results, it can be seen that the emissivity of a glowing ember is likely closer to 1.0 than 0.8 as previously determined for non-glowing embers. There is still a temperature gradient between the center of the ember and the surface, thus the higher surface temperature reading. However, the extent of this gradient is unknown, and should be explored further to find a more accurate emissivity value.

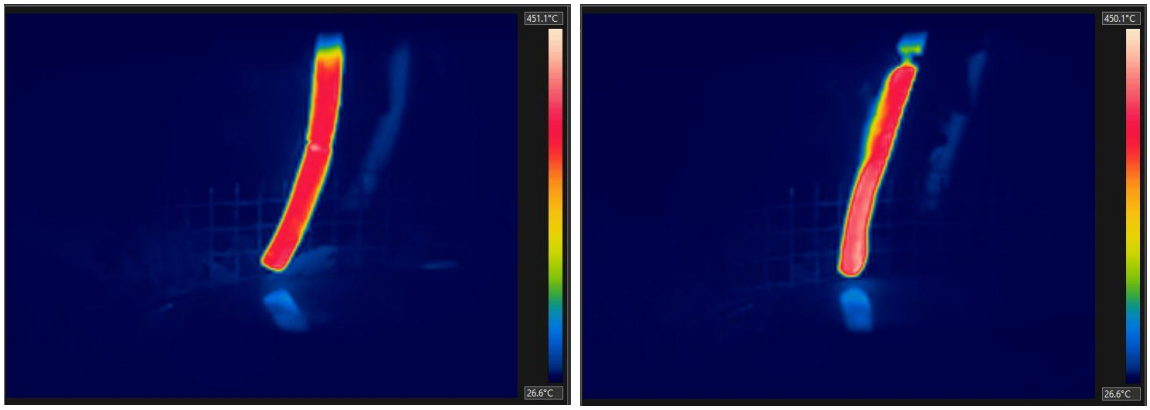

Figure 2.62: IR images of embers in wind speeds of 2.4 m/s (left) and 4.8 m/s (right)

[Temperature range denoted by color bar: 25 °C - 450 °C]

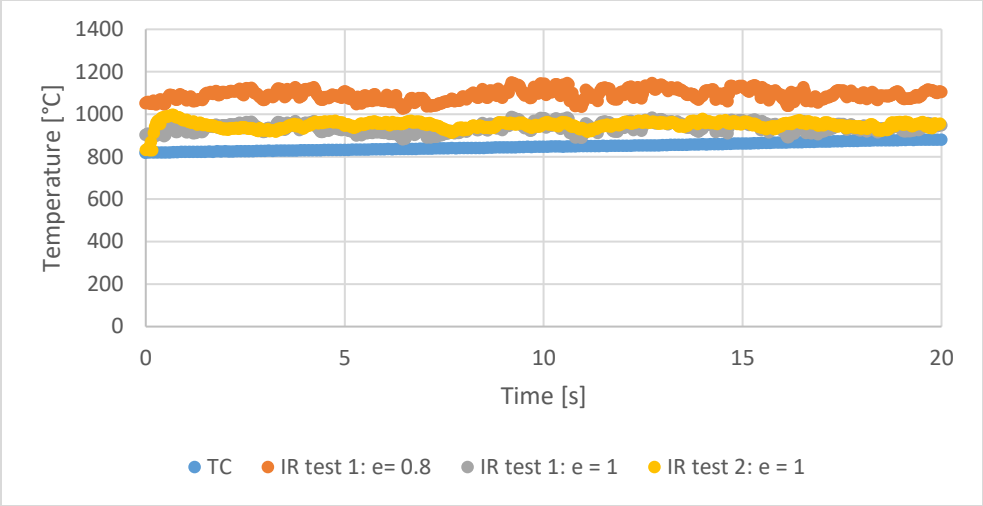

Figure 2.63: Temperatures of ember subjected to wind speeds of 2.4 m/s

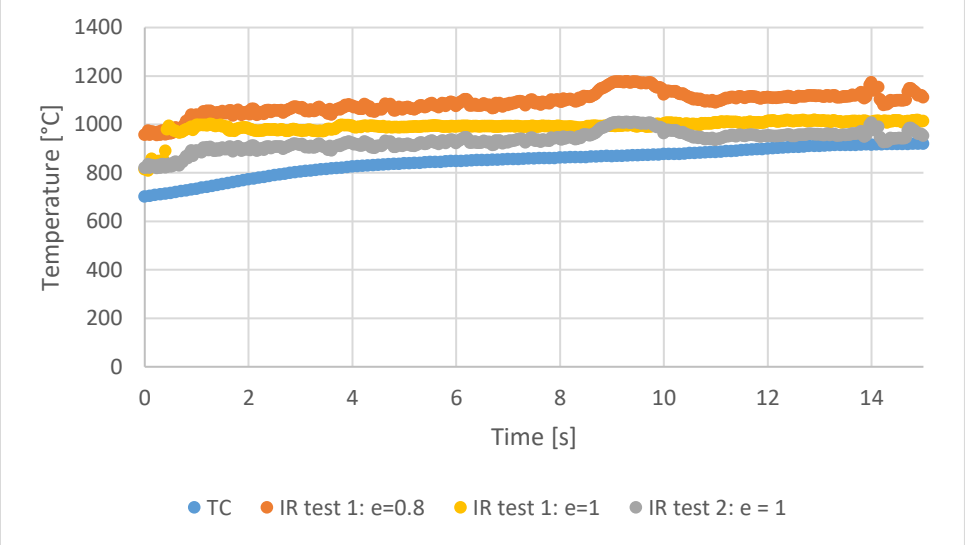

Figure 2.64: Temperatures of ember subjected to wind speeds of 4.8 m/s

An average surface temperature for an ember at the 2.4 m/s air flow condition was 942 °C, whereas the average surface temperature for the 4.8 m/s condition was 977 °C. The calculated instantaneous heat fluxes were 86.7 kW/m^2 for the 2.4 m/s case and 112.7

kW/m^2 for the 4.8 m/s case. It should be noted that the heat flux between the ember and the fuel bed will drop almost immediately as the fuel bed quenches the ember surface. However, it is likely that the ember surface not in contact with the fuel bed will still maintain an elevated temperature, and have more than enough energy to heat up and pilot the ignition of the pyrolyzates.

The drying process of an ember in a radiative environment was also modeled using FEniCS, a partial differential equation solver platform. This model and results can be found in Appendices E and F.

Chapter 3 Material Property Investigation

3.1 THERMAL PROPERTIES

In order to better characterize the heat transfer and ignition processes of the insulation materials, it was necessary to find appropriate thermal properties. The process to find density is relatively straightforward, while specific heat requires more sophisticated experimental setups. Additionally, literature values of thermal conductivity for insulations vary from source to source and typical uncertainties in these measurements can be anywhere from 10 -20% [16]. Therefore, techniques were developed to obtain these three thermal properties. Although the thermal properties were not obtained for the insulations used in the ignition studies, the properties of acrylic were found to test these methods.

3.1.1 Experimental Setup

The densities of the insulations were measured by first coating the material in a hydrophobic coating, and then using the technique of water displacement to find the volume, as seen in Figure 3.1. The hydrophobic coating was prepared using a mixture of hydrophobic fumed silica (Aerosil R 812 S) and kerosene as a solvent, in a concentration of 9:1. Since acrylic was a solid, and the volume could be easily calculated, FR-denim was used to test this method on fabrics. The FR-denim was submerged in the mixture for one minute, and was then dried for a day, or until the weight remained unchanging after subsequent hourly weighings. The fabric was found to be hydrophobic by noting that the weight before and after being submerged in water remained unchanged. A weighted mesh

with a known volume was used to prevent the insulation from floating above the surface, to ensure a more accurate measurement. The FR-denim's density was found to be 41 kg/m^3, while the density using the volume and weight of the packaged denim was calculated to be 48 kg/m^3. This discrepancy can be due to the use of a small piece of material that was used, the large resolution of the beaker, or an incorrectly specified length, width, and weight on the denim's package. Larger samples of materials should be used in the future, with a beaker with a better resolution.

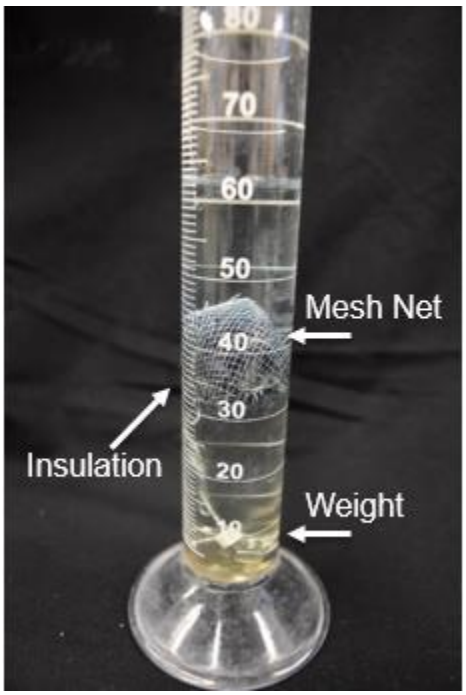

Figure 3.1: Density measurement setup

The specific heat can be found using differential scanning calorimetry if a reference curve, typically using a special sapphire crystal, is obtained. However, this was not possible to obtain, so values obtained from literature were used. The density of acrylic that was used was 1170 kg/m^3 and the specific heat used was 1470 J/(kg*K). Finally, the thermal

conductivity was found using the dual-hot plate setup in Figure 3.2. The acrylic block with dimensions of 104 mm x 104 mm x 12 mm (4.1” x 4.1” x 0.5”) was fitted with a centered thermocouple inserted from the side and was placed in between two isothermal hot-plates at the same temperature. The material of interest was further wrapped by Owens Corning Ecotouch insulation which had better insulating properties, with a thermal conductivity of 0.29 [17]. From there, the temperature evolution in the center of the material was recorded.

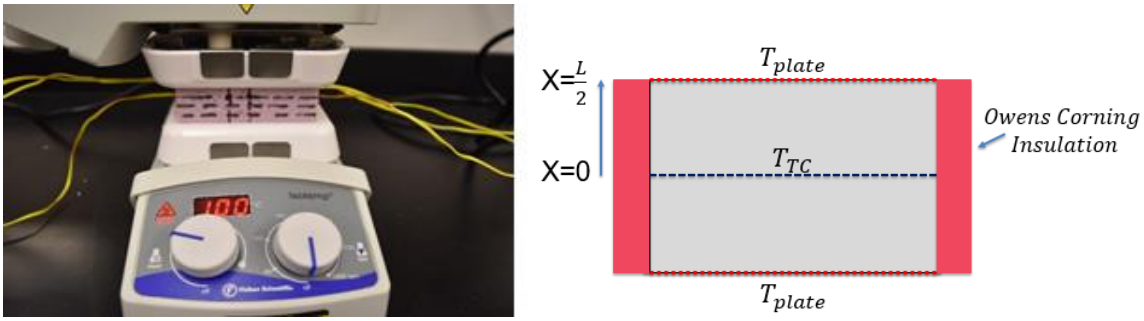

Figure 3.2: a) Thermal conductivity measurement setup b) Schematic of boundary conditions applied to insulation

An alternative setup was also created to compare the thermal conductivity measured with the first apparatus, as seen in Figure 3.3. The setup had two aluminum plates machined to fit heat flux gauges, Vatell Corporation BF02 heat flux sensors, in the center region. The material of interest would then be sandwiched between these two heat flux gauge plates, while placed on a hot plate. A heat sink was placed on the top of the heat flux gauge plates, while being cooled by a fan, in order to induce a constant heat transfer coefficient. Heat losses due to contact resistances between the heat flux gauge and the aluminum plate were apparent, so care was taken to mill the plate so that the gauges were perfectly flush.

Furthermore, a weight was placed on top of the setup to reduce any contact resistances between the materials and the heat flux gauges.

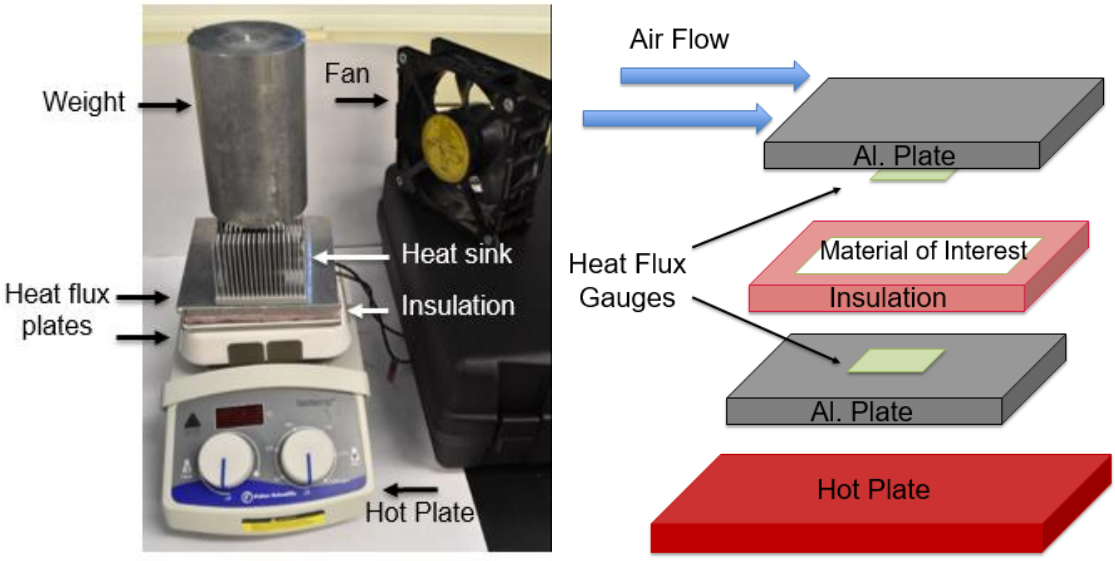

Figure 3.3: Alternative setup for finding thermal conductivity a) Image b) Schematic

The heat flux gauges could also measure temperatures, and so the temperature difference across the substrate could be measured. A thermocouple in the center of the material of interest was also used. The material was wrapped with material with higher insulating properties, Owens Corning Ecotouch Insulation, in order to promote 1-D heat transfer, and the heat losses were tracked by comparing the heat flux from the bottom plate to the heat flux from the top plate. Because the steady-state heat flux, steady-state temperature difference, and thickness were all known, thermal conductivity could be found using Eq. 3.1.

$$q'' = k\frac{\Delta T}{L} \tag{3.1}$$

3.1.2 Thermal Conductivity Solution

3.1.2.1 Bayesian Inversion

Once the transient temperature response was recorded from the first setup, the thermal conductivity was found using a Bayesian inversion performed in Python (PyMC), found in Appendix G. This method requires a theoretical model, a likelihood distribution of the random variables, and measurement data. The temperature in the material was modeled by the heat equation, Eq. 3.2, assuming an isothermal boundary condition, Eq. 3.3, and the symmetry boundary condition, Eq. 3.4. Thermal conductivity was thus found using the estimates of ρ, c_p, and the temperature response over time at a known location.

$$\rho c_p \frac{\partial T}{\partial t} = \mathrm{k} \frac{\partial^2 T}{\partial X^2} \tag{3.2}$$

Boundary Conditions:

$$T_{x=\left(\frac{L}{2}\right)} = 100 \tag{3.3}$$

$$\left(\frac{\partial T}{\partial X}\right)_{x=0} = 0 \tag{3.4}$$

Within the Bayesian inversion code, the differential equation was solved using the Crank-Nicolson method, a typical scheme used to solve the heat equation. The solution was validated against MATLAB's partial differential equation solver. From there, the thermal conductivity was treated as having a uniform distribution within the range of interest, while the model was fitted using a Markov chain Monte Carlo algorithm.

Acrylic was used as a test for the method. The dimensions of the acrylic sample were machined such that the length and width were much greater than the height, in order to minimize lateral heat losses. The predicted temperature response in the center of the acrylic can be shown against the actual response in Figure 3.4a, while the results of the inversion simulation can be seen in Figure 3.4b. The simulation estimated a thermal conductivity value of 0.19 W/(m*K), which is comparable to previously found values of 0.17-0.19 W/(m*K) [18].

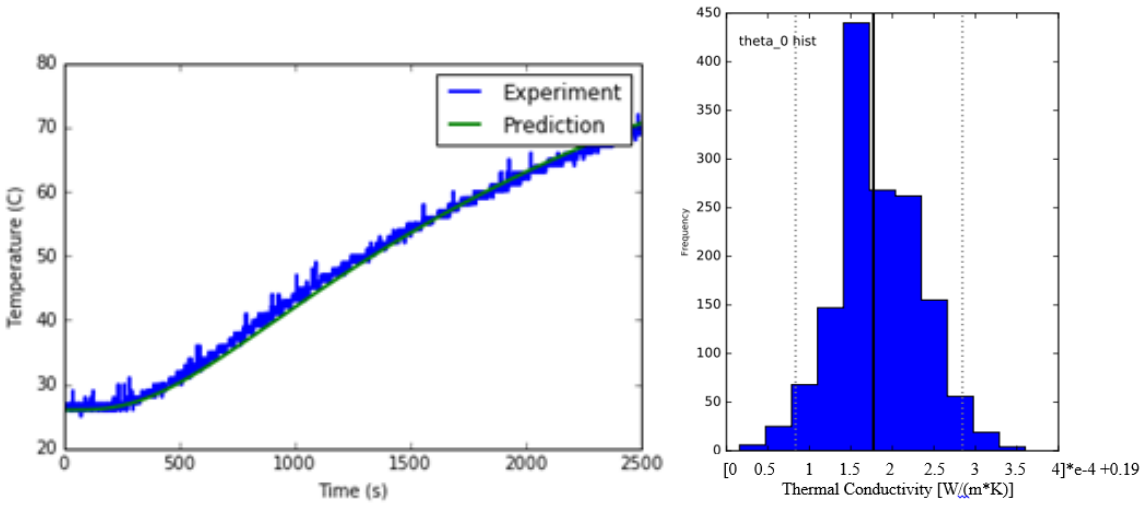

Figure 3.4: a) Predicted vs. measured centerline temperature response of acrylic material
b) Results of thermal conductivity search

3.1.2.2 Alternative Setup to Find Thermal Conductivity

The temperatures of the top, middle, and bottom portion of the acrylic can be seen in Figure 3.5. The average heat flux from the top and bottom heat flux gauges were also plotted. The average of the two heat fluxes were used due to the heat losses that were apparent from the 9% difference between the two heat flux gauge readings on average. This implies that there is room for improving the experimental setup to minimize these heat

losses. The average thermal conductivity over the time period was found to be 0.184 W/(m*K) with a standard deviation of 0.002 W/(m*K). This value falls within the range of previously found values as well, and can be used in conjunction with the previous setup to test for thermal conductivity [18]. Unfortunately, the uncertainty in the heat flux sensor's temperature and heat flux measurements were unspecified.

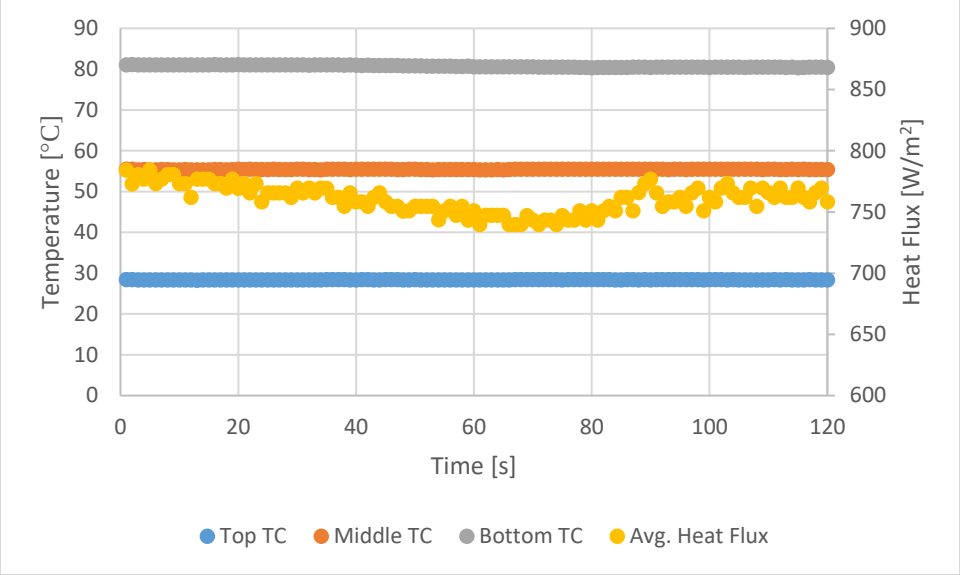

Figure 3.5: Temperatures of acrylic and the average heat flux from the top and bottom heat flux gauges

3.2 Cone Calorimetry

The oxygen consumption (cone) calorimeter is a vital tool used to measure key flammability parameters of materials, such as heat release rates, heats of combustion, smoke production rates, and mass loss rates. The cone calorimeter was used to test the seven different insulation materials of interest in order to gain an insight to the ignition behaviors observed previously in the ember ignition tests. Each material was tested at 15 kW/m^2 and 25 kW/ m^2 at least once, and at 35 kW/ m^2 at least twice. The samples were

prepared in 10 cm x 10 cm (4” x 4”) pieces, wrapped with two layers of aluminum foil with the shiny side facing the sample. Each sample’s mass was measured before and after testing as well. The heat flux incident on the sample was calibrated such that the samples were to be 25 mm (0.98”) away from the cone heater. Tests were run until they either ignited, or until 300 seconds; no ignition was ever observed to occur after 300 seconds, as the volatile production rate was negligible as seen by the non-changing mass of the samples.

A before and after comparison of the seven different insulations at a heat flux of 35 kW/m^2 can be seen in Figure 3.6. The XPS and EPS appear to have completely volatilized and left little residue. The NFR-cellulose and NFR-denim also have little mass left after the test, though tiny ash fibers/shreds can be seen to be left in the pan. The FR-cellulose and FR-denim both have a sizeable amount of char residue left, though the volume did get smaller due to the volatilization. Finally, the PUR has residue left after the test as well. However, this residue is brittle and will crack under pressure.

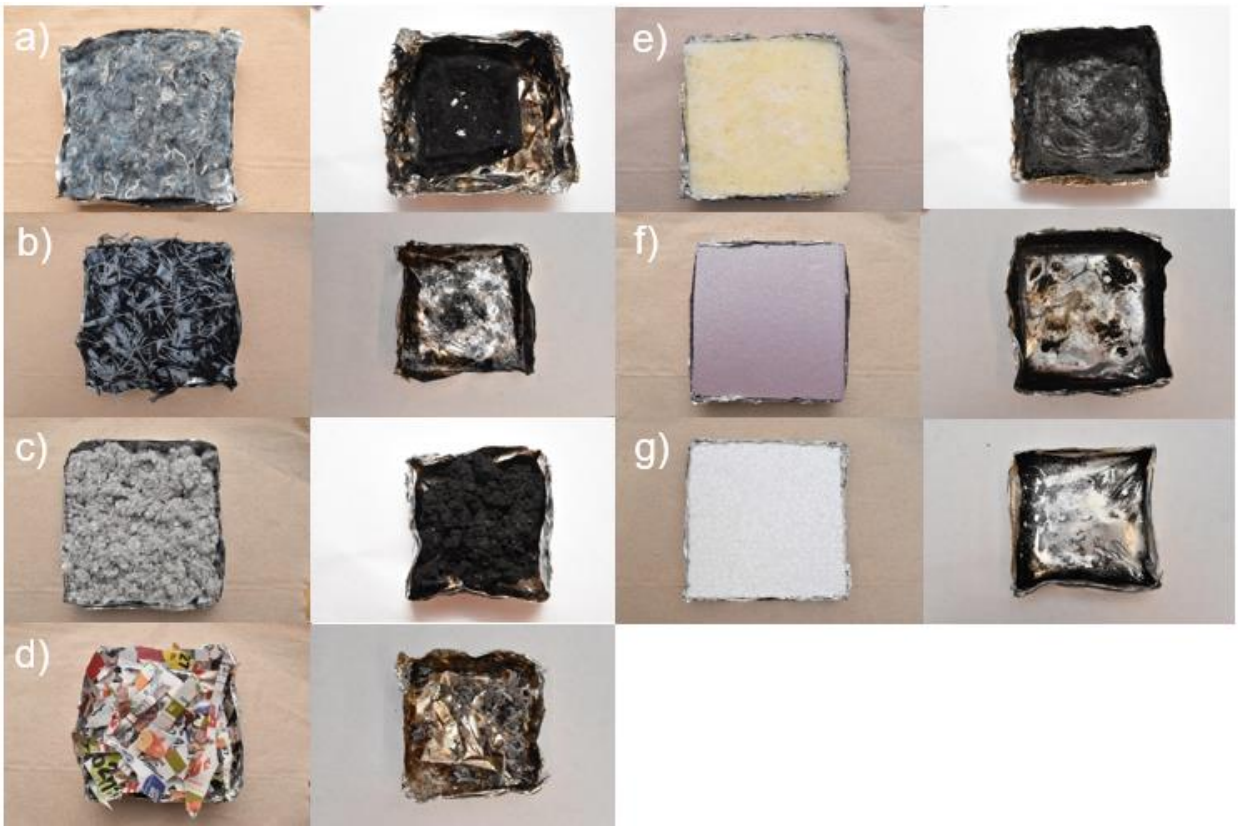

Figure 3.6: Cone Calorimetry Samples at 35 kW/m^2

left) before; right) after
a) FR-denim b) NFR-denim c) FR-cellulose d) NFR-cellulose e) PUR f) XPS g) EPS

3.2.1: Ignition Time Comparison

The times to ignition of the various cases in the cone calorimeter can be seen in Figures 3.7 and 3.8, as well as in Table 3.1. The error bars shown in this section represent the scatter in the data, represented by the Student's t-distribution for a 95% confidence interval. During the 15 kW/m^2 cases, XPS and EPS do not ignite, while at 25 kW/m^2 EPS does not ignite. Also, during some of the tests, most notably the FR-cellulose at 15 kW/m^2 and 25 kW/m^2 some tests would show no-ignition, while other tests would ignite. In order

to better visualize this trend, columns were stacked for the cases of combined ignition/non-ignition results to obtain an adjusted ignition time. The bottom column represents the average weighted ignition time for the cases that did ignite. The top column represents the weighted average of the non-ignition time, where 300 seconds was used as the time for non-ignition. The adjusted ignition time was calculated, where $p_{non\text{-}ign}$ represents the probability that the sample did not ignite.

$$t_{ign_{adjusted}} = t_{ign_{avg}} * p_{ign} + 300 * p_{non-ign} \tag{3.5}$$

For example, two out of the three FR-cellulose (15 kW/m^2) tests did not ignite, while the one that did ignite took 75 seconds. Therefore, the adjusted column height would then be 225 seconds.

$$t_{ign_{adjusted}} = 75 * \left(\frac{1}{3}\right) + 300 * \frac{2}{3} = 225\ seconds \tag{3.6}$$

In all cases of material comparisons, there is a clear trend where the ignition times decrease with increasing heat fluxes. Because of the higher heat fluxes, the materials are able to volatilize and ignite much quicker. The non-flame retarded samples also have faster ignition times compared to the flame retarded samples, due to the efficacy of the various flame retardant mechanisms.

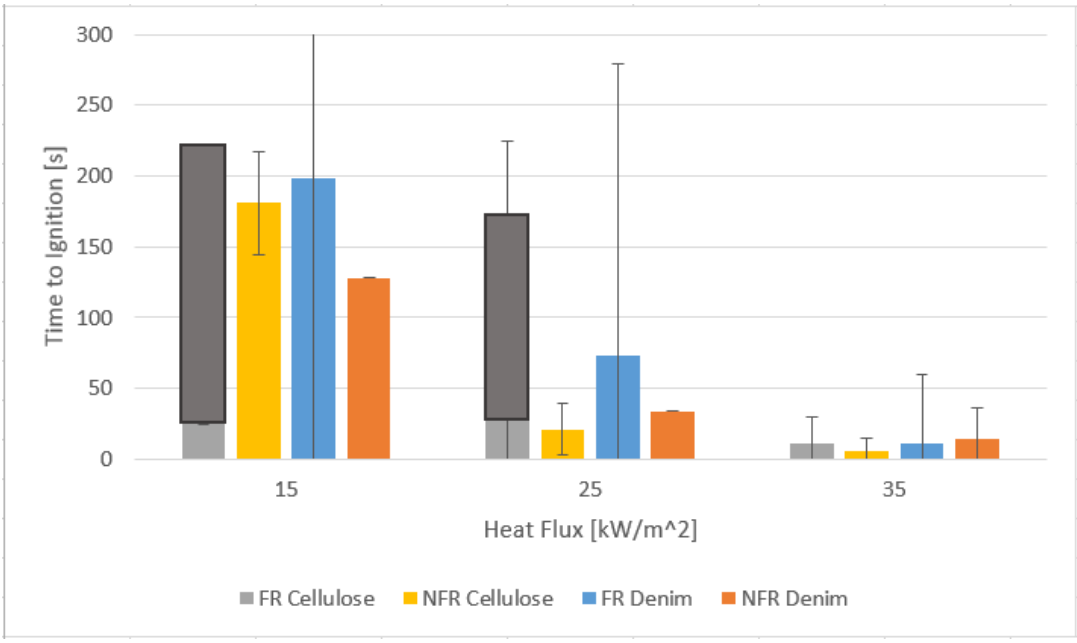

Figure 3.7: Cone calorimeter ignition times of FR vs. NFR Cellulose and Denim

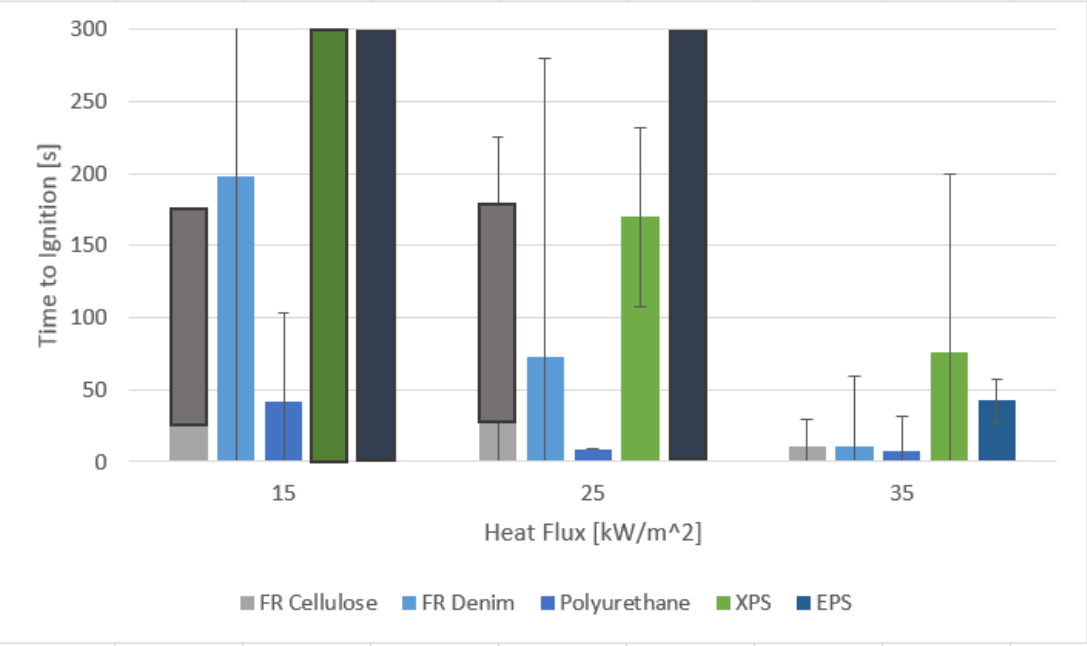

Figure 3.8: Cone calorimeter ignition times of FR vs. NFR cellulose and denim

Table 3.1: Cone calorimeter ignition times

Material	Heat Flux [kW/m^2]	TTI #1	TTI #2	TTI #3	TTI #4	TTI #5	TTI #6
FR-Cellulose	15	75	NI	NI	-	-	-
	25	18	NI	20	18	161	-
	35	5	10	17	-	-	-
NFR- Cellulose	15	187	175	-	-	-	-
	25	18	24	-	-	-	-
	35	2	6	8	-	-	-
FR-Denim	15	160	236	-	-	-	-
	25	28	154	66	56	48	120
	25	7	19	88	86	133	
	35	19	3	-	-	-	-
NFR- Denim	15	128	-	-	-	-	-
	25	34	-	-	-	-	-
	35	18	11	-	-	-	-
PUR	15	32	52	-	-	-	-
	25	9	-	-	-	-	-
	35	11	3				
XPS	15	NI	NI	-	-	-	-
	25	172	188	149			
	35	47	60	120			
EPS	15	NI	-	-	-	-	-
	25	NI	-	-	-	-	-
	35	40	45	-	-	-	-

When all of the materials are compared, the cellulosic materials have on average, lower ignition times compared to XPS and EPS. Polystyrene has a low melting point, but a high vaporization point. Almost immediately when the cone heater starts heating up the XPS and EPS, the materials melt and form a tar-like residue, seen in Figure 3.9. Evidence of this can further be seen in the low heat flux tests where both XPS and EPS melt and lose 20% and 34% of their weights respectively, but do not ignite. Furthermore, the tar forms in random configurations, which can affect the repeatability of these tests.

Figure 3.9: Residue left after non-ignition cases of EPS (left) and XPS (right)

Evidence of this occurs during the ember ignition tests as well, seen in Figure 3.10. The ember is initially able to volatilize the fuel in its immediate vicinity, leading to the flash flames that were observed; however, if the embers are stationary or ingrained into the wood flooring, the XPS can only be melted by radiation. This results in the non-ignition case and the similar black residue is formed.

Figure 3.10: Black residue on the inside of XPS after ember ignition test

The relationship between heat flux and distance from the cone heater can be seen in Figure 3.11 for the case of 30 kW/m^2, which was obtained by Schartel and Hull [19]. It should be noted that the immediate melting of the XPS/EPS causes the heater to be at a

farther distance from the material, thus providing a smaller heat flux to the material for almost the entire test. The initial thickness of the XPS is 25.4 mm (1") while the initial thickness of the EPS is 18 mm (3/4"). It should be noted that the effect should be smaller for lower heat fluxes and larger for higher heat fluxes. The maximum heat flux drop for 15 and 25 kW/m^2 should therefore be at a maximum of 3-5 kW/m^2. Even if the ignition times of the cone calorimeter cases that are 10 kW/m^2 higher are used, the cellulosic materials are still more likely to ignite compared to the XPS and EPS. The case can then be made that the cone calorimeter tests can be used as a screening tool for the ignitability of materials in general, as this correlates well with the results from the ember ignition tests.

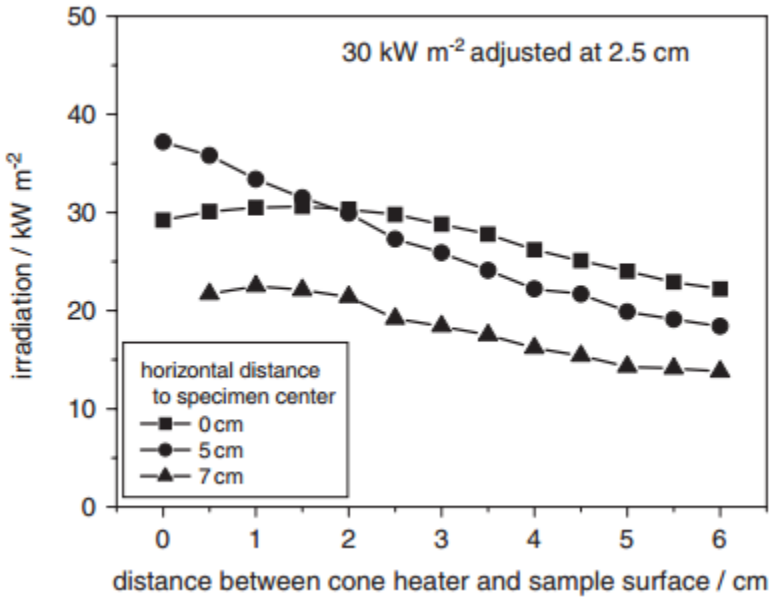

Figure 3.11: Heat flux vs. distance between cone heater and sample surface [19]

Although the melting effect is not large, and should not impact the overall trend comparisons between the cellulosic and polymeric materials, the effect should still be noted, especially when comparing XPS and EPS to values found in literature. The average time

to ignition for our EPS was 42.5 seconds with a standard deviation of 3.5 seconds. Bakhtiyari et al. found their average time to ignition for FR-EPS at 35 kW/m^2 was 102 seconds with a standard deviation of 43.7 seconds [20] for a sample thickness of 40-50 mm (1.57”- 1.97”). Because of this difference in sample thickness, the heat flux drop should almost double and the larger ignition time and standard deviation can be attributed to the lower incident heat flux trends as seen previously. Furthermore, An et al. found the ignition time for a 3 cm (1.18”) thick sample of FR-XPS at 35 kW/m^2 to be 44 seconds, while a 2 cm (0.79”) thick sample of FR-EPS had an ignition time of 54 seconds [21]. They were also able to ignite EPS at 25 kW/m^2, and had an ignition time of 69 seconds for a 4 cm sample of EPS. These results show the large spread in cone calorimeter results that can occur between not only test results, but between researchers as well. It appears that a better characterization of meaningful test conditions needs to be put in place to better understand the results. Bakhyitari also tested rigid PUR foam and found ignition times to be about 5 seconds, which is comparable to our result of 7 seconds.

There is a clear trend where the uncertainty of the ignition results becomes smaller for higher heat fluxes, which is consistent with prior results [22]. The time to ignition appears to be less sensitive to the inherent variability in the material, as might be associated with moisture and flame retardant homogeneity, at higher heat fluxes, just as was the case with the ember ignition tests.

3.2.2 Heat Release Rate (HRR)

In order to achieve meaningful cone calorimeter results, precautions with sample thicknesses must be made. If the sample is too thin, the obtained peak heat release will be

largely dependent on the amount of fuel available in the sample. Schartel and Hull [19] compiled various graphical trends of heat release data in order to show various cases, as seen in Figure 3.12.

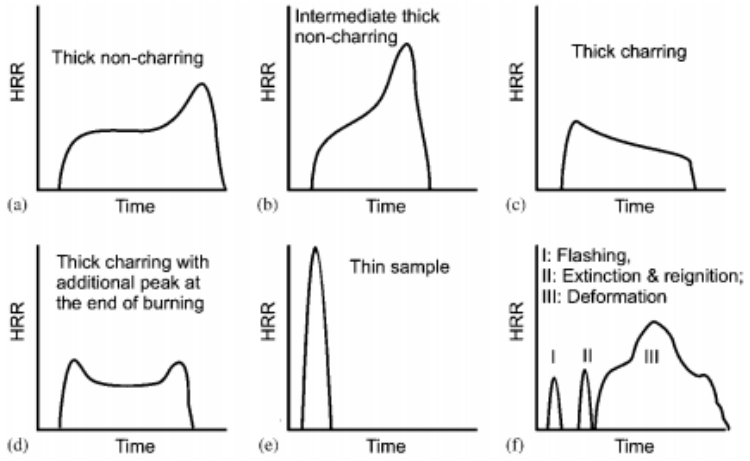

Figure 8. Typical HRR curves for different characteristic burning behaviours.

Figure 3.12: Typical HRR curves for different characteristic burning behaviors [19]

The heat release data for the standard cases of 35 kW/m^2 were compiled. FR-denim, FR-cellulose, NFR-cellulose, XPS and EPS all seem to follow the thick and charring patterns as would be expected, seen in Figures 3.13 for the cellulosic materials and 3.14 for the polymeric materials. The layer of char that is formed becomes a barrier to the heat and mass transfer, thus dropping the HRR.

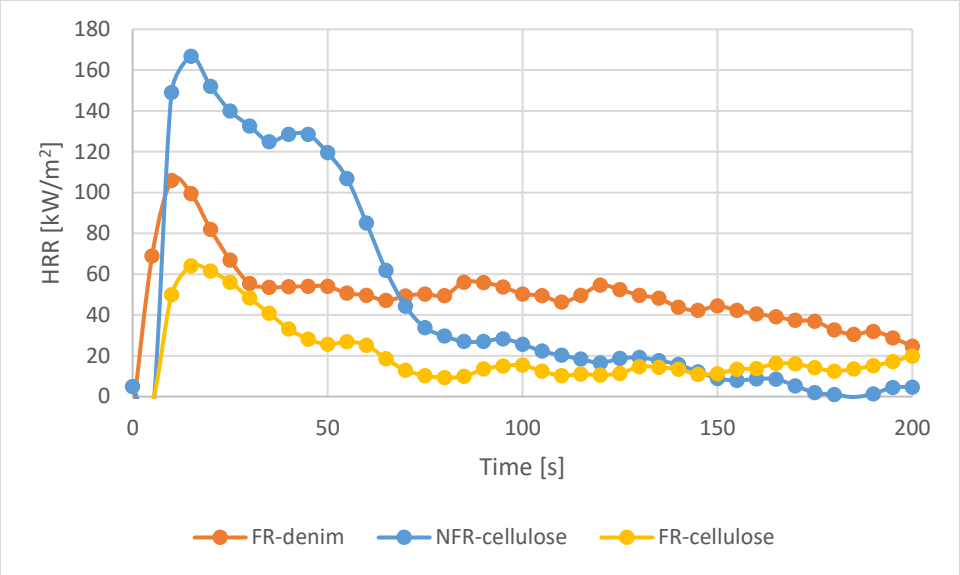

Figure 3.13: HRR of thick-charring cellulosic materials with a 35 kW/m^2 heat flux

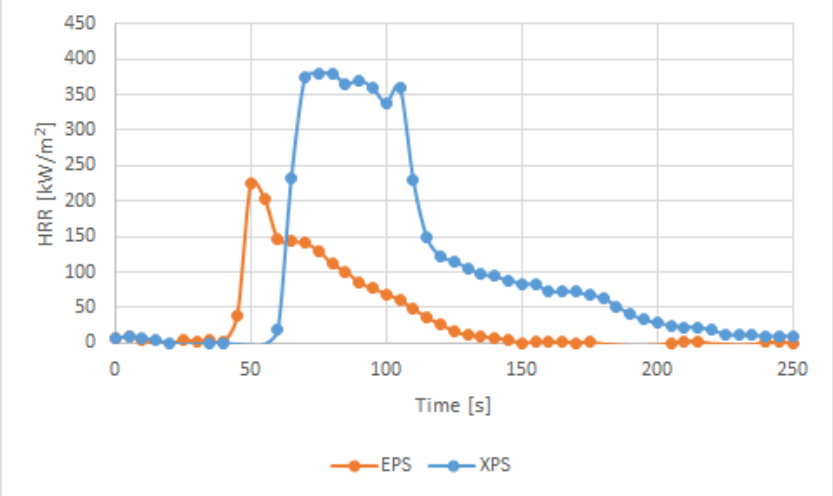

Figure 3.14: HRR of thick-charring polymeric material with a 35 kW/m^2 heat flux

The HRR curve for NFR-denim can be seen in Figure 3.15. NFR-denim has a more rounded HRR curve, and may have been too thin of a sample, thus affecting the peak heat release rate as well as a possible decrease in ignition time [22]. Care should be taken in subsequent tests to ensure more fabric be used.

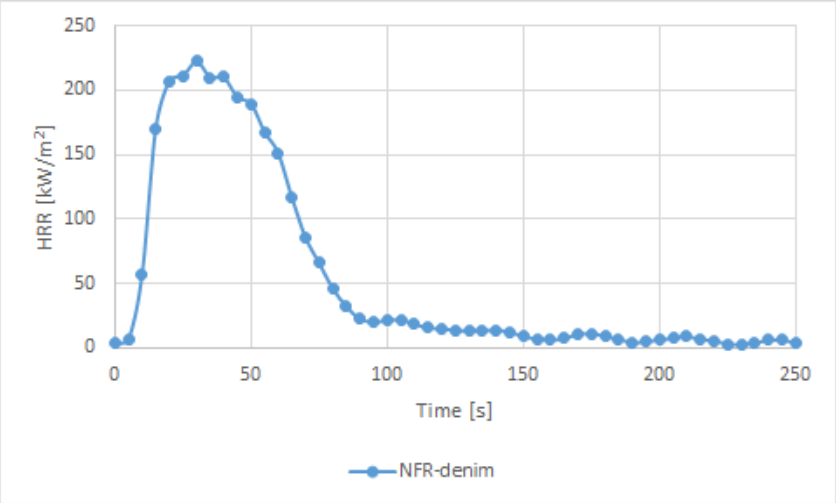

Figure 3.15: HRR of thin-charring cellulosic material with a 35 kW/m^2 heat flux

The PUR HRR pattern resembles a thick non-charring sample, as seen in Figure 3.16. The sample achieves an initial HRR plateau, and maintains this rate until the pyrolysis zone reaches the backside of the sample. Once this occurs, heat is essentially built up in the sample, due to the insulating glass wool on the backside of the sample, and continues to build up until the end of the test.

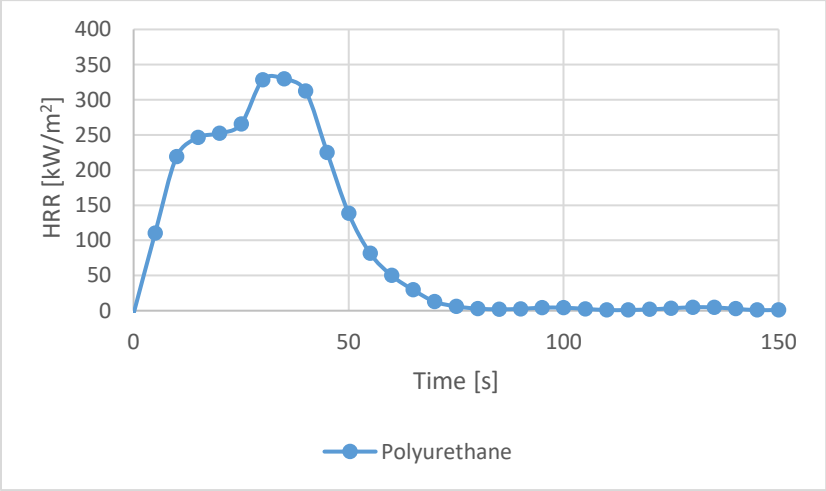

Figure 3.16: HRR of thick non-charring polymeric material with a 35 kW/m^2 heat flux

3.2.2.1: Analysis

The peak HRR of the cellulosic materials can be seen in Figures 3.17, where the t_{95} uncertainty is plotted and all tests that were only tested once are denoted by a red-x on the top of the bar. The peak HRR of the FR samples all have much lower peaks, compared to their NFR counterparts, where the FR in denim decreases the peak HRR by 65%, and the FR in cellulose decreases the peak HRR by 61% across the average of the three heat fluxes. Similarly, White et al. [23] found that the peak HRR decreased by 51% after applying a phosphate flame retardant coating on cotton. The peak HRR also appears to have a linear relationship with heat flux, and was shown to be the case with other textiles as well [19].

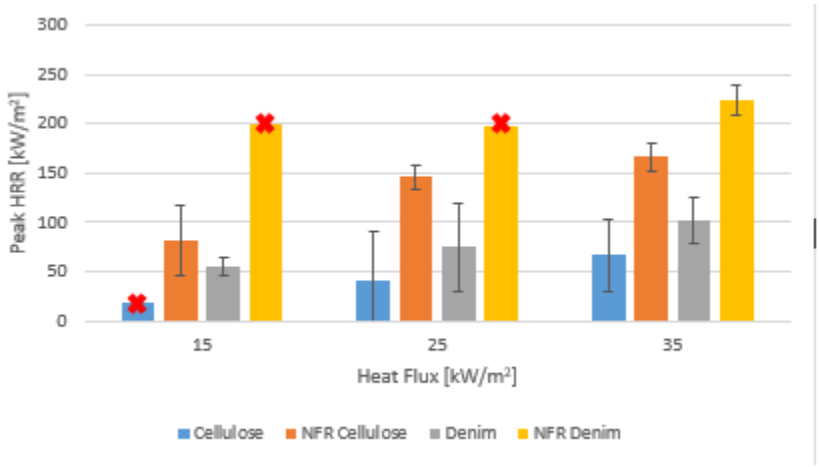

Figure 3.17: NFR vs. FR material peak HRR

The peak HRR of the FR insulation can be seen in Figure 3.18. The peak heat release rates are not taken into account for the three non-ignition cases, XPS and EPS at 15 kW/m^2 and EPS at 25 kW/m^2. The peak HRR appears to follow the same linear trend mentioned above for the other materials. The cellulosic materials appear to have a much lower peak heat release rate compared to the polymeric materials. Even though the

cellulosic materials had comparable uncertainty to the polymeric materials for ignition times, the peak HRR is more consistent. The XPS and EPS, however, still have larger uncertainties for HRR. This could again be attributed to uneven distributions of melt in the aluminum pan. As a metric, peak HRR shows a large portion of the fire risk involved with certain materials, but it does not show which is more likely to ignite under certain conditions. Clearly though, once the XPS, PUR, or EPS do ignite, they pose severe issues to the safety of the built environment.

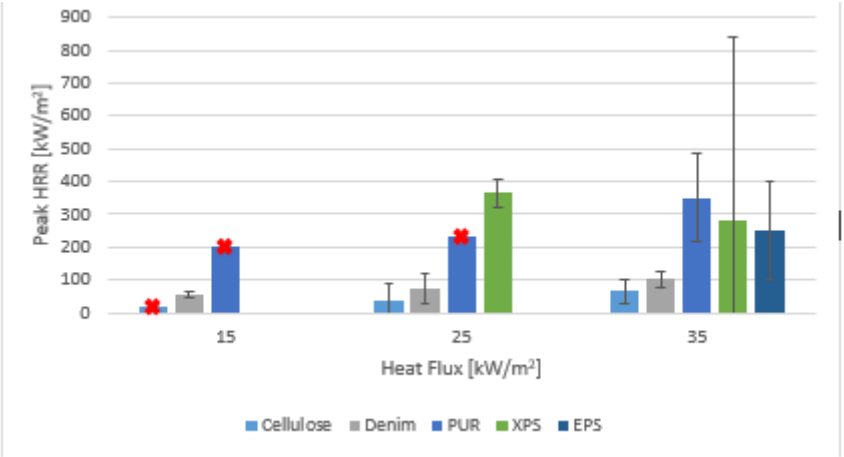

Figure 3.18: Peak HRR of insulation material

One way that researchers have tried to simplify the fire risk of materials is the use of a metric called fire growth rate (FIGRA), which is essentially the peak heat release rate divided by the time to peak heat release rate [19]. One of the benefits to using this metric is that it allows for the inclusion of non-ignition cases. It should be noted that the index is not all encompassing and does not fully represent the fire hazards of materials, since it is purely based off of heat release rates. Flame spread is not a measurable factor using cone

data. Fire scenarios encountered are typically dependent on many other factors, so caution must be used when weighing these metrics too seriously.

Figure 3.19 shows the values of FIGRA for the FR-insulation materials. Higher values for FIGRA are correlated with a lower resistance to flammability, and thus similar trends to the peak HRR can be observed, where increasing heat fluxes pose a greater threat. Furthermore, it also shows that the cellulosic materials have a slightly worse flame resistance performance compared to the polymeric materials, except when compared to PUR.

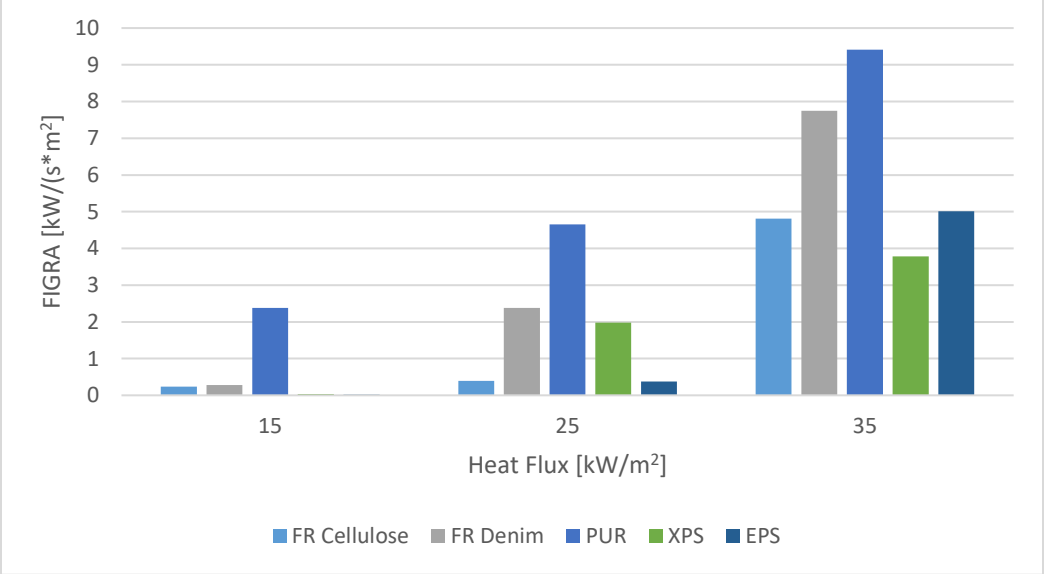

Figure 3.19: FIGRA of materials

The average mass loss rate at ignition of the seven materials can be seen in Figure 3.20. Ignition of a fuel occurs in the cone calorimeter if the amount of volatiles being produced are enough to form a combustible mixture that can be ignited by the spark igniter. The mass loss rate at ignition is thusly an important measure, comparable to critical ignition

temperature that can indicate when a fuel will ignite. Furthermore, the critical mass loss rate is independent from the incident heat flux, since the mass loss rate is temperature controlled. The critical mass loss rates in our tests were about 1-6 g/(s*m^2), which agrees with values found in literature [19]. Figures for the peak MLR of the materials can be found in Appendix H.

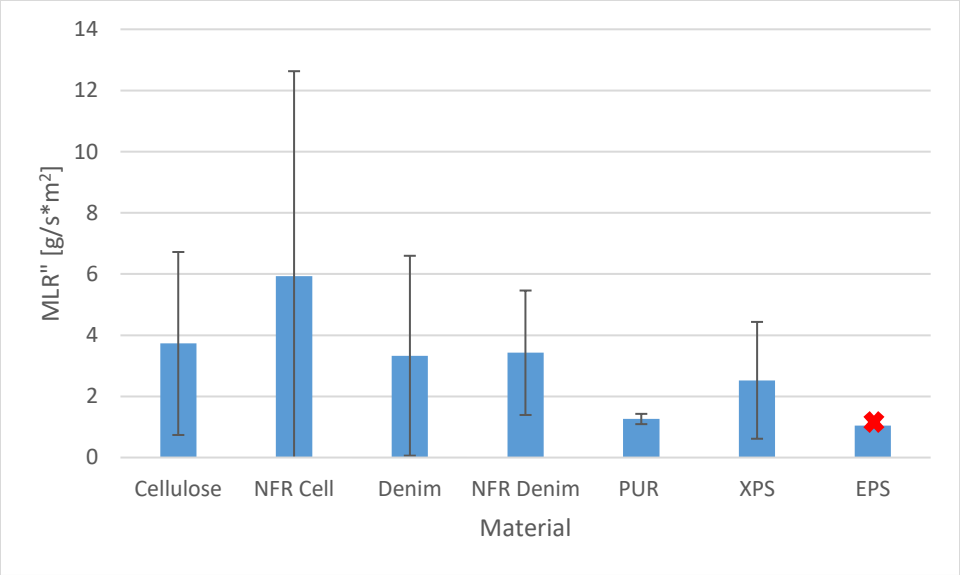

Figure 3.20: Average mass loss rate at time of ignition

The results from the cone calorimeter for PUR have portrayed it to be more flammable than the other materials. It had the lowest time to ignition, a high peak HRR, and the highest fire growth rate. However, during the ember ignition tests, the PUR would not ignite. If the PUR were to ignite, the cone results show that the intensity that it would burn would be higher than the other materials. Yet, in real scenarios, ignition is difficult for it to achieve without a consistent heat flux. These results demonstrate that the cone calorimeter cannot fully predict whether all materials are more flammable than others. In

certain cases, such as with PUR, the effects of the flame retardants are not evident in the data. In the future, cone calorimeter data can be paired with other tests to show the true implications that these flame retardant additives have on ignition.

3.2.3 Other Effects

3.2.3.1 Effects of Relative Humidity

Samples of FR-denim and FR-cellulose were prepared at three different conditions: oven-dry, 50% relative humidity (RH), and 70% relative humidity. Three samples at each condition were prepared. The average moisture content of the samples at 50% RH were 5.1% and 7.0% for the FR-denim and FR-cellulose, respectively, and were 7.2% and 10.1% at 70% RH, respectively. Tests were performed within 30 seconds of taking the samples out of the oven/humidity chamber in order to minimize the moisture content change. Fabric moisture content typically adjusts quickly, so the moisture content change over time was recorded as well. However, both materials only gained <1% moisture content during the time of transit, so the effect can be believed to be negligible.

The ignition times of the FR-denim were scattered for all three conditions, as seen in Figure 3.21. Because of this, there does not appear to be a notable impact of ignition on FR-denim. However, the ignition times for FR-cellulose were much more affected. All of the samples prepared at 50% RH and most samples at 70% RH did not ignite; two out of the three oven-dried samples did ignite, and only took 19 seconds on average. Wood has shown to more than double its time to ignition when conditioned at 90% RH compared to 50% RH [24]. Dimitrakopoulos and Papioannou [25] also found that moisture content was

the most important factor to cone flammability for typical forest fuels. Therefore, the fact that the FR-denim does not seem to be affected by moisture content could be due to a number of reasons. Looking at TGA results, the FR-denim begins to degrade at a higher temperature, compared to the FR-cellulose. Because of this effect, the FR-cellulose may simultaneously be pyrolyzing while drying, which would dilute the volatile gases that are off-gassing. With a higher degradation temperature, the FR-denim may not be affected as much by this effect. Furthermore, the moisture content is roughly 2-3% lower than that of the FR-cellulose. Additional tests should be conducted to narrow down the issues, as well as to decrease the uncertainty between tests.

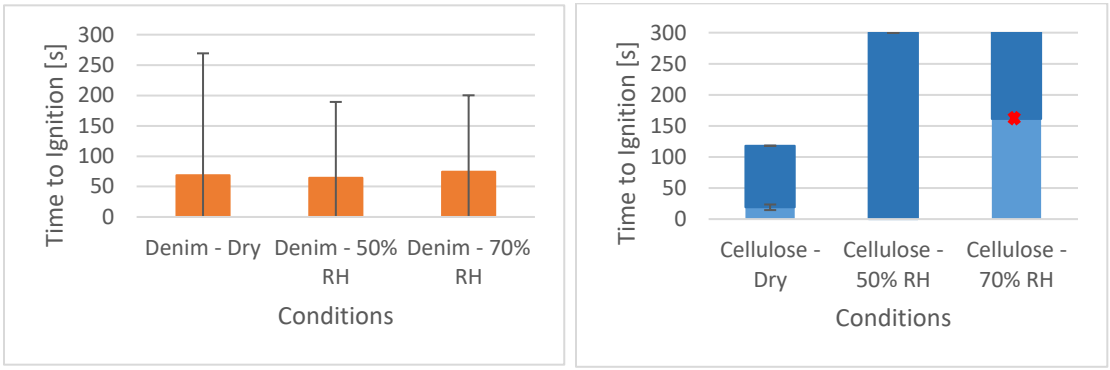

Figure 3.21: Ignition times and Probabilities of Moisture conditioned samples for FR-Denim (left) and FR-cellulose (right)

3.2.3.2 Spalding Number and Blocking Number

The Spalding number, B, is a parameter that can be used to show how much energy is released from a fuel vs. how much energy is required to volatilize it, where c_p is the specific heat of the fluid, h is the heat transfer coefficient, and $\dot{m}''$ is the mass flux. The transient values of h were found using the method described in 3.2.4.2.

$$B = \frac{c_p h}{\dot{m}''} \tag{3.7}$$

The Spalding number can give insight to issues involving the combustion processes on a vaporizing surface, and typically, if the Spalding number is greater than one, any flaming will be self-sustaining. Figure 3.22, shows the average Spalding number prior to ignition, and it can be seen that none of the materials thermally runaway prior to ignition. The main reason these materials ignite is because there is a constant heat source, and therefore, the materials do not have to rely solely on the released heat to combust. The Spalding number can be seen to increase with increasing heat fluxes, though it appears to have roughly the same values between the different materials, except for the case of PUR at 25 kW/m^2. Only one test was performed at this condition though, so additional tests may need to be performed to investigate if it is a discrepancy. On average though, the FR-cellulosic materials have higher Spalding numbers than XPS and EPS.

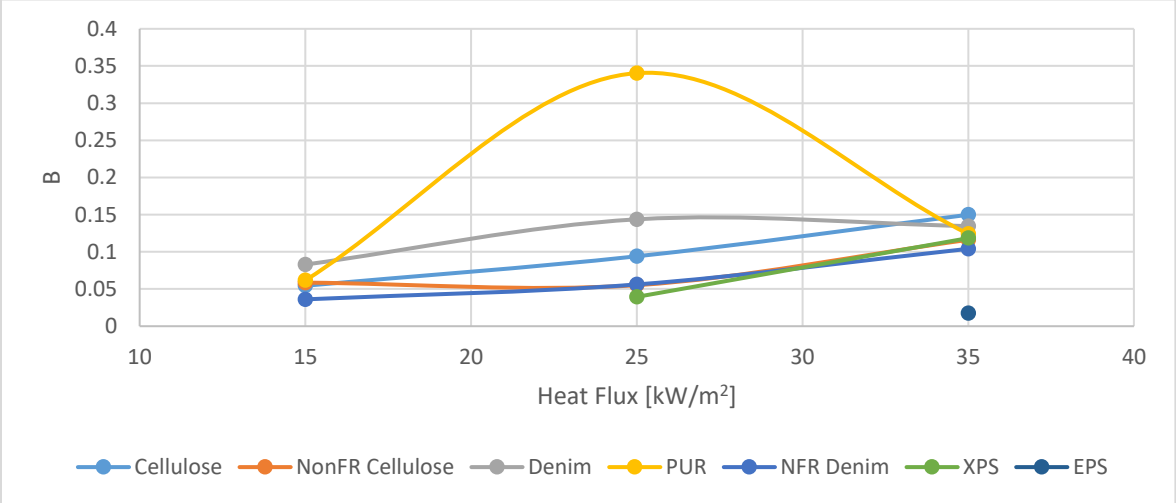

Figure 3.22: Average Spalding number averaged through ignition

Another parameter that was investigated was the blocking number, which accounts for a reduction in heat transfer due to the surface-mass addition during combustion.

$$Blocking\ Number = \frac{\ln(B+1)}{B} \tag{3.8}$$

The blocking effect however, appears to be negligible prior to ignition since the values are not much lower than one, as seen in Figure 3.23.

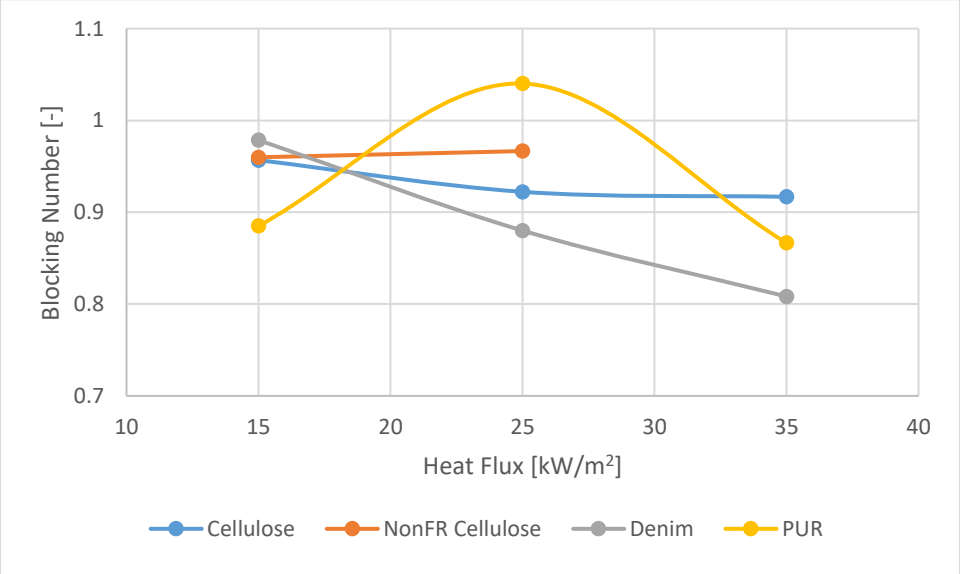

Figure 3.23: Average blocking number prior to ignition

3.2.4: Critical Ignition Temperature

The critical surface temperature of ignition was of interest, in order to see both the trends relative to other material degradation data, in addition to looking at the consistency between different heat fluxes and conditions.

3.2.4.1 Experimental Setup

A k-type, 30-gauge, braided thermocouple was inserted about one millimeter below the surface of each fuel bed, and measured temperature at a rate of 1 Hz, as seen in Figure 3.24. The thermocouple was secured in a manner such that the bead would recede as the material surface receded, and so that there was negligible tension pulling up on the thermocouple. Due to the weight of the thermocouple, the mass data during these tests may have been biased upwards, though the mass loss rate should still be unaffected. Previously, researchers have used thermocouples to obtain surface temperature measurements of samples, which were then used to calibrate an IR pyrometer to be used during experiments [26]. However, the nature of the materials did not allow for accurate surface temperature measurements, as it was difficult to keep the thermocouple on the surface.

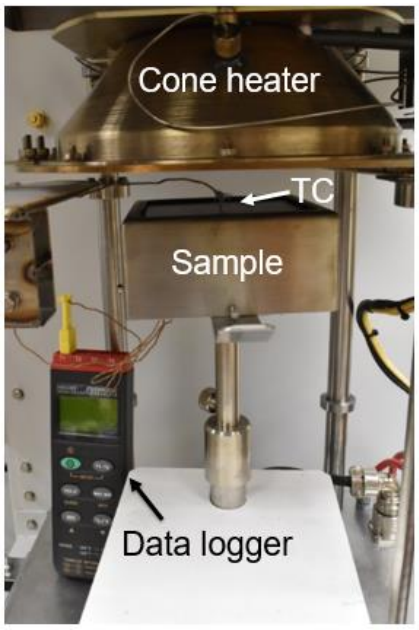

Figure 3.24: Samples with embedded thermocouple

3.2.4.2 Thermal Model

A 1-D model of the temperature of the surface of the material at the time of ignition was used, represented by Figure 3.25 and the equations below, where q''_{heater} is the heat flux from the cone heater, q''_{conv} is the heat loss due to convection, $q''_{re\text{-}rad}$ is the heat loss due to re-radiation, k_f is the thermal conductivity of the fuel, T_{surf} is the surface temperature of the fuel bed, T_{amb} is the ambient temperature of 25 °C, α_f is the thermal diffusivity of the fuel bed, t_{ign} is the time at ignition, h is the heat transfer coefficient, Nu is the nusselt number, k_{air} is the thermal conductivity of the air, L is the characteristic length of the fuel bed, Ra is the Rayleigh number, ε is the emissivity of the fuel bed, and σ is the Stefan-Boltzmann constant. The materials typically char within 10% of the run-time, and thus the emissivity was chosen to be 1.

$$q_{heater}" - q_{conv}" - q_{re-rad}" = \frac{k_f(T_{surf}-T_{amb})}{2}\sqrt{\frac{\pi}{\alpha_f t_{ign}}} \quad (3.9)$$

$$q_{conv}" = h(T_{surf} - T_{amb}) \quad (3.10)$$

$$h = \frac{Nu*k_{air}}{L} \quad (3.11)$$

$$Nu = 0.15Ra^{\frac{1}{3}} \qquad 8*10^6 < Ra < 1.5*10^9 \quad (3.12)$$

$$q_{rad}" = \varepsilon\sigma({T_{surf}}^4 - {T_{amb}}^4) \quad (3.13)$$

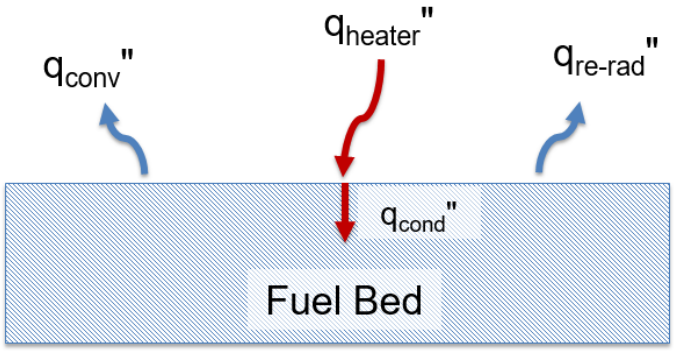

Figure 3.25: Model of the heating of a 1D thermally thick sample

The equations were solved simultaneously resulting in Figure 3.26 for FR-denim at 35 kW/m^2.

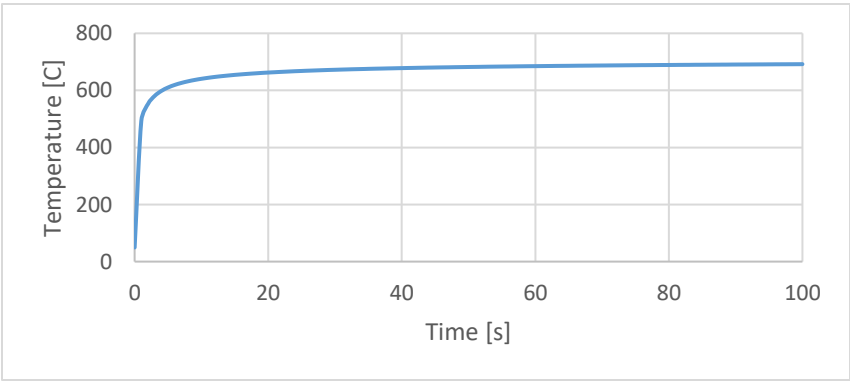

Figure 3.26: Surface temperature of FR-denim at 35 kW/m^2

Furthermore, since the thermocouple was not actually measuring the surface temperature, but 1 mm (0.04") below, a correction was necessary to be made to the temperature curve. The temperature of the thermocouple was treated as a linear interpolation between the surface temperature and the cold boundary, using the thermal boundary growth, where T_{surf} is the temperature of the surface of the fuel bed, T_{TC} is the temperature reading from the thermocouple, δ_{TC} is the depth of the thermocouple within the fuel bed, $\delta(t)$ is the thermal boundary layer thickness over time, α is the thermal diffusivity of the fuel bed, and t is the amount of time that the fuel bed has been heated by the cone heater.

$$\frac{T_{surf}-T_{TC}}{\delta_{TC}} = \frac{T_{surf}-T_o}{\delta(t)} = \frac{T_{surf}-T_o}{\sqrt{\alpha t}} \tag{3.14}$$

3.2.4.3 Results

From the thermocouple test results, the critical surface temperatures can be seen to be similar to the theoretical results using thermocouple depth, as seen in Figures 3.27 and 3.28 for FR-denim and PUR. However, the critical surface temperature is quite sensitive to the specified depth in the temperature interpolation. For example, if the depth of thermocouple was actually 0.5 mm instead of 1 mm, the temperature would have almost a 100 °C difference, depending on the time of ignition. As the time approaches a long time period though, the difference becomes smaller.

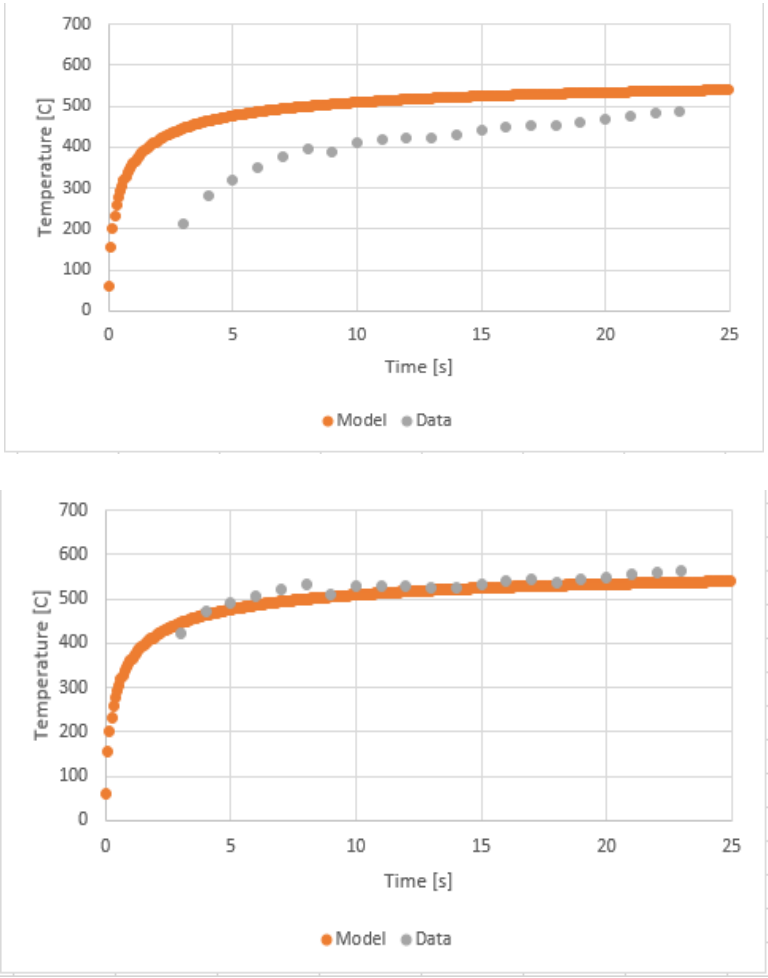

Figure 3.27: FR-denim at 25 kW/m^2 at 0.5 mm (top) vs at 1 mm (bottom)

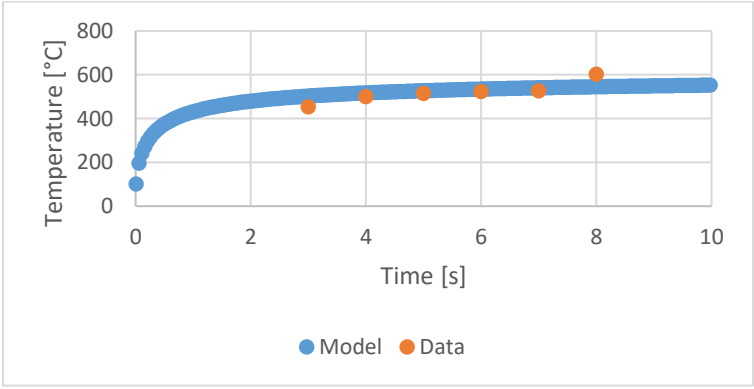

Figure 3.28: PUR at 25 kW/m^2 at 0.00085 mm

There were issues with the thermocouple test involving the NFR-cellulose, as seen in Figure 3.29. Because the thermocouple was not embedded in any material, it was only measuring the air temperature between the pieces of NFR-cellulose. Further issues were encountered with the XPS and EPS, as the material melts almost instantaneously into a liquid about 1 cm (0.4”) thick. Not only are the thermal properties of this liquid unknown, but measurements in this state were unable to be stably measured.

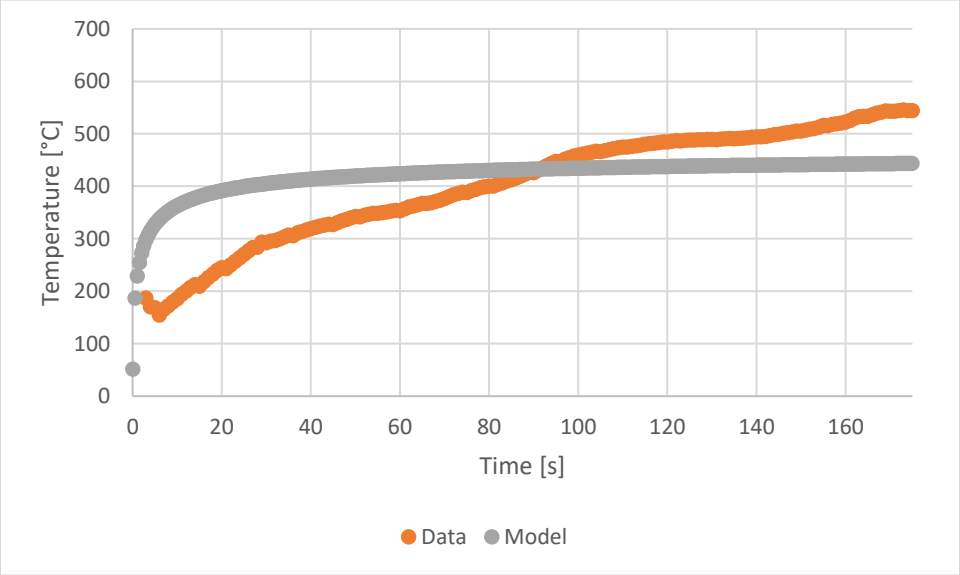

Figure 3.29: NFR-cellulose at 15 kW/m^2

The adjusted surface temperature at the time of ignition recorded by the thermocouples can be seen in Table 3.2, along with the original temperature value. XPS and EPS were not explored, due to the quickly receding surface, as well as the difficulties with good thermocouple contact with the NFR materials. The ignition temperature of PUR can be from 410 - 495 °C [27, 28], while the NFR-cotton cellulose ignition temperature is around 350 °C [29].

Table 3.2: Adjusted surface temperature of materials at different heat fluxes

Material	Heat Flux [kW/m^2]	TC Temp [°C]	Adjusted TC Surface Temp [°C]
FR-Cellulose	15	502	563
	25	371	415
FR-Denim	15	461	507
	25	440	562
PUR	15	367	474
	25	393	625

3.3 THERMOGRAVIMETRIC ANALYSIS

In order to further investigate the material properties of the various insulation, thermal gravimetric analysis was performed for all of the materials. The temperature was swept from 30 °C to 800 °C at a rate of 20 °C/min. A higher temperature rise rate would have been more appropriate to replicate the behavior during smoldering or flaming, but this was the limit of the instrument. This is a typical issue in TGA measurements for fire applications. TGA test results of the FR-cellulose, FR-denim, EPS, and XPS were obtained by a member of our research group, Bonnie Roberts, and were used in conjunction with the NFR-cellulose, NFR-denim, and PUR collected during this period. Five to ten milligrams were used for each test, while air and nitrogen were used as the purge gases.

Ensuring that the sample stayed inside of the crucible was crucial during testing, and therefore, knowing the thermal expansion properties of the various materials was vital. Since the PUR spray foam was not well characterized, a sweep of tests were performed across key temperatures. These tests involved heating small samples of PUR in an oven for

five minutes and noting the changes in volume, as seen in Figure 3.30. Wang et al. [30] and Dick et al. [31] noted that chemistry changes can happen anywhere between 150 °C - 250 °C for PUR, which is why the samples were heated between 150 °C - 300 °C. All samples were shown to either keep a constant volume, or a decrease in volume, making the foam a viable material to be analyzed in the TGA system.

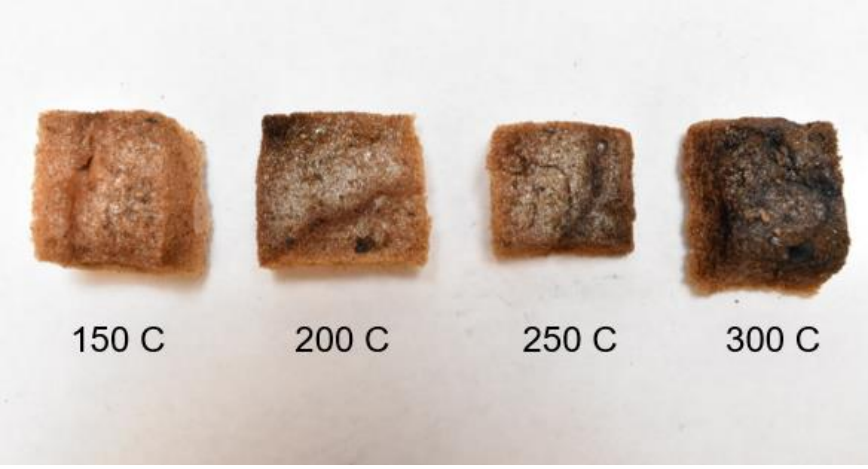

Figure 3.30: Thermal expansion of PUR foam at critical temperatures

3.3.1: Key Results:

Representative TGA curves for XPS, FR-cellulose, and NFR-cellulose can be seen in Figure 3.31. The other TGA curves may be found in Appendix I. XPS is seen to have a later onset temperature, yet only has a one-step reaction with a steep rate of degradation, and thus, decomposes to its residual mass quickest. The FR-cellulose begins degrading earliest, but has much slower degradation rates, and decomposes last. The NFR-cellulose falls in the middle, where its initial reaction has a comparable rate of degradation to the

XPS; however, its second reaction is much slower, and is comparable to that of the FR-cellulose.

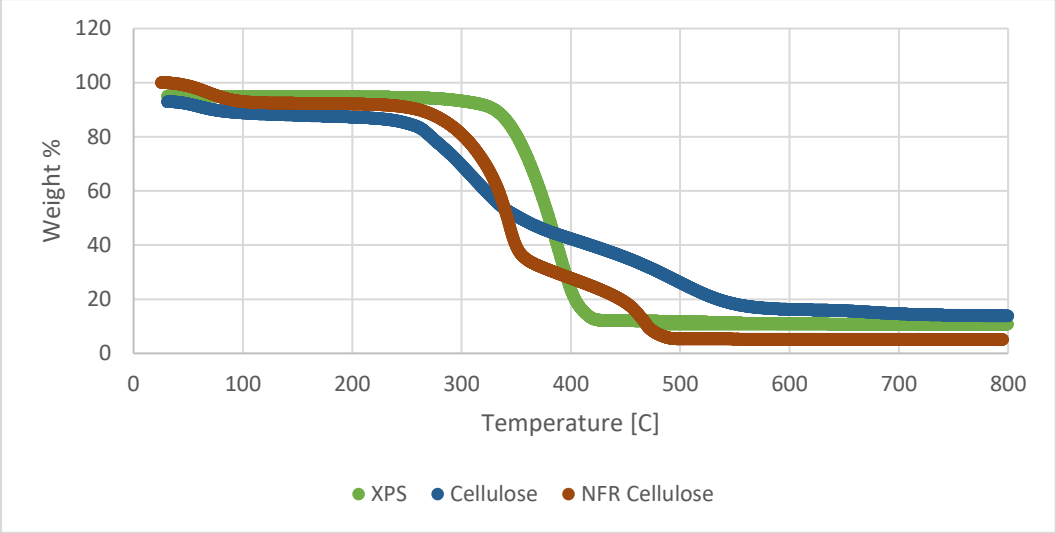

Figure 3.31: Representative TGA curves for air

The peak rates of decomposition for the two different purge gases (air and nitrogen) can be seen in Figure 3.32. The non-flame retarded samples had the highest peak rate of decomposition, whereas the flame retarded samples of the cellulosic materials had the lowest peak rate. These results show the efficacy of flame retardants in reducing the rate of pyrolysis. EPS and XPS had about the same peak mass loss rate, while PUR had a slightly lower peak.

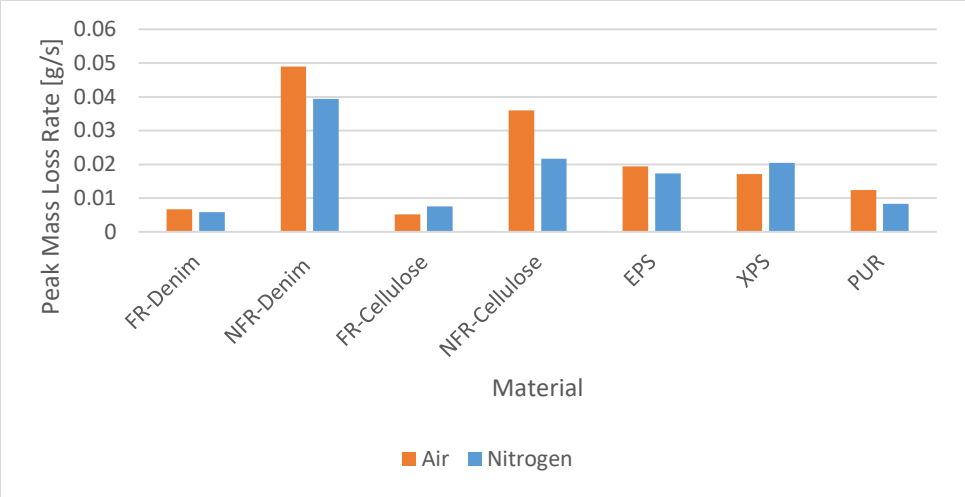

Figure 3.32: Peak mass loss rate from TGA in air and nitrogen environments

Figure 3.32, shows that the temperature of all of these maximum rates of decomposition occur at can be banded between 300 °C – 400 °C for air, and 350 °C -450 °C for nitrogen. Therefore, as these materials are brought up to this temperature, either through radiative heating in the cone calorimeter case or through conduction in the ember case, the rate of volatile production can be seen to near its maximum in this range.

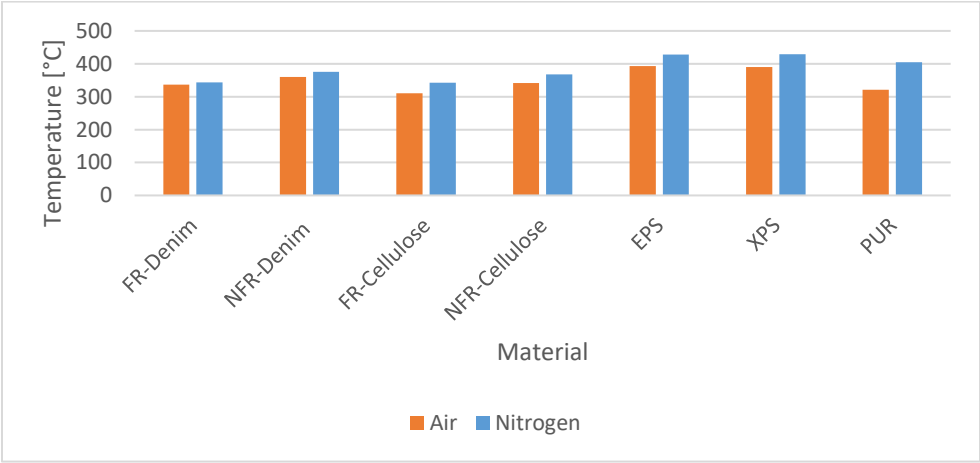

Figure 3.33: Maximum rate of decomposition temperature from TGA in air and nitrogen environments

The onset temperatures of the materials were found using the step tangent method [32], depicted in Figure 3.34 for NFR-denim in air. This method requires using a horizontal line drawn from the baseline weight and intersecting it with a line tangent to the reaction rate.

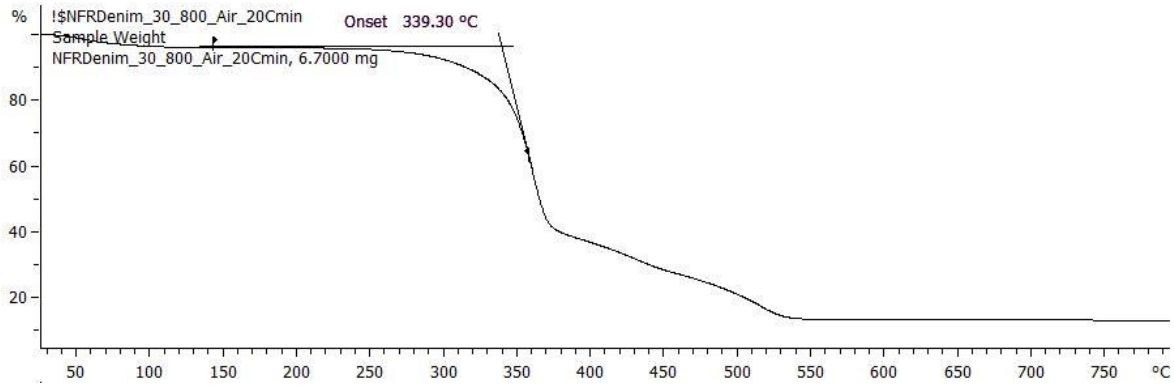

Figure 3.34: Example of step tangent method to find onset temperature of NFR-denim in air

The onset temperatures of the FR materials are slightly lower than the NFR materials, Figure 3.35. This was a similar trend observed by [33], when various flame retardants were tested with rayon fabric. Not only are the onset temperatures lower, but the temperature at which the maximum mass loss occurs is also lower for the FR materials. These trends can shed some insight into the mechanism by which the flame retardants act. The lower temperature at which the materials degrade can be due to the boric acid volatizing, producing char, and also inhibiting the combustion in the vapor phase. By having this reaction occur prior to the temperatures at which combustion occurs, the flame retardant can begin to protect the underlying material earlier. The onset temperatures of the cellulosic materials, which were also the materials that ignited during the ember tests, can

also be seen to have a lower onset temperature compared to the two polymeric materials, EPS and XPS.

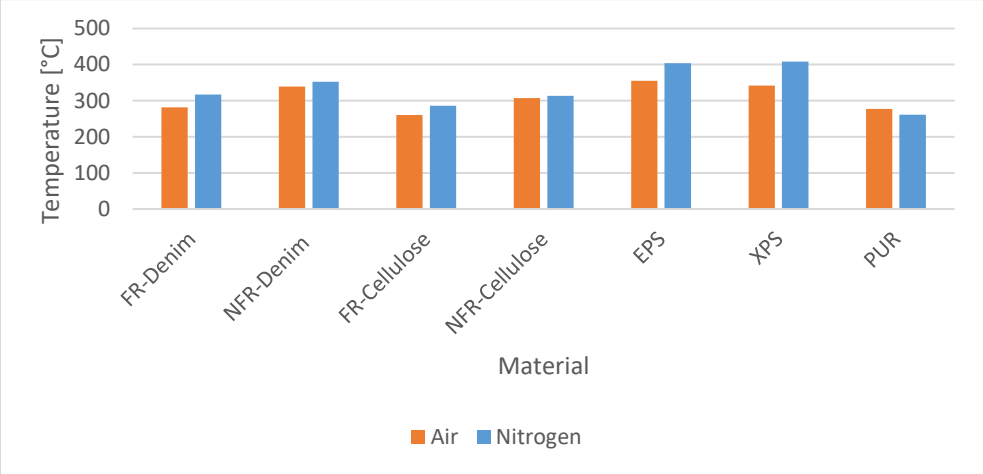

Figure 3.35: Onset temperature of TGA in air and nitrogen environments

The residual mass after TGA was run, Figure 3.36, can be seen to be larger for the cellulosic materials, especially when nitrogen was used as the purge gas. This can show that oxidation is an important process to break down many of the remaining components of the material. The PUR completely volatilizes during both conditions; this did not occur during the cone calorimeter tests, as 36% of its mass remained after the 35 kW/m^2 run was performed. Lower surface temperatures were achieved with the cone, compared with TGA.

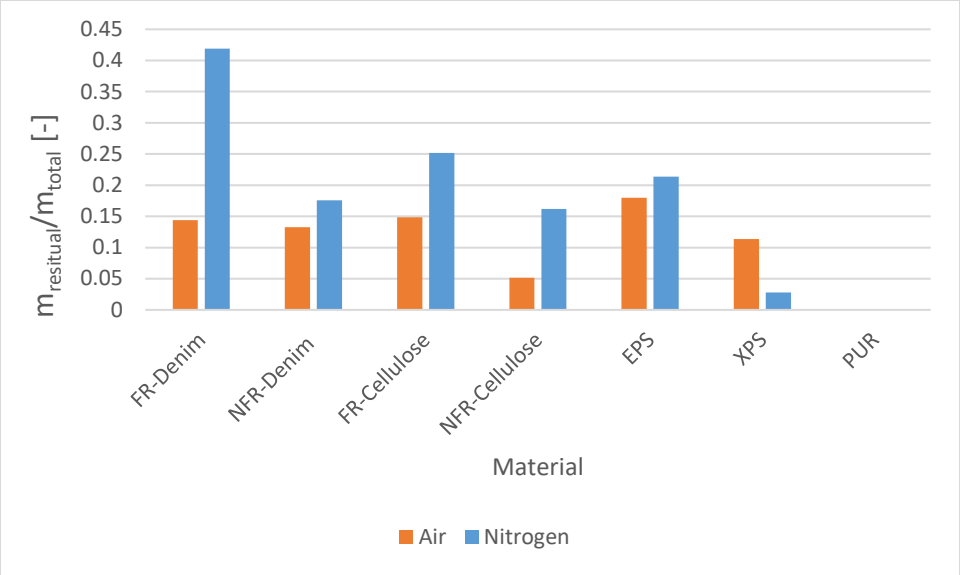

Figure 3.36: Ratio between residual mass and total mass for TGA in air and nitrogen environments

The kinetics of these TGA curves were found using the same process used in Roberts et al. [34]. There is not a clear distinction between the activation energy required for the FR materials vs. the NFR materials, Figure 3.37 – 3.39. This makes sense as the mechanism for the flame retardant is not meant to increase the activation energy, but to affect the amount of heat transfer to both the substrate as well as to interfere with the reactions occurring in the vapor phase. The baseline activation energy of the cellulosic materials are lower than the XPS and EPS though, which coincides with the results from the ember ignition tests as well as the cone calorimeter tests. Because the XPS and EPS requires more energy in order to break and reform bonds, it makes sense that they would have a longer ignition time in the cone calorimeter, and would be provided with insufficient energy from the ember to ignite as well. It should also be noted that the later steps have larger activation energies.

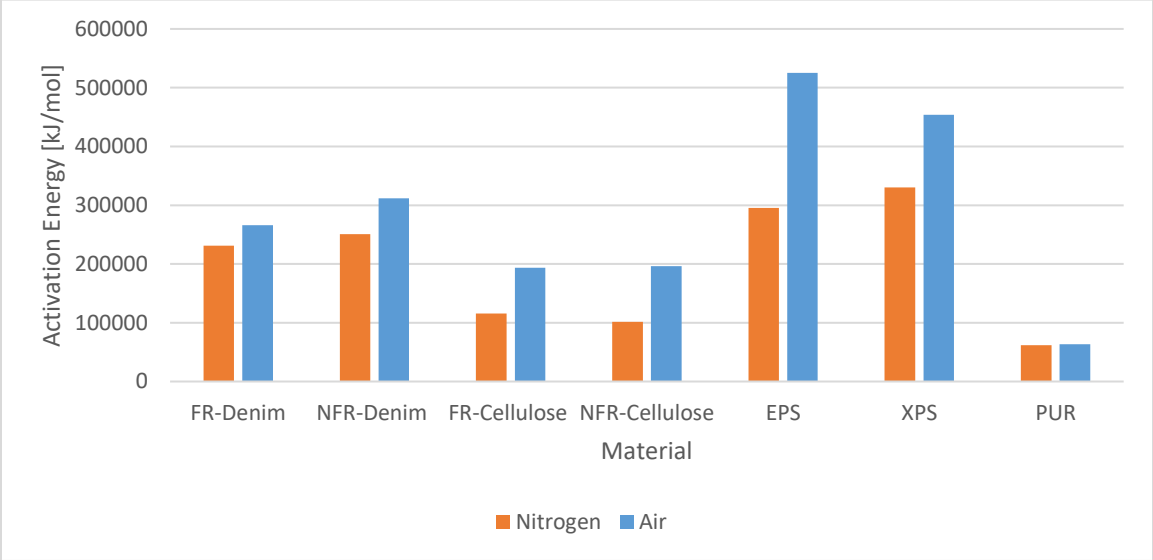

Figure 3.37: Activation energy of 1st step reaction from TGA results in air and nitrogen environments

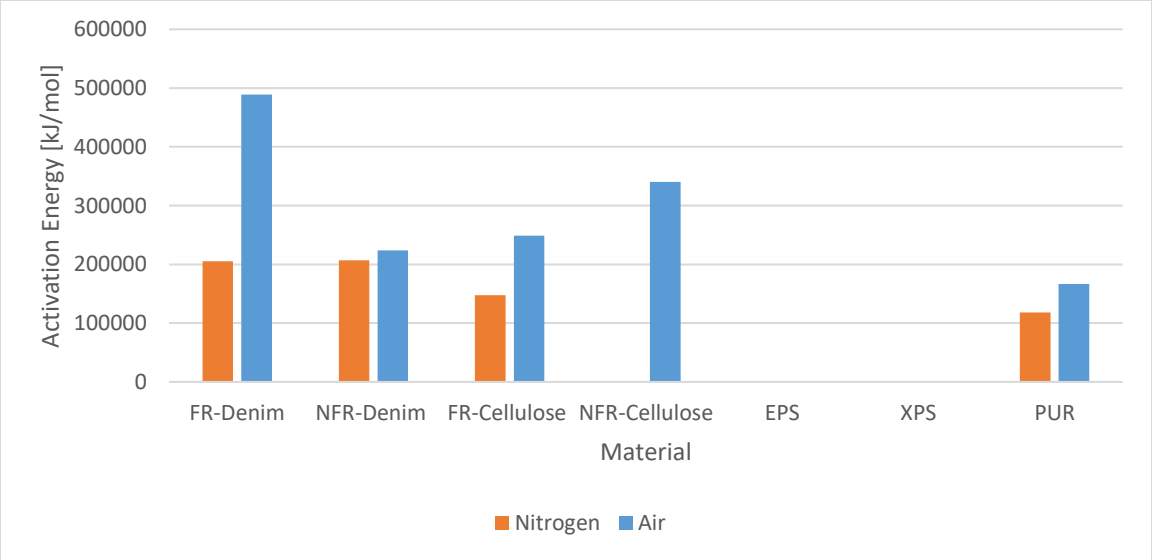

Figure 3.38: Activation energy of 2nd step reaction from TGA results in air and nitrogen environments

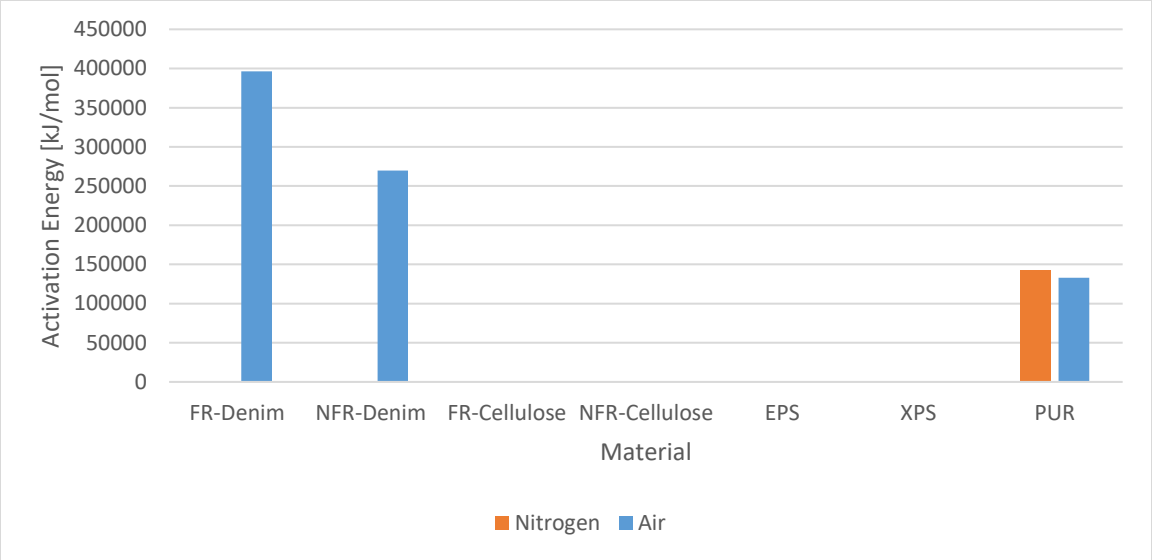

Figure 3.39: Activation energy of 3rd step reaction from TGA results in air and nitrogen environments

3.4 X-Ray Diffraction

X-ray diffraction (XRD) is a technique primarily used to identify compounds within various materials, based on the intensity of diffracted x-rays collected at varying incident beam angles resulting in a spectral pattern. Numerous compounds have been characterized, and can thus be identified based off of these patterns. Typically, this technique works best with crystalline materials, as the structure is more periodic and uniform, resulting in better, sharper spectral peaks. If the material is amorphous, the x-rays will be scattered more randomly and thus result in a wider, more rounded peak. Because of this effect, the exact compounds in the material can be more difficult to ascertain. As with many such techniques, a priori information on the material will reduce errors in interpreting spectral patterns.

The motivation for the study was to deduce what flame retardants were present in the various insulation materials. Preliminary results had shown that peaks of interest were

only in the range of five to sixty degrees. An angle sweep speed of three degrees per minute was chosen, as this gave a sample observation time greater than 0.5 seconds. NFR and FR samples of denim and cellulose were scanned, in order to compare the differences in XRD patterns. Peaks or features identified in FR samples not present in NFR samples may be attributed to the presence of flame retardants.

3.4.1 Key Results

The initial peak patterns of the NFR/FR denim, NFR/FR cellulose, XPS, and two types of PUR can be seen in Figures 3.40-3.43. The two types of PUR had different flame retardants in them, an unknown flame retardant in the Dow Great Stuff Foam and SaFRon 6605 made by ICL Industrial Products. The software that was used, Jade, is primarily used with powders and highly crystalline materials. Since our materials were primarily semi-crystalline and polymeric, almost no hits were found. Also, due to the polymeric nature of the PUR, no discrepancy could be made between the two foams. A similar issue was encountered for the XPS, which led to the decision to not scan EPS.

The cellulosic materials had sharper peaks, and the software was able to determine that mascagnite, commonly known as ammonium sulfate, was used in the FR denim and cellulose. The peaks attributed to mascagnite occur at 20.49, 22.6, 29.4, 33.87, and 38.85 degrees. This compound increases the amount of residue and char during combustion, and helps lower temperatures during combustion as well. Zinc sulfate hydroxide hydrate was found to contribute to the peaks at 12.32 and 24.61 degrees in the FR-cellulose.

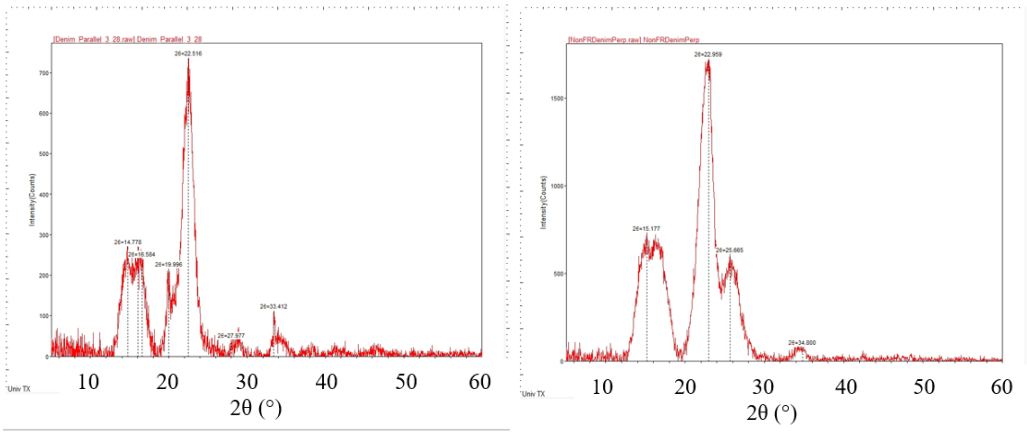

Figures 3.40: XRD curves for FR-denim (left) and NFR-denim (right)

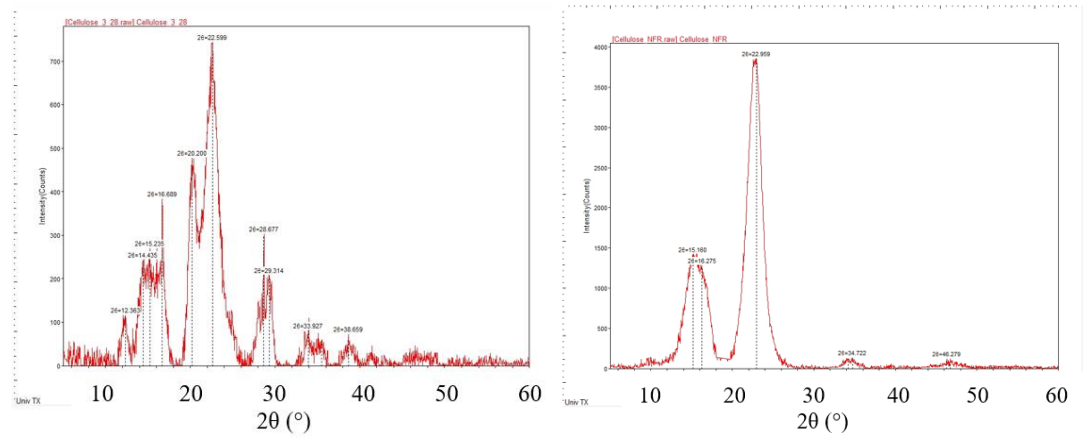

Figures 3.41: XRD curves for FR-cellulose (left) and NFR-cellulose (right)

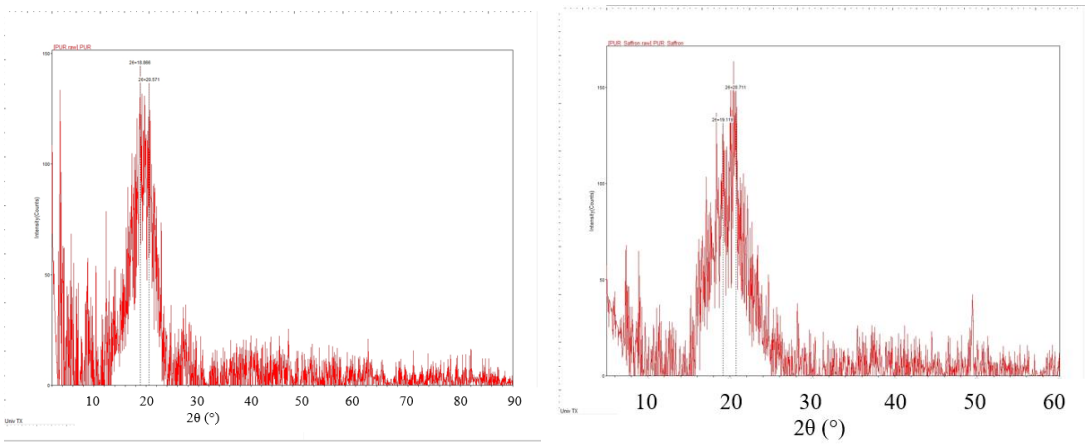

Figures 3.42: XRD curves for PUR (left) and PUR with SaFRron 6605

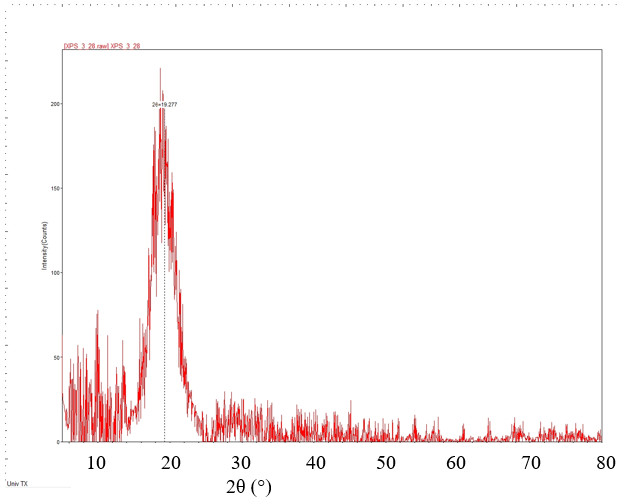

Figure 3.43: XRD curve for XPS

In order to better determine the source of the other peaks found in the cellulosic materials, subsequent testing included varying the orientation of the materials, randomizing the areas examined, and sweeping the x-ray angles at different rates. Changing the orientation of the fibers changed the peak magnitude, where the fibers perpendicular to the x-ray beams showed a higher intensity, seen in Figure 3.44. However, the trend remained

similar for not only the orientation changes, but for the randomization and changing angle rates as well.

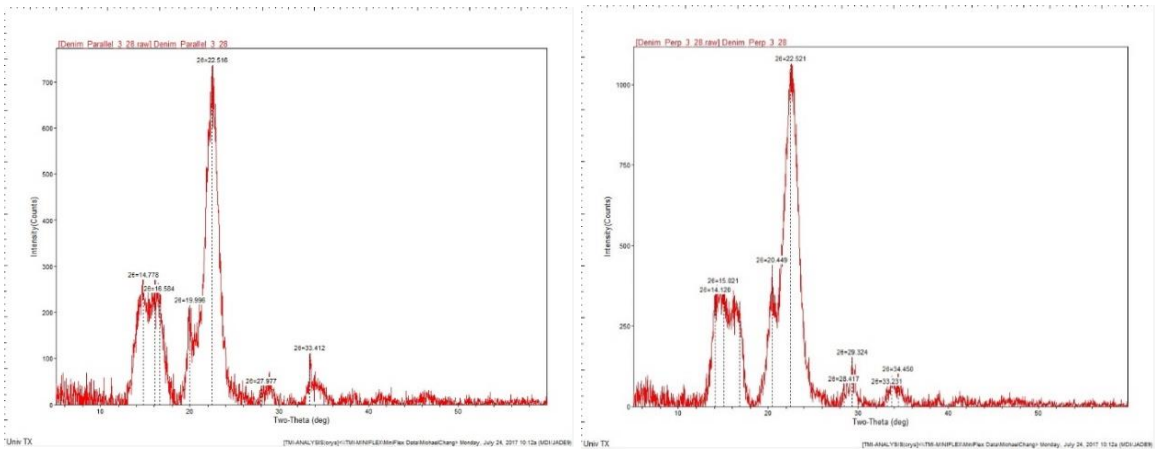

Figure 3.44: XRD comparison of FR-denim in parallel (left) and perpendicular (right) orientations

Literature searches were performed in order to identify common compounds found in these materials, Figure 3.45. The two large peaks found near 15 degrees and 22 degrees, as well as the small peak near 35 degrees in the denim and cellulose can be attributed to the bleached cellulose compound, as found by Rayung [35]. The peak at 25 degrees found in the FR-denim can be attributed to indigo, as shown by Klimovich [36]. The hypothesis was made that the flame retardant in the denim should be attributed to one of the peaks at 20 and 29 degrees, and the cellulose peaks of 12, 20, 29, and 39 degrees. However, no known flame retardants in its crystalline form were found to produce those peaks.

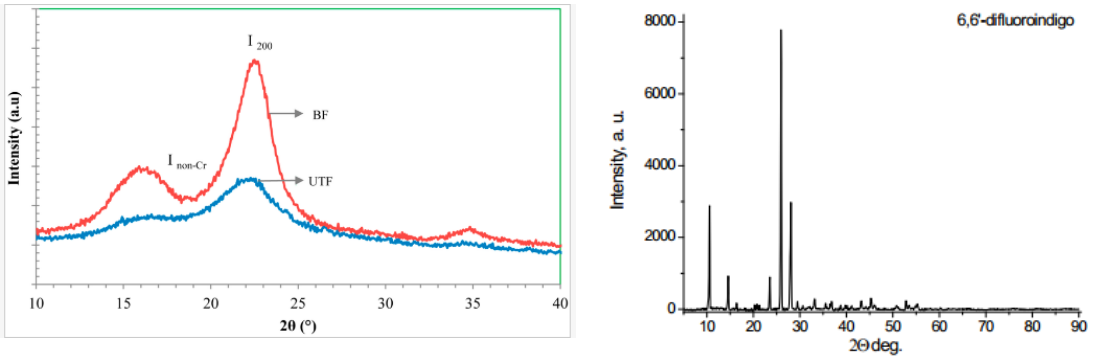

Figure 3.45: XRD curves for bleached cellulose [35] (left) and indigo [36] (right)

The flame retardant present in the denim and cellulose was believed to be boric acid, due to the green flame produced when ignited. Ullah et al. showed an interesting methodology to find certain elements in XRD results, when boric acid was used on an intumescent fire-retardant coating on steel [37]. They heated up the steel with a bunsen burner, recorded the temperatures, and analyzed the char for chemical makeup. From the char, they saw that the boric acid had broken up into boron oxide and sassolite (the mineral acid of boric acid), and then the boron oxide had reacted to form borophosphate. The peaks were highly crystalline, and the chemical makeup was evident. Because it was believed that the flame retardant compound in our materials was boric acid, an attempt was made to replicate the experiment. The denim and cellulose were allowed to char in an oven at comparable temperatures, between 300 °C – 400 °C degrees, as well as between the melting and boiling points of 170 °C to 300 °C degrees. Unfortunately, after heating up the materials, the cellulosic peaks simply began showing more amorphous behavior, possibly outweighing the effects of the flame retardant degradation. A method to separate the materials from the compounds was necessary.

The next method essentially involved boiling the materials in water, until the liquid changed to a green liquid and a red liquid for the denim and cellulose, respectively, seen in Figure 3.46. The material was then taken out of the Pyrex beakers, and further boiled down in aluminum pans until it had become a solid, Figure 3.47. This solid was scraped off of the pans, crushed into a powder, and then run in the XRD, where the peak pattern can be seen in Figure 3.48. The peak associated with the borane sulfide occurs at 14.50 and 16.73 degrees. It should be noted that the peaks obtained through this method show much greater crystalline behavior, compared to simply using the fabric by itself. The inference can be made that the boron atoms were obtained from the boric acid and the sulfide came from the ammonium sulfate.

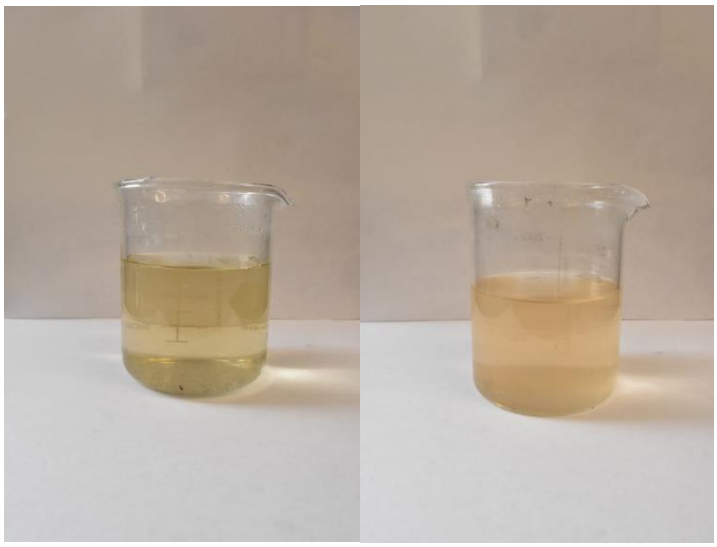

Figure 3.46: Liquid after boiling the FR-denim (left) and FR-cellulose (right)

Figure 3.47: Powder residue after dehydrating the liquid from the FR-denim (left) and FR-cellulose (right)

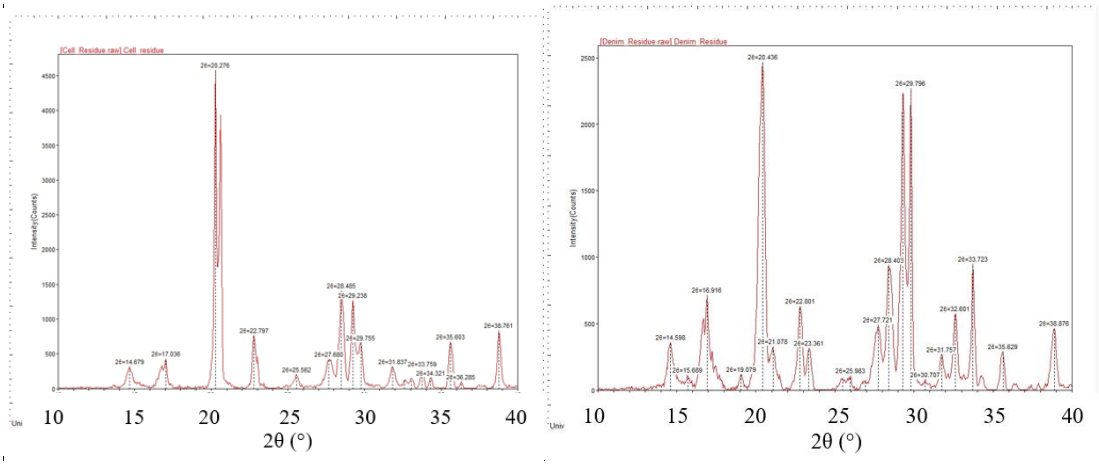

Figure 3.48: XRD curves of a) FR-cellulose residue b) FR-denim residue

Chapter 4 Conclusions

Research up until this point has not characterized the ignition problem of insulating materials commonly found in the attic space. In order to address this issue, an experimental apparatus was built to characterize the ignition parameter space where ignition and extinction occur due to an ember. The effects of air flow at 0 m/s, 2.4 m/s, and 4.8 m/s, were investigated. Geometrical effects, as well as the effects of having flame retardants were also explored. The five insulations that were tested were XPS, EPS, PUR, FR-denim, and FR-cellulose, where the denim and cellulose had NFR counterparts tested as well.

Flaming ignition was found to occur for denim at 2.4 m/s and 4.8 m/s, as well as for cellulose at 4.8 m/s. A phenomenon known as flash flaming, where small wisps of flames were produced that did not consume the fuel bed, appeared on XPS, EPS, and PUR for various configurations at 2.4 m/s and 4.8 m/s. Unsurprisingly, the times to ignition for the flame retardant samples of denim and cellulose were larger than those of the non-flame retardant samples and higher air flows caused ignition to occur quicker. The fragmented ember piles also caused the insulation to ignite faster compared to the single large embers, possibly due to the increased abilities to oxidize and maintain its interfacial temperature between the samples. Furthermore, thermocouples and an IR camera were used to track the ember temperatures as well as the signatures associated with fuel bed ignition.

Methodologies for obtaining thermal properties, such as density, specific heat, and thermal conductivity, were developed. Cone calorimeter tests were also performed. The times to ignition for the NFR samples were lower than the FR samples. Furthermore, the cellulosic materials which showed ignition during the ember tests, also showed lower

ignition times than the XPS and EPS. It is possible that cone calorimeter could be used as a screening tool for the ignition of materials in the future. Similar results in the peak HRR and FIGRA were observed. The effects of relative humidity appeared to affect denim differently than cellulose, where denim was unaffected and cellulose's ignition time decreased with decreasing moisture content. The critical surface temperature for ignition was estimated experimentally; however, more experiments need to be performed and a better model may need to be developed.

TGA was performed for the materials, which highlighted the differences in degradation between FR and NFR materials. The activation energy was found to show similar trends observed in the cone calorimeter and ember ignition results. Furthermore, the application of XRD was explored in order to pinpoint flame retardants occurring in the various insulation materials, though more work needs to be done to refine the process.

By performing these experiments, a better idea of the critical parameter space affecting various fuel beds was found. This helps lay the foundation for finding additional critical parameters and better characterizing the ember and materials, which can then be used for design and analysis models.

4.1 Future Work

Results from this study leaves many questions still unanswered. First and foremost, obtaining NFR samples of the other materials would have greatly helped depict the mechanisms of the flame retardants within the samples. For the ember ignition tests, it would also be desirable to test different mass fluxes on the ignition, in order to find a critical mass flux to ignition. Other shapes of dowels could be manufactured as well, such as the

disks used by Manzello. The critical air flow rate that would cause ignition could also be explored. The model of a drying ember can be improved to include oxidation, and will eventually need to be coupled with the fuel bed to create a full model. A method to determine the heat flux from the ember during testing should also be explored and developed.

The thermal properties of the various insulation should be found using the proposed experiments. Although the thermal property setups worked well for acrylic, care should be taken when measuring the properties of insulation with lower thermal conductivity, as the magnitudes of thermal resistance change. A significant scatter was observed in cone calorimetry measurements. This is likely due to high sensitivity to material characteristics near critical ignition conditions. More tests should be conducted to reduce the effects of the random variation of flame retardants, moisture content, and room humidity. Furthermore, the NFR samples of the other materials should also be tested.

The kinetics obtained from the TGA data should be used to model the pyrolysis and ignition after ember contact. Validation of this model should be performed, as well as a replication of the ember experiment using a controlled heat flux generator (e.g. cartridge heater). Finally, all of these results should be tied back to the cone calorimeter results for comparison at relevant heat fluxes.

Appendix A: Ember Ignition Procedure

Dowel Dimensions:

1) Large Ember Dimension = 1.9 inches
    a. Make sure large ember mesh is inside mesh basket for tests
2) Small Ember Dimension = 3/8 inch
    a. # of Small Embers to be Used for Tests: 5
3) Ensure that large embers have been in Oven at 105 °C for at least an hour before testing

Fuel Bed Prep:

1) NFR Denim: Use about 3.2 g
    a. Needs to be shredded and poofed with brush
2) FR-Cellulose/NFR Cellulose: Use about 3.9 g
3) FR-Denim: Cut half circles to fit wood;
    a. Use an inch of material (In package: comes in 1.8 inch thickness, so need to break it up)

Air Flow Chamber (Before Testing):

1) Turn Graphtek on; Turn Power Source on (Gray Box with fan); Turn on Variac (Gray Knob Thing)
2) Check the voltage of the pressure transducer with the fuel bed NOT inside of the chamber:
    a. 4 mps: 3.23 Volts
    b. 8 mps: 5.5 volts
3) Place Fuel Bed inside of air flow chamber and push the three thermocouples into place
    a. If doing small ember test, make sure mesh chute is attached to top lid
4) Place Chamber lid on top of box, and secure using two Green Unistrut
    a. Make sure lid hole is centered on the center of the fuel bed

Furnace Procedure:

1) Turn Dial on Furnace to High (Between 4 and 5) initially, and adjust accordingly as temperature approaches 420 °C
    a. I've obtained good steady temperature of 420 °C at a dial position of 2.5
2) Turn on Air Flow to 22 SCFH once the furnace starts getting hotter
3) Turn on LabVIEW to monitor Furnace Temperature
    a. Dev1/ai74 = Furnace Temperature

    b. Dev1/ai11:13 = Fuel Thermocouples
4) For small ember tests, push ember into furnace until line is just outside of furnace
    a. Leave inside furnace until you can see all embers glowing (~200 secs)
5) For large ember tests, push ember into furnace until line is ½ inch outside of furnace
    a. Leave inside furnace until you can see ember glowing (~200 secs)

During Testing

1) Open FLIR Tools+ and ensure temperature range is from 0-650 °C
2) Start Recording on DSLR
3) Turn on Variac and allow for at least 20 seconds of runtime before placing ember on Fuel Bed
    a. Make sure you're wearing respirator at this time
4) Ensure naming of file is correct on FLIR and LabVIEW; Simultaneously start recording on both
5) Large Ember: Take ember out of basket using tweezers and place ember through lid's hole onto fuel bed, centered below the lid's hole
6) Small Ember: Angle basket above hole, and tap gently so that all embers roll into chute and onto fuel bed
    a. Make sure chute is pressed tight enough on fuel bed; If it is not, some embers may escape during testing
7) Once flame occurs, turn off the variac and press the foil sheet over the flame to extinguish
8) Clean back window with Windex and front IR transmissive window with a wet paper towel

Quick Checklist:

Prior to testing:

- ✓ Machined Embers Conditioned in Oven
- ✓ Checked velocity of chamber at least once during the day
- ✓ Fuel bed inside of chamber with thermocouples, lid on top with green Unistrut
- ✓ Furnace temperature at 420 °C

During testing:

- ✓ DSLR, LabVIEW, FLIR all recording
- ✓ Variac on
- ✓ Facemask on
- ✓ Embers basically all glowing red
- ✓ Place Ember on Fuelbed
- ✓ Once flame occurs, turn off Variac and extinguish flame

Appendix B: Polyurethane (PUR) sample production

The PUR spray foam was initially created using two different methods. The first method involved simply spraying a one inch layer of foam and letting it expand. This created large gaps and voids and made an inhomogeneous type of foam, as seen in Figure B1a.

The second method involved using a layer of Plexiglas to sandwich the foam as it was expanding, hoping to shrink the voids that were appearing. A similar issue occurred, where the resulting foam was undesirable, B1b.

Figure B1: a) Thick layered PUR b) Flattened PUR

It was found that the components used to create the PUR foam react best when there is a plethora of moisture available. Therefore, subsequent attempts involved adding thinner layers of foam, spraying water over the layers, waiting in between adding layers, or a combination of all of the above. The best method found was laying out a layer of aluminum foil, so the foam would not stick, and spraying it with an initial coating of water. A 1.5 cm layer of foam was then sprayed, and was misted with water immediately after. The foam was allowed to cure for 10 minutes, before another 1.5 cm layer was sprayed, misted, and

allowed to cure. The pores are much smaller, and the foam is more homogenous using this technique, as seen in Figure B2.

Figure B2: Properly made PUR

Appendix C: Image Processing in MatLAB

Image Processing Toolbox in MatLAB was used to measure the areas of each fragmented ember, and was to be used to make the process more automated. Figure C1 shows the before and after pictures of the processed image, where the white space in the processed image is what is used to calculate the area. The shadows of the embers were filtered out using thresholds, but in the future, better quality images should be used.

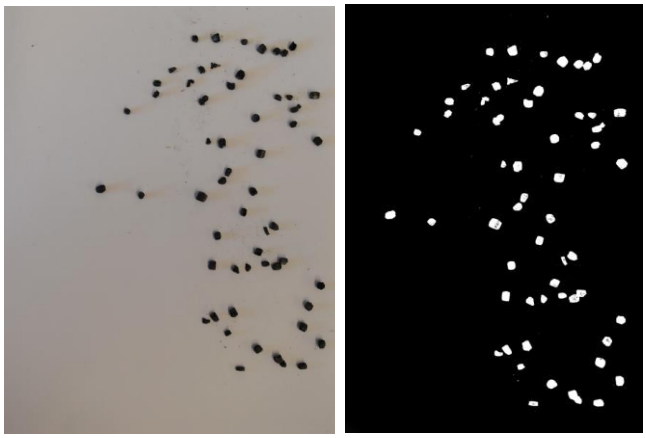

Figure C1: Image of embers (left) and image of processed embers (right)

It can be seen in Figure C2 that the average area of the embers falls between 15-25 mm^2.

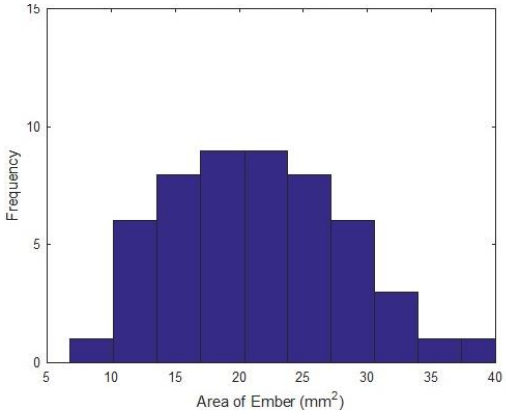

Figure C2: Histogram of the areas of the embers

MatLAB code used to process images:

```
I2 = imread('ember.jpg');
imshow(I2)
I = imcomplement(I2);

level = graythresh(I);
bw = im2bw(I,level);
bw = bwareaopen(bw, 50);
imshow(bw)

cc = bwconncomp(bw, 4)
cc.NumObjects

graindata = regionprops(cc, 'basic')
grain_areas = [graindata.Area];
act_grain_areas=60322.46/17584384*grain_areas;

for i=1:54
if act_grain_areas(i)<1
        act_grain_areas(i)=[];
end
end

nbins = 13;
figure, hist(act_grain_areas, nbins)
title('Histogram of Ember Area');

% axis([5,40,0,15])
>> xlabel('Area of Ember (mm^2)')
>> ylabel('Frequency')
```

Appendix D: Angle XPS Tests

Tests were performed to see the effects of having embers pile up in the corner of an attic. The idea was to see if flash flaming can propagate flaming vertically, as would be done in the corner of an attic crevice. Embers were dropped where the two pieces of XPS meet, while a fan at the same height with an average velocity of 2.4 m/s was used to blow on the ember during testing. The setup can be seen in Figure D1, and it should be noted that the char marks on the top piece of wood came from a prior ember test.

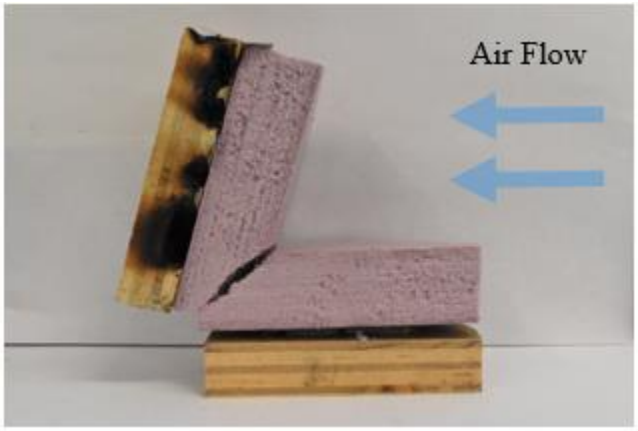

Figure D1: Example of XPS sample, pre-ember drop

During the three tests that were performed, flash flaming was not evident during any of the tests. Furthermore, the ember typically sank down to the wood on the lower portion of the XPS, and so moving the ember to the top piece of XPS was attempted mid-tests, as seen at 10s in Figure D2. Conditions to either entrain the volatilized gases or to change the direction and magnitude of the air flow should be attempted in order to promote flash flaming for future testing.

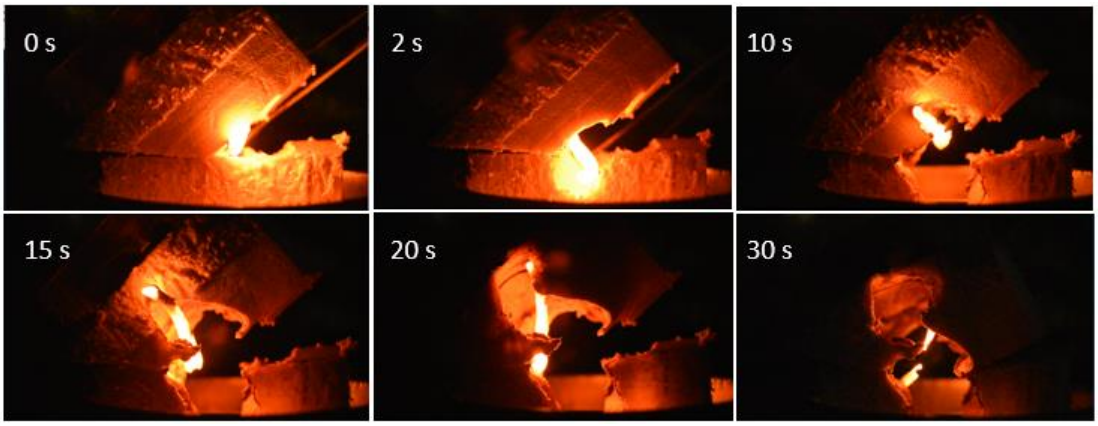

Figure D2: Progression of ember drop experiment

Appendix E: Drying Process of an Ember

The drying process of an ember in a radiative environment was modeled using FEniCS, a partial differential equation solver platform. Initially, the model was strictly 1-D and only tracked T(x,t). Eventually, a heat and mass transfer model developed by Luikov, and refined by Whitaker [38, 39] was used to track the simultaneous temperature and moisture content in the dowel's 3-D cylindrical geometry. The parameters used were taken from Kulasiri [40], where c_p is the specific heat of the dowel, ρ_o is the original density of the dowel, k is the thermal conductivity of the dowel, T is the temperature of the dowel, R is the specific enthalpy of the water's phase change, ε is the phase change coefficient, m is the moisture content of the dowel, a_m is the total diffusion coefficient, δ is the thermogradient coefficient, and h_m is the mass transfer coefficient.

$$c_p \rho_o \frac{\partial T}{\partial t} = k\nabla^2 T + R\varepsilon_{mc} \frac{\partial m}{\partial t} \tag{E.1}$$

$$a_m \nabla^2 m + a_m \delta \nabla^2 T = \frac{\partial m}{\partial t} \tag{E.2}$$

Initial conditions:

$$T(r, 0) = 25$$

$$m(r, 0) = 0.15 \tag{E.3}$$

Boundary conditions:

$$As\ r\ \rightarrow \infty;\ T = \ 450, m = 0 \tag{E.4}$$

$$\left(k\frac{\partial T}{\partial n}\right) = h\left(T_{amb} - T_{surf}\right) + \sigma\varepsilon(T_{amb}^4 - T_{surf}^4) \quad \text{(E.5)}$$

$$D\frac{\partial m}{\partial n} = h_m(m_{surf} - m_{amb}) \quad \text{(E.6)}$$

Where n is a unit normal vector perpendicular to the surface

Table E.1: Properties used in FEniCS model

Property	**Value**
c_p	$2500\frac{J}{kg*K}$
ρ_o	$350\frac{kg}{m^3}$
k	$1.41\frac{W}{m*K}$
R	$2{,}257{,}000\frac{J}{kg}$
ε_{mc}	0.5
a_m	$2.8*10^{-10}\frac{m^2}{s}$
δ	$1*10^{-2}\,K^{-1}$
ε	1
D	$1.45*10^{-9}\frac{m^2}{s}$
h_m	$0.0022\frac{m}{s}$

In order to use FEniCS, the previous equations needed to be transformed into its variational form, where the left side of the equation, a, is written as a bilinear function, the right side, L, is some linear vector, u is a test function, and v is a trial function. The transformed set of equations are represented in Eq. E.8 and E.9.

$$a(u, v) = L(v) \tag{E.7}$$

The variational forms of these equations can be seen below.

$$\alpha \left[\int_{\Omega} (k \nabla T_{k+1}) \cdot \nabla v \, dx + \int_{\partial \Omega} \varepsilon \sigma T_{k+1}^4 v \, ds \right] + \int_{\Omega} (\rho_0 c T_{k+1} + R \varepsilon m_k) N v \, dx$$

$$= (\alpha - 1) \left[\int_{\Omega} (k \nabla T_k) \cdot \nabla v \, dx + \int_{\partial \Omega} \varepsilon \sigma T_k^4 v \, ds \right] + \int_{\Omega} (\rho_0 c T_k + R \varepsilon m_{k+1}) N v \, dx +$$

$$\int_{\partial \Omega} \varepsilon \sigma T_c^4 v \, ds \tag{E.8}$$

$$\alpha \left[\int_{\Omega} (a_m \delta \nabla T_{k+1}) \cdot \nabla v \, dx + \int_{\Omega} (a_m \nabla m_{k+1}) \cdot \nabla v \, dx + \int_{\partial \Omega} \frac{a_m \delta}{k} \varepsilon \sigma T_{k+1}^4 v \, ds + \right.$$

$$\left. \int_{\partial \Omega} \frac{a_m h_m (m_{k+1} - m_o)}{D} v \, ds \right] + \int_{\Omega} (N m_{k+1}) v \, dx = (\alpha - 1) \left[\int_{\Omega} (a_m \delta \nabla T_k) \cdot \nabla v \, dx + \right.$$

$$\left. \int_{\Omega} (a_m \nabla m_k) \cdot \nabla v \, dx + \int_{\partial \Omega} \frac{a_m \delta}{k} \varepsilon \sigma T_k^4 v \, ds + \int_{\partial \Omega} \frac{a_m h_m (m_k - m_o)}{D} v \, ds \right] +$$

$$\int_{\Omega} (N m_k) v \, dx + \int_{\partial \Omega} \frac{a_m \delta}{k} \varepsilon \sigma T_c^4 v \, ds \tag{E.9}$$

Gmsh was used to create the geometry of the dowel, while ParaView was used to visualize the results. The results of the temperature evolution can be seen in Figure E.1 and E.2, and can be compared to the thermocouple measurements of the ember obtained in section 2.2. The trends of the temperature evolution are similar, as both results show the ember near 400 °C around 150 seconds. However, the FeNIcs results do not show the trend at 100 °C where the experimental ember is drying, and thus has a higher temperature for

most of the test. Furthermore, kinetics are not accounted for, and therefore the temperature of the FeNIcs ember does not ever go above the furnace temperature.

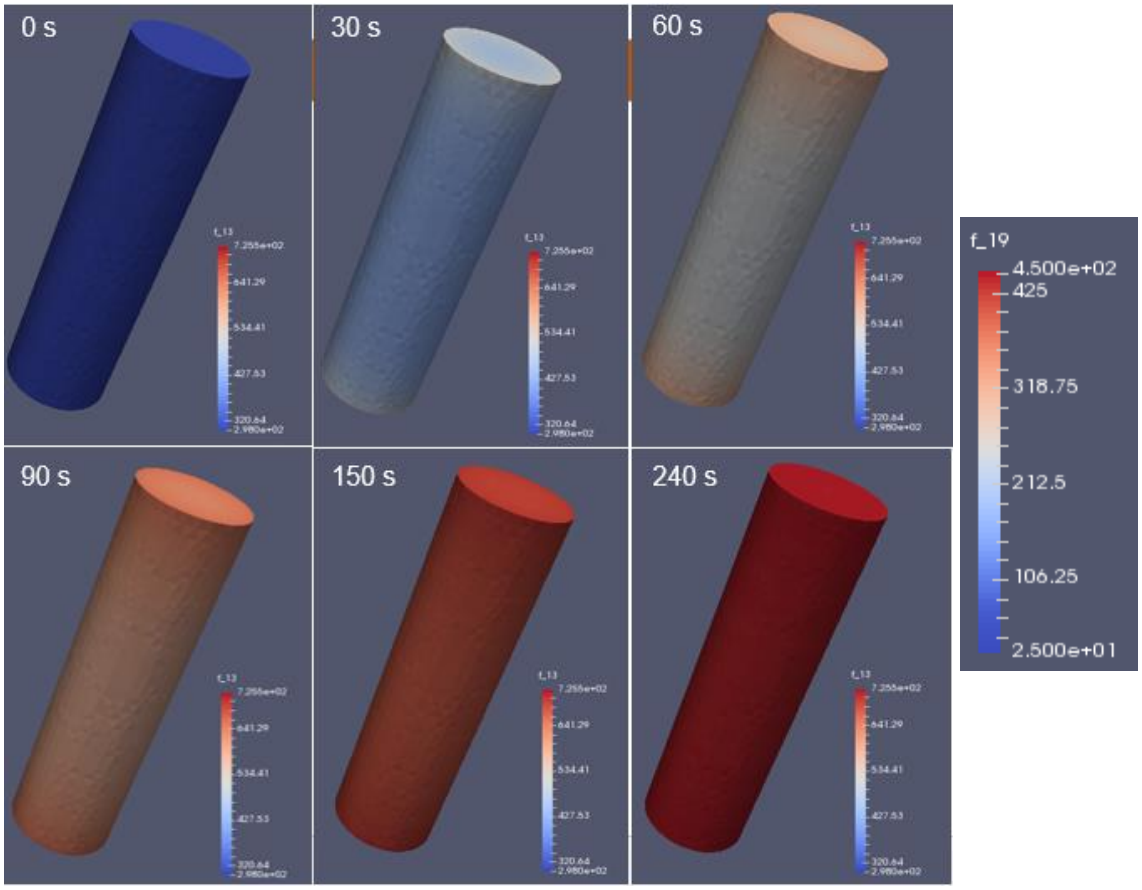

Figure E.1: Temperature progression of an ember in a radiative environment modeled in FeNIcs

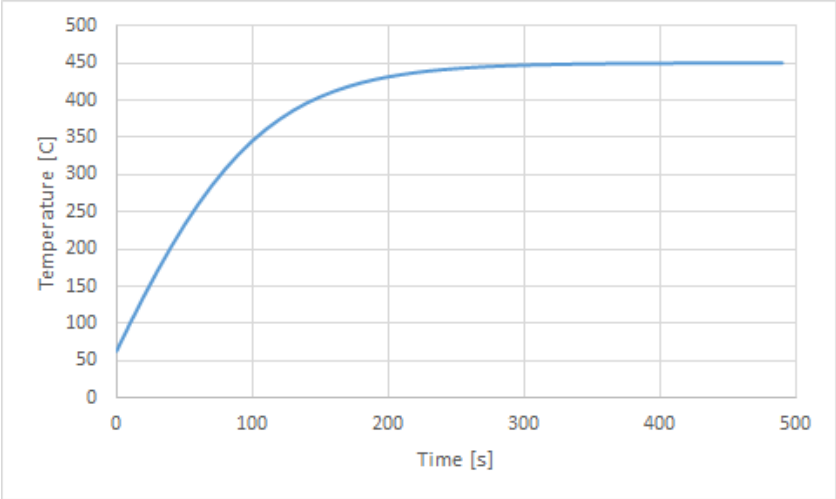

Figure E.2: Average temperature of ember modeled in FEniCS

The coupled moisture content appears not to dry as rapidly as the experimental ember, seen in Figures E.3 and E.4, and also does not show a drying period when the ember is near 100 °C.

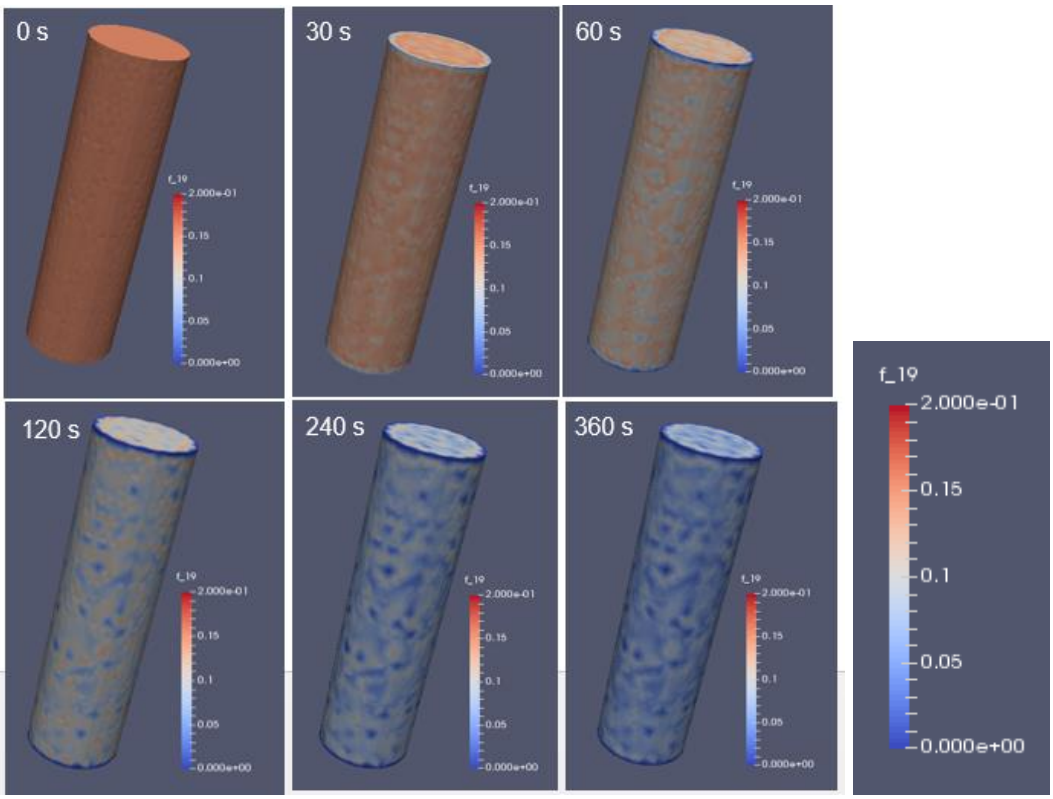

Figure E.3: Moisture content progression of an ember in a radiative environment modeled in FeNIcs

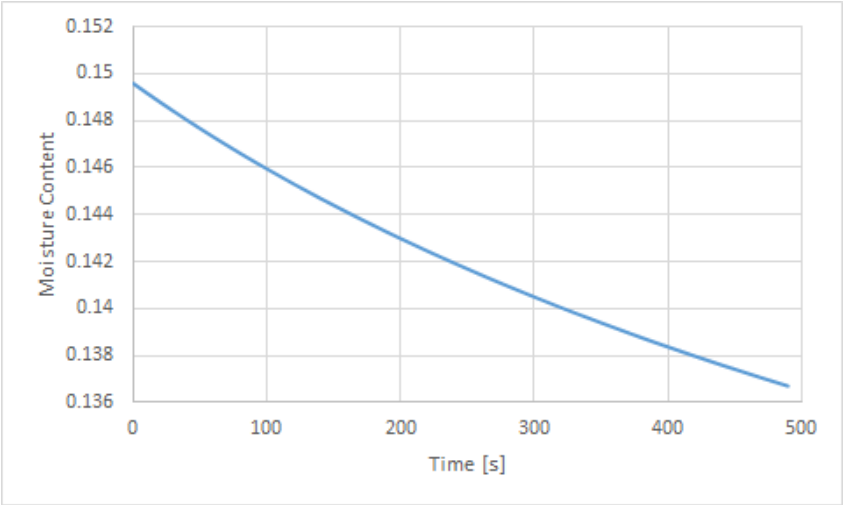

Figure E.4: Average moisture content of ember modeled in FEniCS

There appears to be an issue with the model that causes a ring of high moisture content to appear and stagnate inside of the ember, as seen in Figure E.5. The surface is able to lose its moisture to the environment, but the moisture on the inside of the dowel builds up near that ring, and the process of drying slows down as seen above. Adjustments need to be made in the future to address this issue.

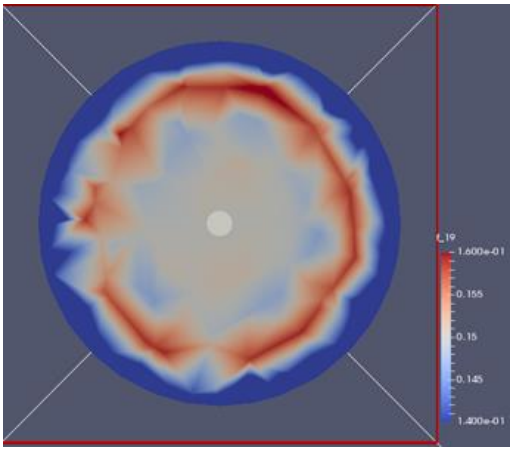

Figure E.5: Cross-section of ember center during the drying process

Appendix F: FEniCS Model of Ember

```
from dolfin import *
import numpy as np

# Create mesh
mesh = Mesh("./cylinder.xml")

# Define subdomains
boundaries  = FacetFunction("uint", mesh)
domains     = CellFunction("uint", mesh)

#Define boundaries - radius & length
class Omega1(SubDomain):
  def inside(self, x, on_boundary):
     tol = 10**(-5)
     if (x[0]**2+x[1]**2)**(0.5) < 0.010+tol and x[2]< 0.070+tol and x[2] > -tol:
        return True
     else:
        return False

class Perimeter(SubDomain):
        def inside(self,x,on_boundary):
                tol=10**(-5)
                r=(x[0]**2+x[1]**2)**(0.5)
                return on_boundary and (r < 0.010+tol or r> 0.010 -tol)

class Caps(SubDomain):
        def inside(self,x,on_boundary):
                tol=10**(-5)
                return on_boundary and ((abs(x[2])< tol) or (abs(x[2]-0.070)< tol))

omega1 = Omega1()
perimeter= Perimeter()
caps=Caps()

domains.set_all(0)

omega1.mark(domains, 1)
perimeter.mark(boundaries,2)
caps.mark(boundaries,3)

dx = Measure("dx")[domains]
ds = Measure("ds")[boundaries]
```

```
def q(u):
  return (u)*(u)*(u)*(u)

# Define thermal properties
kmult = 1.41 #W/m*K
k00 = 1.0 * kmult
k01 = 0.0 * kmult
k11 = 1.0 * kmult
k = as_matrix(((k00,k01),(k01,k11)))
h = 0.0
cp = 2500 #J/kg*K
rho=350 #kg/m^3
sig=5.670367*10**(-8)          #W/(m^2*K^4)
rad_eps=1
mc_eps=1
hm=0.0022                  #m/s
diff=1.45*10**(-9)                 #m^2/s
hfg=2257000 #J/kg
am=2.8*10**(-10) #m^2/s
delta=1*10**(-1)

# Define function spaces and mixed (product) space
CG  = FunctionSpace(mesh, "CG", 1)
CG2 = CG*CG
tempfunction=CG

#Time Dependence
initial_condition_temp = Expression("298.0")
initial_condition_mc = Expression("0.15")
u_k = Function(CG)
u_k = interpolate(initial_condition_temp, CG)
m_k = Function(CG)
m_k = interpolate(initial_condition_mc, CG)
dt = 10
time = dt
time_max = 50*dt
nu = 1.0/dt
beta = nu*rho*cp
alpha = 0.5

# Define source functions
f = Expression("0.0") #driving function/heat gen
g3 = Expression("283.0")       #Dirchlet Fixed Wall Temp
```

```
uc = Expression("298.0")       #convective temperature
mc = Expression("0.0")                  #Environmental Moisture Content
one=Expression("1.0")

# Define trial and test functions
(u,m) = TrialFunctions(CG2)
(v,n) = TestFunctions(CG2)
u_ = Function(CG2) # the most recently computed solution

RHS1 = alpha*((inner(kmult*grad(u),grad(v)))*dx + rad_eps*sig*q(u)*v*ds) +
beta*u*v*dx + hfg*mc_eps*m*nu*v*dx
RHS2 = alpha*((inner(am*delta*grad(u),grad(n)))*dx + (inner(am*grad(m),grad(n)))*dx
+ am*delta/kmult*rad_eps*sig*q(u)*n*ds + am*hm*(m-mc)/(diff*rho)*n*ds) +
nu*m*n*dx
LHS1 = (alpha-1.0)*((inner(kmult*grad(u_k),grad(v)))*dx + sig*rad_eps*q(u_k)*v*ds)
+ f*v*dx + rad_eps*sig*q(uc)*v*ds + beta*u_k*v*dx + hfg*mc_eps*m_k*nu*v*dx
LHS2 = (alpha-1.0)*((inner(am*delta*grad(u_k),grad(n)))*dx +
(inner(am*grad(m_k),grad(n)))*dx + am*delta/kmult*rad_eps*sig*q(u_k)*n*ds +
am*hm*(m_k-mc)/(diff*rho)*n*ds) + nu*m_k*n*dx +
am*delta/kmult*rad_eps*sig*q(uc)*n*ds
a1 = RHS1 + RHS2 - LHS1 - LHS2

a1 = action(a1,u_)

bc3 = DirichletBC(CG2.sub(0),g3,boundaries,3)
bc2 = DirichletBC(CG2.sub(1),g1,boundaries,3)
bcs = [bc3, bc2]

# Compute solution and save
ufile1 = File("time_tutorial_results/temperature.pvd")
ufile1 << u_k
ufile2 = File("time_tutorial_results/moisturecont.pvd")
ufile2 << m_k
ufile3 = File("time_tutorial_results/mcint.xml")
ufile4 = File("time_tutorial_results/tint.xml")

f = Function(CG)
n = CG.dim()
f_values = np.zeros(n)
f.vector()[:] = f_values

f2 = Function(CG)
f2_values = np.zeros(n)
f2.vector()[:] = f2_values
```

```
tempfunction=interpolate(one, CG)
normalization=assemble(tempfunction*dx)

i=0
#Transient loop solver
while (time <= time_max):

        set_log_level(PROGRESS)
        solve(a1 == 0, u_, None, solver_parameters={"newton_solver":
{"maximum_iterations": 50, "relative_tolerance": 1e-5,"absolute_tolerance": 1e-5}})

        (j,k) = u_.split()
        assign(u_k,j)
        assign(m_k,k)
        f.vector()[i] = assemble(m_k*dx)/normalization
        f2.vector()[i] = assemble(u_k*dx)/normalization
        i=i+1
        time += dt
        ufile1 << u_k
        ufile2 << m_k
        ufile3 << f.vector()
        ufile4 << f2.vector()
```

Appendix G: Thermal Conductivity Inversion Code

```
#!/usr/bin/env python

"""
PyMC simulation to determine a model exponent.

"""

import numpy as np
import pymc as mc
import matplotlib.pyplot as plt
import forward_model

# Data
data = np.genfromtxt('ExperimentalData.csv', delimiter=',', names=True)

# Set data variables
time = data['time']     # times, seconds
T_1a = data['T_1a']     # temperatures at back of exposed board, K

# Priors
theta = mc.Uniform('theta', lower=[0.10], upper=[0.5], value=[0.16])
sigma = mc.Uniform('sigma', lower=[0], upper=[10], value=[1])

# Deterministic node for y_mean from model
@mc.deterministic
def y_mean(theta=theta, inputs=time):

        return forward_model.conduct(theta,inputs)

# Stochastic node set to observed (data)
y_obs = mc.Normal('y_obs', value=T_1a, mu=y_mean,
            tau=sigma**-2, observed=True)

# Generate model
m = mc.MCMC([theta,sigma])

# Configure and run MCMC simulation
m.sample(iter=500, burn=50, thin=10)

# Plot resulting distributions and convergence diagnostics
mc.Matplot.plot(m, format='pdf',
```

```
            path='../Figures',
            common_scale=False)

plt.figure()
plt.plot(T_1a,lw=2,label='Experiment')
#plt.plot(forward_model.conduct(0.125,time),lw=2,label='Prediction')
plt.plot(forward_model.conduct(np.mean(m.trace("theta")[:]),time),lw=2,label='Predictio
n')
plt.legend()
plt.xlabel('Time (s)')
plt.ylabel('Temperature (C)')
plt.show()

# Display results
m.summary()
```

2) Forward Model

```
import numpy as np

def conduct(theta, time):
        k=float(theta)
        rho = 1170
        cp=1470

        #Thermal Properties
        alpha = k/(rho*cp)

                #PDE to be solved is u_xx=u_t
                # BC: @ x=0, T= 100; @ x=1, dT/dx=0
                # IC: @ t=0, T=25

        ubc = np.array([[2,0,0], [1,100,0]])  #First Number: If 1, then dirchlet, if 2, robin;
Second Number: Either Temp or g and h

        #Discretization
        n=5
        t_int=len(time)
        max_time=time[t_int-1]
        deltime=max_time/(t_int-1)
        maxh=0.006085
        delx=maxh/(n-1)

        x=np.linspace(0,maxh,n)
        t=time
```

```
        temp=np.ones((n,t_int))*26
        temp[n-1,:] *=100/26

        # --- Coefficients of the tridiagonal system
        b = (-alpha/2/delx**2)*np.ones((n,1))  #  Super diagonal: coefficients of u(i+1)
        c = b.copy()                           #  Subdiagonal: coefficients of u(i-1)
        a = (1/deltime)*np.ones((n,1)) - (b+c)   #  Main Diagonal: coefficients of u(i)
        c[0] = 0
        b[(n-1)] = 0

        # --- Adjust boundary coefficients
        a[0] = 1/deltime + alpha*(1 + ubc[0,2]*delx)/delx**2
        b[0] = -alpha/delx**2

        #If L has BC of Robin Use this:
        #a[n-1] = 1/deltime + alpha*(1 - ubc[1,2]*delx)/delx**2
        #c[n-1] = -alpha/delx**2

        #If L has BC of Dirchlet, Use This:
        a[n-1]=1
        c[n-1]=0

        # TridiagLU (a,b,c)
        l=len(a)
        e=np.zeros((l,1))
        f=e.copy()
        # --- Elimination phase: compute e and f
        f[0]=a[0]
        for i in range(1,l):
                e[i] = c[i]/f[i-1]
                f[i] = a[i] - e[i]*b[i-1]

        # --- Loop over time steps
        at = (1/deltime + b + c);   #  coefficient of u_i^k

        for k in range(0,t_int-1):
        # --- Update RHS for all equations except those on boundary
                # the c(1:end-1) is being multiplied by the Temp Vector til a point) and
being added throughout
                d1 = np.array([0])
                d1 = np.append(d1,c[1:n-1,0]*temp[0:n-2,k])
                d1 = np.append(d1,0)
                d2 = np.array([0])
                d2 = np.append(d2,at[1:n-1,0]*temp[1:n-1,k])
```

```
                d2 = np.append(d2,0)
                d3 = np.array([0])
                d3 = np.append(d3,b[1:n-1,0]*temp[2:n,k])
                d3 = np.append(d3,0)
                d= -d1+d2-d3

                d[0] = (1/deltime - alpha*(1 + ubc[0,2]*delx)/delx**2)*temp[0,k] +
alpha*temp[1,k]/delx**2 - 2*alpha*ubc[0,1]/delx

                #If L has BC of Robin
                # d[n-1] = (1/deltime - alpha*(1 - ubc[1,2]*delx)/delx**2)*temp[n-1,k] +
alpha*temp[n-2,k]/delx**2 + 2*alpha*ubc[1,1]/delx
                #If L has BC of Dirchlet
                d[n-1] = ubc[1,1]
        # TridiagLUSolve
                d_len=len(d)
                x=np.zeros((d_len,1))
                x[0] = d[0]

                for i in range(1,d_len):
                        x[i] = d[i] - e[i]*x[i-1]

        # --- Backward substitution: solve U*x = y.  y is stored in x to start of loop
                x[d_len-1] = x[d_len-1]/f[d_len-1]
                for i in range(d_len-2,-1,-1):
                        x[i] = (x[i] - b[i]*x[i+1])/f[i]
                temp[:,k+1]=x[:,0]
        return temp[0,:]
```

Appendix H: Peak MLR

The peak mass loss rate of the seven materials can be seen in Figures H1 and H2. The peak MLR is higher for the NFR materials, although there is no clear trend between the different heat fluxes. PUR has the highest peak MLR, whereas the other polymeric materials have similar rates compared to the cellulosic materials.

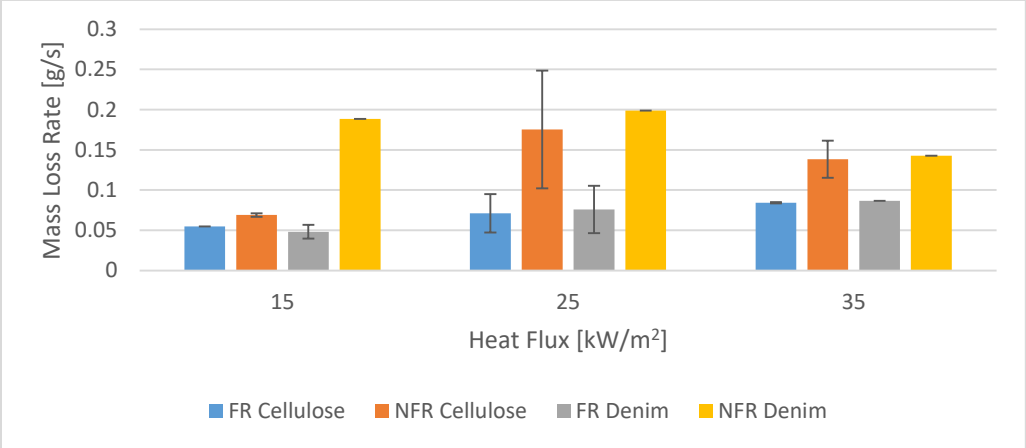

Figure H1: Peak MLR of NFR vs. FR material

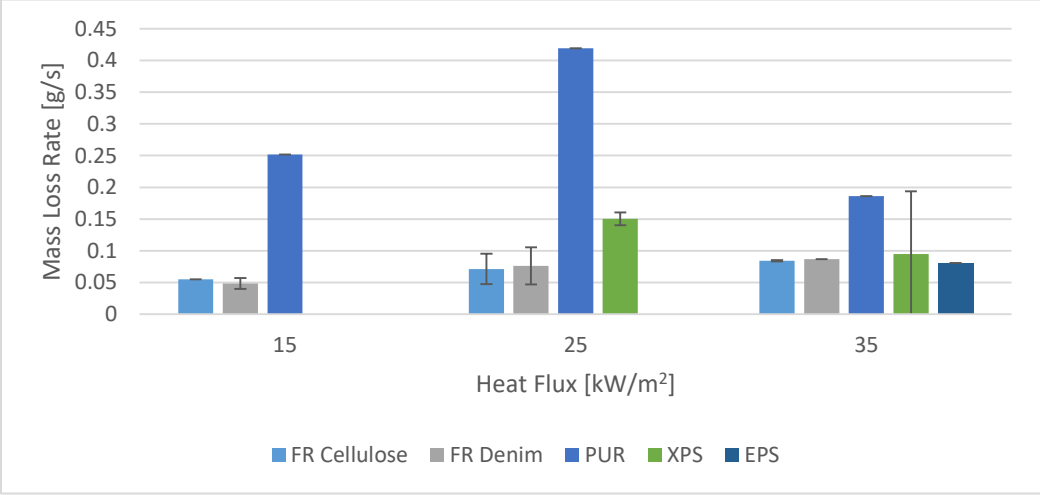

Figure H2: Peak MLR of insulation materials

Appendix I: TGA Curves

1) Curves for Air

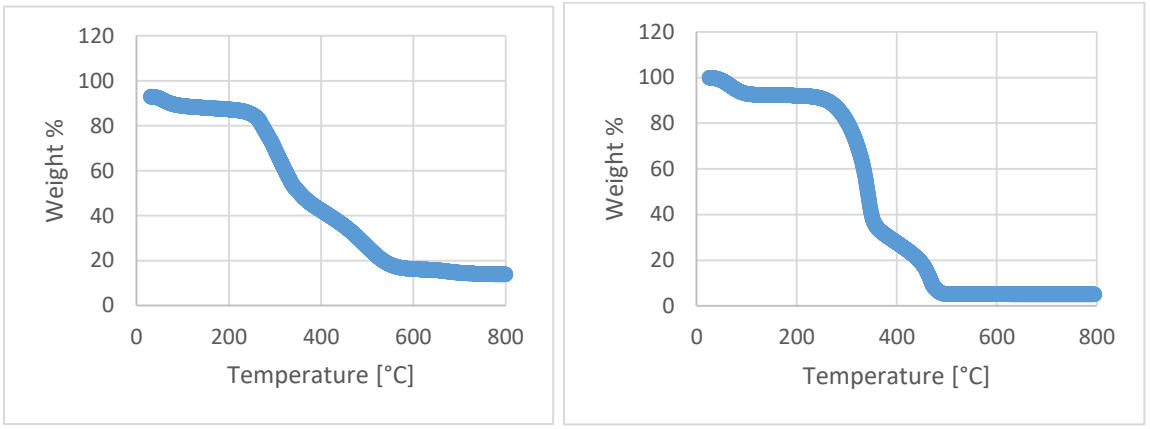

Figure I1: TGA curves of FR-cellulose (left) and NFR-cellulose (right) in air

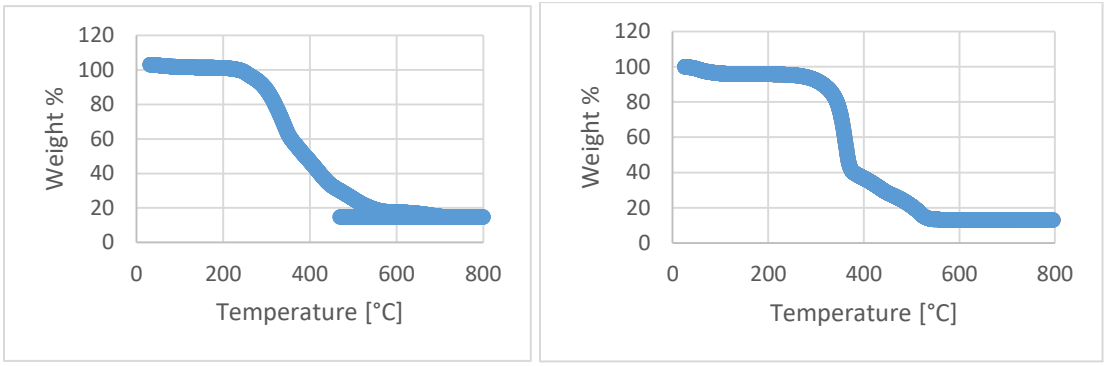

Figure I2: TGA curves of FR-denim (left) and NFR-denim (right) in air

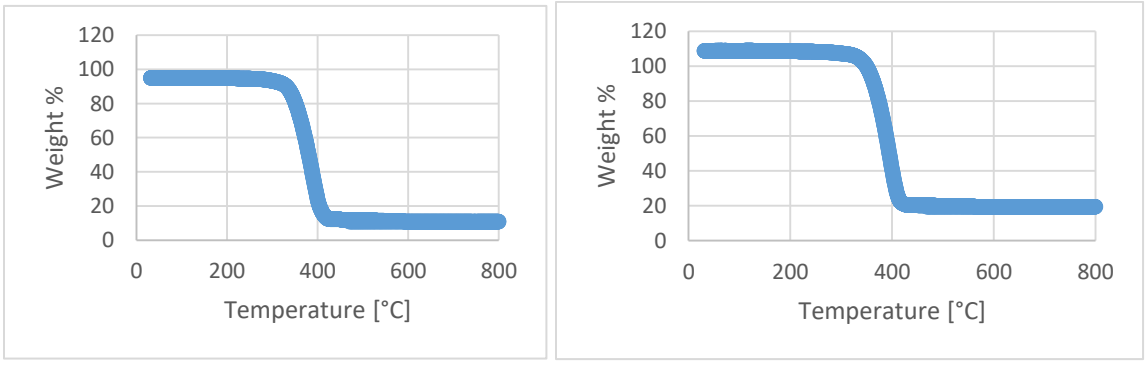

Figure I3: TGA curves of XPS (left) and EPS (right) in air

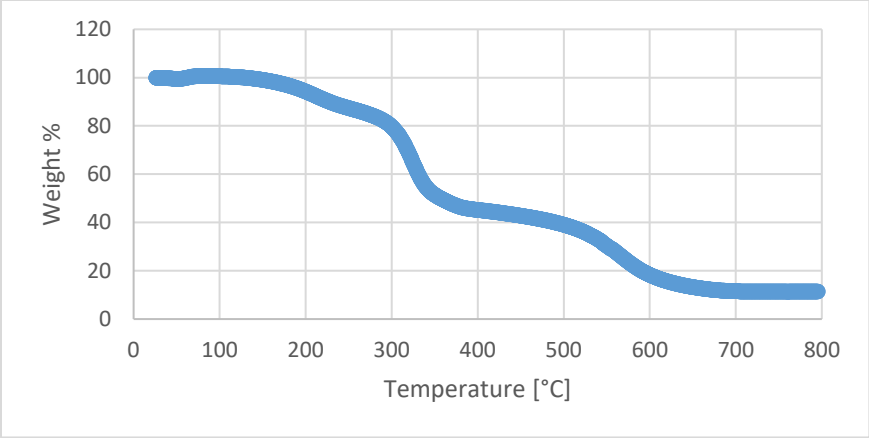

Figure I4: TGA curve of PUR in air

2) Curves for Nitrogen

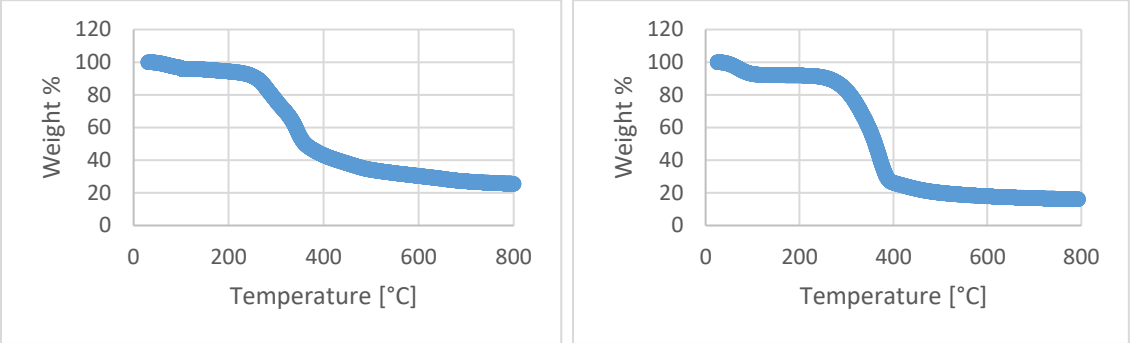

Figure I5: TGA curves of FR-denim (left) and NFR-denim (right) in nitrogen

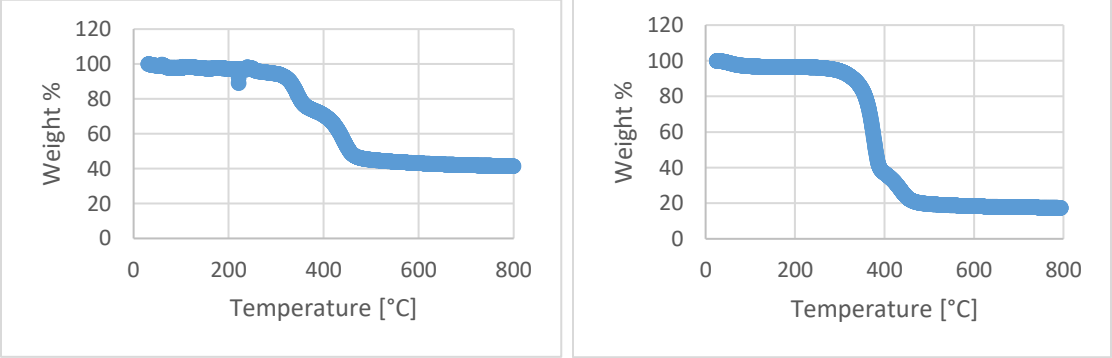

Figure I6: TGA curves of FR-denim (left) and NFR-denim (right) in nitrogen

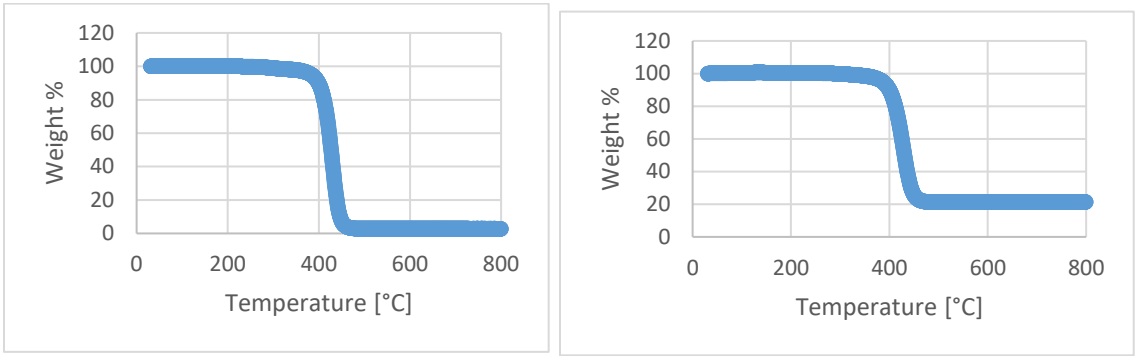

Figure I7: TGA curves of XPS (left) and EPS (right) in nitrogen

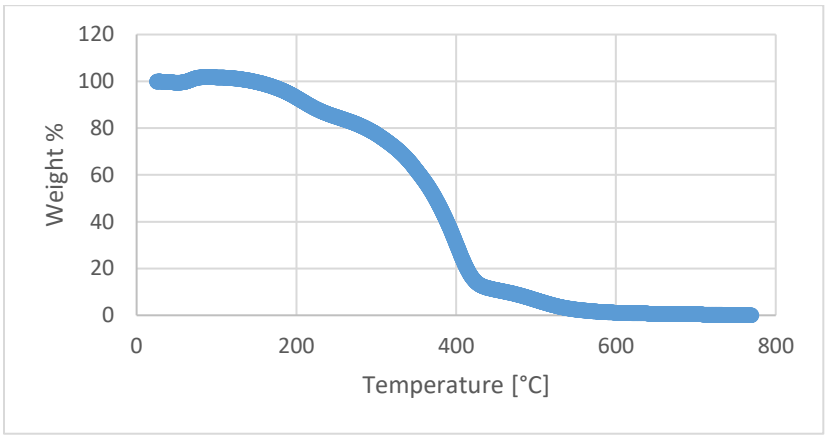

Figure I8: TGA curves of PUR in nitrogen

References

[1] Quarles, Stephen, and Melissa Sindelar. *Wildfire ignition resistant home design (WIRHD) program: Full-scale testing and demonstration final report*. No. 11-14-R. USDA Forest Service-Savannah River, New Ellenton, SC, 2011.

[2] Manzello, Samuel L., John R. Shields, Jiann C. Yang, Yoshihiko Hayashi, and Daisaku Nii. "On the use of a firebrand generator to investigate the ignition of structures in wildland–urban interface (WUI) fires." In *11th international conference on fire science and engineering (INTERFLAM)*, pp. 3-5. 2007.

[3] Manzello, Samuel L., Thomas G. Cleary, John R. Shields, Alexander Maranghides, William Mell, and Jiann C. Yang. "Experimental investigation of firebrands: generation and ignition of fuel beds." *Fire Safety Journal* 43, no. 3 (2008): 226-233.

[4] Manzello, Samuel L., Seul-Hyun Park, and Thomas G. Cleary. "Investigation on the ability of glowing firebrands deposited within crevices to ignite common building materials." *Fire Safety Journal* 44, no. 6 (2009): 894-900.

[5] Manzello, Samuel L., Thomas G. Cleary, John R. Shields, and Jiann C. Yang. "Ignition of mulch and grasses by firebrands in wildland–urban interface fires." *International Journal of Wildland Fire* 15, no. 3 (2006): 427-431.

[6] Urban, James L., Casey D. Zak, and Carlos Fernandez-Pello. "Cellulose spot fire ignition by hot metal particles." *Proceedings of the Combustion Institute*35, no. 3 (2015): 2707-2714.

[7] Wang, Supan, Haixiang Chen, and Naian Liu. "Ignition of expandable polystyrene foam by a hot particle: An experimental and numerical study." *Journal of hazardous materials* 283 (2015): 536-543.

[8] Hadden, Rory M., Sarah Scott, Chris Lautenberger, and A. Carlos Fernandez-Pello. "Ignition of combustible fuel beds by hot particles: an experimental and theoretical study." *Fire technology* 47, no. 2 (2011): 341-355.

[9] Zak, Casey David. *The Effect of Particle Properties on Hot Particle Spot Fire Ignition*. University of California, Berkeley, 2015.

[10] Suuberg, Eric Michael, I. Milosavljevic, and W. D. Lilly. *Behavior of charring materials in simulated fire environments*. US Department of Commerce, National Institute of Standards and Technology, 1994.

[11] "Agricultural Engineering in Development - Drying." *Food and Agriculture Organization of the United Nations*. http://www.fao.org/docrep/t0522e/T0522E08.htm.

[12] Freedman, David, and Persi Diaconis. "On the histogram as a density estimator: L 2 theory." *Zeitschrift für Wahrscheinlichkeitstheorie und verwandte Gebiete* 57, no. 4 (1981): 453-476.

[13] Poespowati, Tri. "An experimental study on autoignition of wood." *Proc World Acad Sci Eng Technol* 30 (2008): 672-675.

[14] Shen, D. K., M. X. Fang, and W. K. Chow. "Ignition of wood-based materials by thermal radiation." *Int. J. Eng. Perform.-Based Fire Codes* 8 (2006): 69-83.

[15] LeVan, Susan L., and Hao C. Tran. "The role of boron in flame-retardant treatments." (1990).

[16] Domínguez-Muñoz, Fernando, Brian Anderson, José M. Cejudo-López, and Antonio Carrillo-Andrés. "Uncertainty in the thermal conductivity of insulation materials." *Energy and Buildings* 42, no. 11 (2010): 2159-2168.

[17] “Ecotouch Insulation for Flexible Duct – Product Data Sheet.” *Owens Corning*

[18] “Polymethylmethacrylate (PMMA, Acrylic)." *Goodfellow*. http://www.goodfellow.com/E/Polymethylmethacrylate.html.

[19] Schartel, Bernhard, and T. R. Hull. "Development of fire-retarded materials—Interpretation of cone calorimeter data." *Fire and materials* 31.5 (2007): 327-354.

[20] Bakhtiyari, Saeed, Leila Taghi-Akbari, and Mehdi Barikani. "The effective parameters for reaction-to-fire properties of expanded polystyrene foams in bench scale." *Iran Polym J* 19 (2010): 27-37.

[21] An, Weiguang, Lin Jiang, Jinhua Sun, and K. M. Liew. "Correlation analysis of sample thickness, heat flux, and cone calorimetry test data of polystyrene foam." *Journal of Thermal Analysis and Calorimetry* 119, no. 1 (2015): 229-238.
[22] Schartel, Bernhard, Matthias Bartholmai, and Uta Knoll. "Some comments on the use of cone calorimeter data." *Polymer Degradation and Stability* 88.3 (2005): 540-547.
[23] White, Robert H., Sunghyun Nam, and Dharnidhar V. Parikh. "Cone calorimeter evaluation of two flame retardant cotton fabrics." *Fire and Materials* 37.1 (2013): 46-57.
[24] Bellivier, Axel, Delphine Garcia, Aurelien Thiry, Mathieu Suzanne, and Herve Bazin. "Effect of Humidity and Moisture Content on the Combustion of Materials From Household Furniture." *Laboratoire Central*. N.p., n.d.
[25] Dimitrakopoulos, A. P., and Kyriakos K. Papaioannou. "Flammability assessment of Mediterranean forest fuels." *Fire Technology* 37.2 (2001): 143-152.
[26] Urbas, Jože, and William J. Parker. "Surface temperature measurements on burning wood specimens in the cone calorimeter and the effect of grain orientation." *Fire and Materials* 17.5 (1993): 205-208.
[27] Levchik, Sergei V., and Edward D. Weil. "Thermal decomposition, combustion and fire-retardancy of polyurethanes—a review of the recent literature." *Polymer International* 53.11 (2004): 1585-1610.
[28] Singh, Harpal, and A. K. Jain. "Ignition, combustion, toxicity, and fire retardancy of polyurethane foams: a comprehensive review." *Journal of Applied Polymer Science* 111.2 (2009): 1115-1143.
[29] Davies, D., A. R. Horrocks, and M. Greenhalgh. "Ignition studies on cotton cellulose by DTA." *Thermochimica Acta* 63.3 (1983): 351-362.
[30] Wang H, Wang QS, He JJ, Mao Zl; Study on the Pyrolytic Behaviors and Kinetics of Rigid Polyurethane Foams,2013,52:377 385.
[31] C. Dick, E. Dominguez-Rosado, B. Eling, J.J.Liggat, C.I. Lindsay, S.C. Martin, M.H. Mohammed, G. Seeley, C.E. Snape; Flammability of Urethane-modified Polyisocyanurates and its Relationship to Thermal Degradation Chemistry. Polymer 42 (2001) 913-923.
[32] Chancelier, Léa, A. O. Diallo, C. C. Santini, G. Marlair, T. Gutel, S. Mailley, and C. Len. "Targeting adequate thermal stability and fire safety in selecting ionic liquid-based electrolytes for energy storage." *Physical Chemistry Chemical Physics* 16, no. 5 (2014): 1967-1976.
[33] Godfrey, Leonard EA. "Differential Thermal Analysis (DTA) and Thermogravimetric Analysis (TGA) Studies of Flame-Retardant Rayon Fibers." *Textile Research Journal* 40.2 (1970): 116-126.
[34] Roberts, B. C., A. R. Jones, O. A. Ezekoye, C. J. Ellison, and M. E. Webber. "Development of kinetic parameters for polyurethane thermal degradation modeling featuring a bioinspired catecholic flame retardant." Combustion and Flame 177 (2017): 184-192.
[35] Rayung, Marwah, Nor Azowa Ibrahim, Norhazlin Zainuddin, Wan Zuhainis Saad, Nur Inani Abdul Razak, and Buong Woei Chieng. "The effect of fiber bleaching treatment on the properties of poly (lactic acid)/oil palm empty fruit bunch fiber composites." *International journal of molecular sciences* 15, no. 8 (2014): 14728-14742.
[36] Klimovich, I. V., L. I. Leshanskaya, S. I. Troyanov, D. V. Anokhin, D. V. Novikov, A. A. Piryazev, D. A. Ivanov, N. N. Dremova, and P. A. Troshin. "Design of indigo derivatives as environment-friendly organic semiconductors for sustainable organic electronics." *Journal of Materials Chemistry C* 2, no. 36 (2014): 7621-7631.
[37] Ullah, Sami, Faiz Ahmad, and P. S. M. Yusoff. "Effect of boric acid and melamine on the intumescent fire-retardant coating composition for the fire protection of structural steel substrates." *Journal of Applied Polymer Science*128.5 (2013): 2983-2993.
[38] Whitaker, Stephen. "Simultaneous heat, mass, and momentum transfer in porous media: a theory of drying." *Advances in heat transfer* 13 (1977): 119-203.
[39] Horáček, P. "Modeling of coupled moisture and heat transfer during wood drying." *IUFRO Wood Drying Conference. Transilvania University of Brasov, Brasov, Romania*. 2003.
[40] Kulasiri, Don, and Ian Woodhead. "On modelling the drying of porous materials: analytical solutions to coupled partial differential equations governing heat and moisture transfer." *Mathematical Problems in Engineering* 2005.3 (2005): 275-291.